

## MODELING AND REMOTE SENSING TECHNIQUES

The Laboratory is involved in a broad range of programs dealing with theoretical and experimental research in the oceanic, cryospheric, and hydrologic sciences. One of the Laboratory's primary missions is the development of remote sensing technologies for the purpose of modelling and retrieving the various spectral and physical properties, which define the elements of the hydrosphere. Twenty-nine papers were found to address these specific issues. The focus for these contributions is the development of remote sensing techniques for measuring quantities ranging from snow and ice sheet properties to various ocean and land surface properties. Broad categories for these research papers can be established as follows: (1) sea ice studies (2) snow and ice-sheet studies, (3) ocean surface properties, (4) land surface hydrology studies, and (5) surface topography and altimetry studies.

- (1) Sea ice studies. This collection of studies included such diverse topics as estimating rainfall (Meneghini et al.; Chang et al.), atmospheric moisture in its various physical states (Olson et al.; Whiteman et al.), atmospheric heat profiles (Tao et al.), and a review paper by Chang which covered a variety of atmospheric parameters.
- (2) Snow and ice-sheet studies. Research in this subject area included papers on snow cover extent and mapping and (Hall et al.), ice-sheet studies (Bardel et al.), and snow physics (Wergin et al.).
- (3) Ocean surface properties. By far the largest category, these studies covered subjects such as sea ice monitoring (Markus et al.; Markus and Dokken; Zhao et al.), general ocean circulation (Keppenne and Rienecker; Hakkinen and Mo; Gregg), coastal zone studies (Renfrew and King; Dokken et al.) and ocean surface studies (Hoge and Lyon; Gregg et al.; Moisan et al.; Campbell et al.; Liu et al.; Wang et al.).
- (4) Land surface hydrology studies. These studies reported on a variety of research aspects, including soil moisture studies (Chen et al.; Jackson et al.; Owe) data assimilation (Reichle et al.) atmospheric correction (Skofronick-Jackson), and general hydrology (Houser; Bradley et al.).
- (5) Surface topography and altimetry studies. Research in these areas covered studies of sea surface altimetry studies (Vandemark et al.; Gourrion et al.) and coastal topography studies (Brock et al.).

# Synthetic aperture radar detection of the snowline on Commonwealth and Howard Glaciers, Taylor Valley, Antarctica

PATRICK BARDEL,<sup>1</sup> ANDREW G. FOUNTAIN,<sup>1</sup> DOROTHY K. HALL,<sup>2</sup> RON KWOK<sup>3</sup>

<sup>1</sup>*Departments of Geography and Geology, Portland State University, Portland, OR 97207, U.S.A.*

<sup>2</sup>*Hydrological Sciences Branch, NASA Goddard Space Flight Center, Code 974, Greenbelt, MD 20771, U.S.A.*

<sup>3</sup>*Jet Propulsion Laboratory, California Institute of Technology, 4800 Oak Grove Drive, Pasadena, CA 91109-8099, U.S.A.*

**ABSTRACT.** Synthetic aperture radar (SAR) images of Taylor Valley, Antarctica, were acquired in January 1999 in coordination with ground-based measurements to assess SAR detection of the snowline on dry polar glaciers. We expected significant penetration of the radar wave resulting in an offset of the SAR-detected snowline relative to the true snowline. Results indicated no detectable displacement of the SAR snowline. Snow depths of 15 cm over ice can be detected on the imagery. We hypothesize that the optical depth of thin snowpacks is enhanced by reflection and refraction of the radar beam by internal snow layers. The enhanced optical depth increases the volume scattering, and thereby enhances backscatter sufficiently to be detected by the SAR. Consequently, SAR imagery may be used directly to image the position of transient snowlines in dry polar regions.

## INTRODUCTION

Assessing glacier change in the polar regions, particularly in the Antarctic, has been difficult because of the distance and expense involved in conducting the fieldwork. Fieldwork also limits the spatial scope of the measurements due to the logistics of surface movement. Monitoring glaciers in the polar regions is an important component of studying the effects of climatic change because the rate and magnitude of change are expected to be greatest in those regions (Serreze and others, 2000). To monitor glacial change efficiently over broad regions requires the use of remote-observation methods. Currently, remote monitoring includes airborne laser altimetry of alpine glacier altitude (Echelmeyer and others, 1997), and satellite remote sensing (Advanced Very High Resolution Radiometer and Landsat) of ice-shelf extent (Scambos and others, 1998). An important glacial feature that can be tracked on dry polar glaciers is the position of the equilibrium line.

The equilibrium line separates the zone of net mass accumulation from the zone of net mass loss (ablation) at the end of the melt season. The equilibrium-line altitude (ELA) relative to the distribution of glacier area with altitude is an important characteristic for determining the state of the glacier's mass balance (Paterson, 1994). This presumes that the gradient of mass balance with altitude is relatively constant from year to year, but the intercept is shifted. Unlike glacier-length (terminus-position) changes, the ELA is entirely controlled by climatic processes and is not influenced by the behavior of glacier flow. In contrast to temperate or subpolar glaciers, the ELA on polar glaciers is the same as the snowline because there is no melting. One of the most attractive techniques for tracking the ELA on polar glaciers is satellite synthetic aperture radar (SAR) since it covers broad areas, it images through clouds, and it is self-illuminating. These attributes are particularly useful for the cloudy coastal conditions and long polar nights common to

polar marine environments. For dry-snow conditions, typical of polar glaciers, however, the SAR beam penetrates snow (Ulaby and others, 1981, 1982, 1986; Jezek and others, 1993; Lucchitta and others, 1995) and would displace the location of the ELA up-glacier. Maximum penetration in homogeneous snow is estimated to be about 20 m (Ulaby and others, 1981, 1982, 1986; Rott and Mätzler, 1987). This effect should be quite pronounced for thin snow accumulations on low-sloping surfaces, characteristics common to polar glaciers. For example, with a small mass-balance gradient with altitude, typical of polar glaciers, we would expect roughly a 2 km shift in the apparent snowline for a glacier with a 5° slope. The purpose of our study was to examine the extent of ELA displacement on a polar glacier and determine a correction for the SAR-estimated ELA.

## STUDY SITE

We examined two glaciers in Taylor Valley, one of the McMurdo Dry Valleys in Antarctica (Fig. 1). This area was chosen because of ongoing glaciological investigations in the valleys on four glaciers that include measurements of mass balance, energy balances, ice velocity and ice depth. Mean annual temperature in Taylor Valley is -17°C (Clow and others, 1988), and summer temperatures have not often exceeded freezing since 1993 (unpublished information from P.T. Doran). The glaciers show little or no evidence of melt except in the lowermost fringe near the glacier terminus and along the cliff face, which forms the terminus (Lewis and others, 1995; Fountain and others, 1998). Most of the mass loss is from sublimation, which during the summer represents 40–90% of the ablation (Lewis and others, 1995).

The two glaciers we studied were Commonwealth and Howard Glaciers. In this paper we examine Commonwealth Glacier in detail, and briefly mention the results from Howard Glacier in the discussion section. Commonwealth Glacier (Fig. 2) faces south-southeast with a gentle (5°) slope.

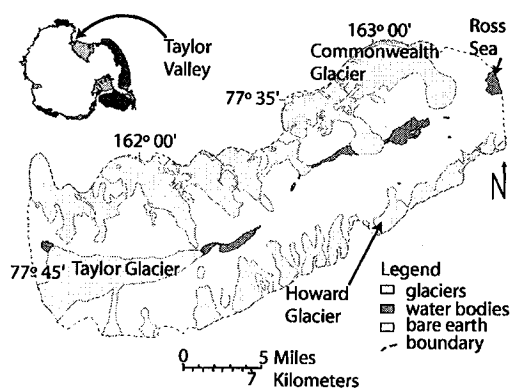


Fig. 1. Taylor Valley.

The glacier is about 2 km wide across the ELA at 350 m, with a relatively constant slope and even surface. The snow cover in the ablation zone ranges from traces to patchy, dune-like formations 4–35 cm high and covering areas of 1–20 m<sup>2</sup>. In the accumulation zone, dry snow exists on the surface, with thin (cm or less) ice layers and hoar crystals at depth.

## Methods

Mass-balance measurements are collected over the entire surface with a network of 21 stakes on Commonwealth

measurements with precisely located measurements relative to the SAR image, we set up a transect on Commonwealth Glacier from the ablation zone, across the snowline and into the accumulation zone.

## CONCLUSIONS

Glacier surfaces in Taylor Valley are generally radiometrically smooth and appear dark in the SAR image over most of the ablation zone. The snow zone images brighter because of the volume reflection from the entire depth of snow penetrated by the SAR beam. Because of the known penetration characteristics of SAR in dry snow, we expected a displacement of the SAR-inferred snowline. In contrast, the SAR-inferred and actual snowlines were very close to each other. We believe that this correspondence is due to enhanced volume reflection and can reveal the presence of snow depths of only 15 cm. Enhanced volume reflection results from layers of different densities acting as specular reflective surfaces (Ulaby and others, 1981, 1982, 1986; Mätzler and Schanda, 1984; Tsang and others, 1986). Reflection off internal layers increases the path length the beam travels (Ulaby and others, 1981, 1982, 1986), creates more opportunity to scatter in the snow and increases total reflection. Therefore thin, dry snowpacks with no internal layers will not be visible in SAR imagery.

The largest difference of backscatter between polarizations occurred in the ablation zone and reduced in the accumulation zone. On the ice surface of the ablation zone, VV polarization

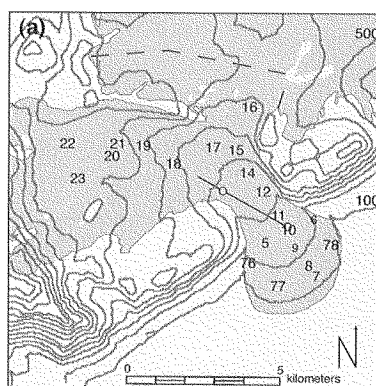
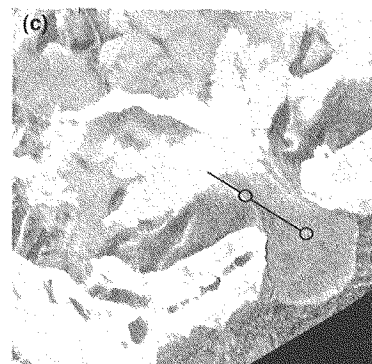
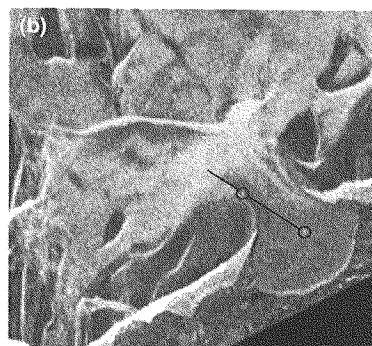


Fig. 2. Commonwealth Glacier maps; circles indicate reflector locations, and line is the transect. (a) Contour map with 100 m contours; gray areas are glacierized areas, and numbers are snow-stake locations. (b) ERS-2 uncorrected SAR image. (c) ERS-2 terrain-corrected SAR image. SAR images © 1999 European Space Agency.



Glacier as part of the ongoing monitoring. The stakes are typically measured twice annually, once in the spring (October–November) and once in the autumn (mid- to late January). The measurements include surface height, and snow depth if the snow covers the ice of the ablation zone. Whenever snow is present, a snow pit is dug at every stake and the snow stratigraphy is measured, including layer thickness, density and crystal shape. To supplement these

backscatters more than the HH polarization. In deep snow, HH backscatter increases relative to VV, and the difference in backscatter is reduced.

The corner reflectors worked very well, precisely locating the transect, adding scale and two known points to the SAR image. The reflectors were placed on smooth glacial ice, and the contrast between the dark backscatter of the ice and the brilliant reflection of the reflectors left no doubt of their locations on the image.

## RAINGAGE NETWORK DESIGN USING NEXRAD PRECIPITATION ESTIMATES<sup>1</sup>

A. Allen Bradley, Christa Peters-Lidard, Brian R. Nelson,  
James A. Smith, and C. Bryan Young<sup>2</sup>

**ABSTRACT:** A general framework is proposed for using precipitation estimates from NEXRAD weather radars in raingage network design. NEXRAD precipitation products are used to represent space time rainfall fields, which can be sampled by hypothetical raingage networks. A stochastic model is used to simulate gage observations based on the areal average precipitation for radar grid cells. The stochastic model accounts for subgrid variability of precipitation within the cell and gage measurement errors. The approach is ideally suited to raingage network design in regions with strong climatic variations in rainfall where conventional methods are sometimes lacking. A case study example involving the estimation of areal average precipitation for catchments in the Catskill Mountains illustrates the approach. The case study shows how the simulation approach can be used to quantify the effects of gage density, basin size, spatial variation of precipitation, and gage measurement error, on network estimates of areal average precipitation. Although the quality of NEXRAD precipitation products imposes limitations on their use in network design, weather radars can provide valuable information for empirical assessment of raingage network estimation errors. Still, the biggest challenge in quantifying estimation errors is understanding subgrid spatial variability. The results from the case study show that the spatial correlation of precipitation at subgrid scales (4 km and less) is difficult to quantify, especially for short sampling durations. Network estimation errors for hourly precipitation are extremely sensitive to the uncertainty in subgrid spatial variability, although for storm total accumulation, they are much less sensitive.

(KEY TERMS: network design; hydrologic sampling; precipitation measurement; NEXRAD; Catskill Mountains.)

### INTRODUCTION

Raingage network design is a problem that has received considerable attention in the hydrologic literature (for a review see Bras and Rodríguez-Iturbe, 1985). An objective of raingage network design is to determine the effects of raingage sampling (both the number of gages and their locations) on the estima-

tion uncertainty of precipitation variables or hydrologic variables computed from precipitation estimates (Bras *et al.*, 1988). This is done using either theoretical models of the rainfall process (Rodríguez-Iturbe and Mejía, 1974a; Peters-Lidard and Wood, 1994) or high resolution rainfall data from dense networks or weather radars (Huff, 1970; Seed and Austin, 1990; Fontaine, 1991).

The use of theoretical models of the rainfall process has certain advantages in raingage network design. For example, Rodríguez-Iturbe and Mejía (1974a) applied an analytical model of rainfall to derive precipitation estimation variance as a function of gage density, area of interest, correlation length scale of the rainfall process, and variance of the rainfall process. Their work considers both long-term and storm event rainfall as well as stratified (uniform) and random sampling designs. Peters-Lidard and Wood (1994) extended this approach to include events with anisotropic, time-dependent correlation structures and hierarchical clustering behavior, using a space-time stochastic model of rainfall. The use of a stochastic rainfall model in this case allowed the investigation of raingage sampling at small space (e.g., a few km) and time (e.g., minutes) scales associated with data collection for hydrologic field experiments.

Still, a limitation of using theoretical rainfall models is that space-time patterns of storm precipitation, including the initiation, growth, and dissipation of storms, are very difficult to represent with stochastic models. Usually these models assume that the statistical characteristics of precipitation do not vary in space (i.e., a stationary random field). However, cli-

<sup>1</sup>Paper No. 99151 of the *Journal of the American Water Resources Association*. Discussions are open until April 1, 2003.

<sup>2</sup>Respectively, Iowa Institute of Hydraulic Research and Department of Civil and Environmental Engineering, University of Iowa, Iowa City, Iowa 52242; Hydrological Sciences Branch, NASA-GSFC Code 974, Greenbelt, Maryland 20771; Iowa Institute of Hydraulic Research and Department of Civil and Environmental Engineering, University of Iowa, Iowa City, Iowa 52242; Department of Civil and Environmental Engineering, Princeton University, Princeton, New Jersey 08544; and Department of Civil and Environmental Engineering, Learned Hall, University of Kansas, Lawrence, Kansas 66045 (E-Mail/Bradley: allen-bradley@uiowa.edu).

matological variations are usually evident across large regions for precipitation sampled at both short and long time scales. For example, in regions with complex mountainous terrain, orography is known to affect precipitation formation and accumulation patterns.

The use of high resolution rainfall data in raingage network design attempts to mimic space-time patterns of observed precipitation (Huff, 1970). Of course, the data based approach is restricted to locations where high resolution data are available. With the recent deployment of the NEXRAD network of WSR-88D (Weather Surveillance Radar - 1988 Doppler) weather radars (Klazura and Imy, 1993), high resolution data are now being collected across the United States. Although there are known problems associated with NEXRAD radar rainfall estimates (Smith *et al.*, 1996a; Young *et al.*, 1999, 2000), NEXRAD observations still provide very good qualitative information on space-time patterns of precipitation that can be utilized in water resources applications.

In this paper we propose a general approach for use of NEXRAD radar rainfall data in raingage network design. The approach is similar to that of Seed and Austin (1990), which used radar data in Florida and South Africa to examine precipitation errors for gage sampling with hypothetical stratified and random networks. Specifically, radar rainfall data are used to represent the "true" rainfall fields for the region. However, the proposed approach differs in that the mismatch between the point precipitation (measured at a gage) and true areal average precipitation (for each radar grid cell) is considered using a theoretical model to represent the subgrid spatial variability of precipitation and gage measurement errors. As will be seen, the effect of subgrid spatial variability is very important for short sampling durations.

In the following sections, the proposed framework is presented using a case study for a mountainous region in New York. This case study for a region with complex terrain is a challenging application of the approach and demonstrates many issues that need to be considered in raingage network design using NEXRAD precipitation estimates.

## SUMMARY AND CONCLUSION

This paper describes a general framework for using NEXRAD precipitation estimates for raingage network design. The approach is illustrated through a case study conducted for six catchments in the Catskill Mountains. Network design experiments quantified the estimation errors in areal average precipitation for the catchments for random gage network alternatives. The mismatch between point

(gage) measurement and the areal average precipitation for each radar grid cell was simulated using a model that accounts for spatial variability of precipitation within the grid cell and gage measurement errors.

The case study for the Catskill region shows how the simulation approach can be used to quantify the effects of gage density, basin size, spatial variation of precipitation, and gage measurement error on network estimates of areal average precipitation. Subgrid spatial variability was found to be the most critical factor in error estimation for hourly precipitation. Average errors differed by a 100 percent or more for assumed correlation function models representing low and high subgrid variability. However, for storm total accumulation, average errors differed by around 10 to 25 percent for low and high subgrid variability cases. The high sensitivity for hourly precipitation occurs because (1) the correlation of precipitation in space is much lower, and (2) the shape of the correlation function is more difficult to estimate with available gage observations. A better understanding of small-scale spatial variability of precipitation is needed to improve quantitative estimates of network errors for short sampling durations.

The case study for the Catskill region also demonstrates the challenges in using NEXRAD precipitation estimates in a region with complex mountainous terrain. NEXRAD precipitation estimates suffered from problems due to beam blockage, ground returns, and systematic underestimation. Despite these problems, NEXRAD observations still contain valuable information on space-time patterns of storm rainfall over the region. However, to select the best storms for use in network design, we needed to focus on heavier rainfall events, carefully screen the NEXRAD data, merge estimates from multiple radars, and correct for biases with gage data. Similar efforts may be required in other regions to deal with inherent problems with NEXRAD precipitation estimates.

With conventional approaches to raingage network design, stochastic modeling is often used to simulate space-time patterns for a region. Often these models assume that precipitation fields are stationary, which severely limits their utility in large regions with complex terrain. An advantage of the proposed approach is that it uses the high resolution NEXRAD precipitation estimates to characterize space-time variations over large regions. Stochastic models of the rainfall process are applied only to simulate the mismatch between point and areal precipitation at small-scales (the size of a single radar grid cell). At this scale, the simplifying assumptions needed to model the rainfall process can still be justified. Hence, the proposed approach is ideally suited to applications in regions where significant climatic variations exist.

# Basis and Methods of NASA Airborne Topographic Mapper Lidar Surveys for Coastal Studies

John C. Brock<sup>†</sup>, C. Wayne Wright<sup>‡</sup>, Asbury H. Sallenger<sup>§</sup>, William B. Krabill<sup>\*</sup>, and Robert N. Swift<sup>††</sup>

<sup>†</sup>USGS Center for Coastal and Regional Marine Studies  
600 4th Street South  
St. Petersburg, FL,  
33701, USA  
jbrock@usgs.gov,

<sup>‡</sup>NASA Goddard Space Flight Center  
Wallops Flight Facility  
Wallops Island, VA  
23337, USA  
wright@osb.wff.nasa.gov

<sup>§</sup>USGS Center for Coastal and Regional Marine Studies  
600 4th Street South  
St. Petersburg, FL  
33701, USA  
asallenger@usgs.gov

<sup>\*</sup>NASA Goddard Space Flight Center  
Wallops Flight Facility  
Wallops Island, VA  
23337, USA  
krabill@osb1.wff.nasa.gov

<sup>††</sup>EG&G, NASA Goddard Space Flight Center  
Wallops Flight Facility  
Wallops Island, VA  
23337, USA  
swift@ao15.wff.nasa.gov

## ABSTRACT

BROCK, J.C.; WRIGHT, C.W.; SALLENGER, A.H.; KRABILL, W.B., and SWIFT, R.N., 2002. Basis and methods of NASA airborne topographic mapper lidar surveys for coastal studies. *Journal of Coastal Research*, 18(1), 1–13. West Palm Beach (Florida), ISSN 0749-0208.

This paper provides an overview of the basic principles of airborne laser altimetry for surveys of coastal topography, and describes the methods used in the acquisition and processing of NASA Airborne Topographic Mapper (ATM) surveys that cover much of the conterminous US coastline. This form of remote sensing, also known as “topographic lidar”, has undergone extremely rapid development during the last two decades, and has the potential to contribute within a wide range of coastal scientific investigations. Various airborne laser surveying (ALS) applications that are relevant to coastal studies are being pursued by researchers in a range of Earth science disciplines. Examples include the mapping of “bald earth” land surfaces below even moderately dense vegetation in studies of geologic framework and hydrology, and determination of the vegetation canopy structure, a key variable in mapping wildlife habitats. ALS has also proven to be an excellent method for the regional mapping of geomorphic change along barrier island beaches and other sandy coasts due to storms or long-term sedimentary processes. Coastal scientists are adopting ALS as a basic method in the study of an array of additional coastal topics. ALS can provide useful information in the analysis of shoreline change, the prediction and assessment of landslides along seaciffs and headlands, examination of subsidence causing coastal land loss, and in predicting storm surge and tsunami inundation.

**ADDITIONAL INDEX WORDS:** *Shoreline change, airborne laser altimetry, LaserMap.*

## INTRODUCTION

During the last decade, several complementary airborne remote sensing methods have matured, resulting in significant new capabilities that are enabling advances in coastal research. Topographic information, essential for regional and local geomorphologic studies, and useful in investigations of sedimentary processes, hydrology, pedogenesis, and wildlife habitats, can now be rapidly and accurately acquired at various spatial scales by airborne laser surveying (ALS) (ACKERMANN, 1999; BUFTON, 1989). Airborne laser surveying, or “topographic lidar”, is a type of remote sensing generally known as “Light Detection and Ranging” (lidar) that has undergone very rapid development during the last two decades (GARVIN, 1993; FLOOD and GUTELIUS, 1997). Airborne laser surveying herein refers to airborne topographic lidar, exclusive of other lidar methods. Numerous recent studies have demonstrated that current ALS systems have the potential to contribute within a wide range of coastal scientific investigations (CARTER and SHRESTHA, 1997; FLOOD *et al.*, 1997; GUTIERREZ *et al.*, 1998; HUISING and VAESSEN, 1997; KRABILL and SWIFT, 1982; KRABILL *et al.*, 2000; SALLENGER *et al.*, 1999a; SHRESTHA and CARTER, 1998).

The advent of laser scanning as a new method for the direct, high density measurement of decimeter accuracy elevation from aircraft has been enabled by the parallel development of several incorporated techniques. Kinematic differential Global Positioning System (GPS) methods now enable the positioning of light aircraft to within several centimeters (KRABILL and MARTIN, 1987). Inertial Navigation Systems (INS) or Inertial Measuring Units (IMU) can now provide three-dimensional aircraft orientation at 64-Hz within 0.1 degree, rendering aerotriangulation based on ground data points obsolete (DELOACH, 1998). Modern lightweight laser pulse transmitters can be operated at extremely high repetition rates ranging to greater than 20,000 pulses per second, and can provide ranges from a nominal 1000 m altitude with an accuracy of 1 cm or better (BUFTON, 1989).

Combined within contemporary airborne laser mapping systems, these newly emerged technologies now enable low cost geomorphic surveys at decimeter vertical accuracy and at spatial densities greater than 1 elevation measurement per square meter. Multiple-reflection ALS is uniquely well suited to the mapping of land surfaces below even moderately dense vegetation. This technique enables the creation of “bald earth” digital elevation models in forested areas for application in investigations of geologic structure and hydrology

00027 received 5 June 2000; accepted in revision 8 June 2001.

(KRABILL *et al.*, 1984; KRAUS and PFEIFER, 1998; LOHR, 1997; RITCHIE, 1995). In addition to sub-canopy topography, topographic lidars that capture the entire time-amplitude history of the return pulse can acquire the height and vertical structure of vegetation (BLAIR *et al.*, 1999). Unlike microwave or passive optical sensors, topographic lidars that capture the full reflected pulse can provide volumetric representations of canopy structure (BLAIR *et al.*, 1994; HARDING *et al.*, 1994; LEFSKY *et al.*, 1999).

As much recent work has demonstrated, ALS is an excellent means of mapping change along barrier island beaches and other sandy coasts (CARTER and SHRESTHA, 1997; FLOOD *et al.*, 1997; GUTIERREZ *et al.*, 1998; HUISING and VAESSEN, 1997; KRABILL and SWIFT, 1982; KRABILL *et al.*, 2000; SALLENGER *et al.*, 1999a; SALLENGER *et al.*, 1999b; SALLENGER *et al.*, 1999c; SHRESTHA and CARTER, 1998). The ability of ALS to rapidly survey long, narrow strips of terrain is very valuable in this application, as beaches are very elongate, highly dynamic sedimentary environments that undergo seasonal and long-term erosion or accretion, and are also impacted by severe storms (SALLENGER *et al.*, 1999b). Closely related applications are airborne laser mapping of flood-prone coastal fluvial zones, and the use of laser bathymeters to survey benthic change driven by hurricanes (PEREIRA and WICHERSON, 1999). Wave effects on nearshore circulation, sediment transport, and littoral zone topography may be investigated through ALS observations of sea state and surface wave displacement over continental shelves (HWANG *et al.*, 1998; TSAI and GARDNER, 1982).

## OBJECTIVES

The goal of this paper is to provide an overview of the methods applied within the NASA/USGS/NOAA U.S. "lower 48" coastal mapping project (SALLENGER *et al.*, 1999b) for airborne laser surveys of coastal geomorphology. The specific objectives of this paper are:

- (1) to provide the basic principles that govern the acquisition of laser ranging observations for surveys of coastal topography, and
- (2) to describe the topographic lidar surveying and processing methods in use by a NASA/USGS/NOAA project that has mapped most of the conterminous US coastline.

### Basis of Lidar Remote Sensing

The acronym "laser" stands for "light amplification by stimulated emission of radiation" and refers to devices that rely on stimulated emission to generate narrow spectral band radiation, in contrast to conventional broad spectral band spontaneous emission of radiation governed by Planck's Law. The invention of laser transmitters capable of compressing laser energy into very short, high power density single pulses enabled range-resolved measurements (MCCLUNG and HELLWARTH, 1962), analogous to microwave radar ranging. By timing the two-way travel time of a laser pulse reflected off a remote target, the range to the reflector can be directly determined through division by the speed of light. The acronym "lidar" (light detection and ranging), generally refers to any remote sensing system that emits laser light and detects,

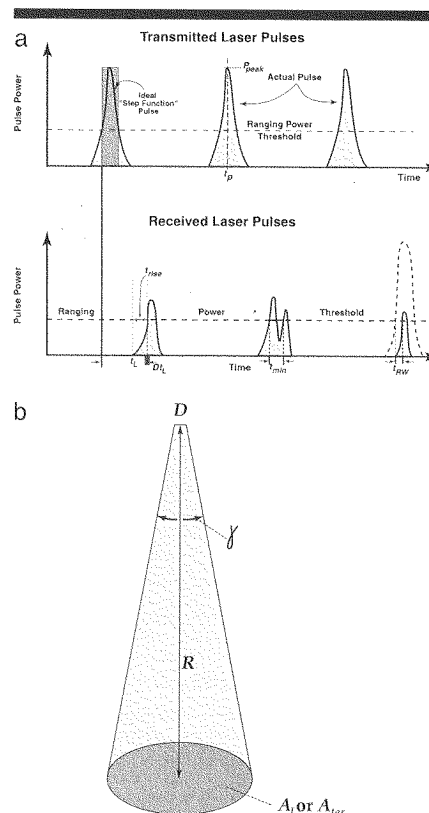


Figure 1a. Relationships between transmitted and received laser pulses (adapted from Wehr and Lohr, 1999).

Figure 1b. Geometry of a single laser shot.

ranges, or identifies remote objects based on the time-resolved sensing of light reflected or emitted through subsequent fluorescence from that object (MEASURES, 1984). By definition, lidar is a type of active remote sensing, because it incorporates an energy source to illuminate objects. Therefore, lidar differs fundamentally from passive remote sensing methods, such as multi-spectral scanning or aerial photography that rely upon reflected sunlight.

## SUMMARY

Based on its capacity for carefully-timed high resolution regional surveys keyed to natural processes, ALS is becoming a fundamental tool for coastal scientists within coastal studies. This paper provides a set of basic equations that describe laser ranging, and its implementation within the airborne laser scanning of topography. A description of the processing steps used by NASA and the USGS to extract scientifically useful information from the vast number of observations that are obtained through NASA ATM surveys is provided. The multi-tiered lidar processing approach outlined here supports the geometric, reference system, and file structure transformations that are required for most coastal applications of ALS. This approach is being incorporated in a software package called LaserMap that creates lidar data products that may be directly inserted into a Geographic Information System, or used within specialized analysis programs designed to extract landscape information for coastal studies.

## Comparison of algorithms for estimating ocean primary production from surface chlorophyll, temperature, and irradiance

Janet Campbell,<sup>1</sup> David Antoine,<sup>2</sup> Robert Armstrong,<sup>3</sup> Kevin Arrigo,<sup>4</sup> William Balch,<sup>5</sup> Richard Barber,<sup>6</sup> Michael Behrenfeld,<sup>7</sup> Robert Bidigare,<sup>8</sup> James Bishop,<sup>9</sup> Mary-Elena Carr,<sup>10</sup> Wayne Esaias,<sup>7</sup> Paul Falkowski,<sup>11</sup> Nicolas Hoepffner,<sup>12</sup> Richard Iverson,<sup>13</sup> Dale Kiefer,<sup>14</sup> Steven Lohrenz,<sup>15</sup> John Marra,<sup>16</sup> Andre Morel,<sup>2</sup> John Ryan,<sup>17</sup> Vladimir Vedernikov,<sup>18</sup> Kirk Waters,<sup>19</sup> Charles Yentsch,<sup>5</sup> and James Yoder<sup>20</sup>

Received 21 May 2001; revised 8 March 2002; accepted 8 March 2002; published 17 July 2002.

[1] Results of a single-blind round-robin comparison of satellite primary productivity algorithms are presented. The goal of the round-robin exercise was to determine the accuracy of the algorithms in predicting depth-integrated primary production from information amenable to remote sensing. Twelve algorithms, developed by 10 teams, were evaluated by comparing their ability to estimate depth-integrated daily production (IP, mg C m<sup>-2</sup>) at 89 stations in geographically diverse provinces. Algorithms were furnished information about the surface chlorophyll concentration, temperature, photosynthetic available radiation, latitude, longitude, and day of the year. Algorithm results were then compared with IP estimates derived from <sup>14</sup>C uptake measurements at the same stations. Estimates from the best-performing algorithms were generally within a factor of 2 of the <sup>14</sup>C-derived estimates. Many algorithms had systematic biases that can possibly be eliminated by reparameterizing underlying relationships. The performance of the algorithms and degree of correlation with each other were independent of the algorithms' complexity. **INDEX TERMS:** 4894 Oceanography: Biological and Chemical: Instruments and techniques; 4275 Oceanography: General: Remote sensing and electromagnetic processes (0689); 4805 Oceanography: Biological and Chemical: Biogeochemical cycles (1615); 4806 Oceanography: Biological and Chemical: Carbon cycling; 4853 Oceanography: Biological and Chemical: Photosynthesis; **KEYWORDS:** primary productivity, algorithms, ocean color, remote sensing, satellite, chlorophyll

### 1. Introduction

[2] Global maps of the upper-ocean chlorophyll concentration are now being generated routinely by satellite ocean color sensors. These multispectral sensors are able to map the chlorophyll concentration, a measure of phytoplankton biomass, by detecting spectral shifts in upwelling radiance. As the chlorophyll concentration increases, blue light is increasingly absorbed, and thus less is scattered back into space. Although global coverage can nominally be achieved every 1–2 days, the actual temporal resolution is reduced to

~5–10 days because of cloud cover. Nevertheless, the coverage afforded by satellite remote sensing is vastly greater than that obtainable by any other means.

[3] A principal use of the global ocean chlorophyll data is to estimate oceanic primary production [Behrenfeld *et al.*, 2001]. The mathematical models or procedures for estimating primary production from satellite data are known as primary productivity algorithms. In the early days of the Coastal Zone Color Scanner (CZCS), simple statistical relationships were proposed for calculating primary production from the surface chlorophyll concentration [e.g., Smith and Baker, 1978; Eppley *et al.*, 1985]. Such empirically derived algorithms are still considered useful when applied to annually averaged data [Iverson *et al.*, 2000], but they are not sufficiently accurate to estimate production at seasonal timescales. The surface chlorophyll concentration explains only ~30% of the variance in primary production at the scale of a single station [Balch *et al.*, 1992; Campbell and O'Reilly, 1988].

[4] Over the past 2 decades, scientists have sought to improve algorithms by combining the satellite-derived chlorophyll data with other remotely sensed fields, such as sea surface temperature (SST) and photosynthetic available radiation (PAR). These algorithms incorporate models

**Table 1.** Algorithm Testing Subcommittee of NASA's Ocean Primary Productivity Working Group<sup>a</sup>

Participant	Affiliation
Robert Armstrong	Stony Brook University
Richard T. Barber	Duke University
James Bishop	Lawrence Berkeley National Laboratory
Janet W. Campbell	University of New Hampshire
Mary-Elena Carr	Jet Propulsion Laboratory
Wayne E. Esaias	NASA Goddard Space Flight Center
Richard Iverson	Florida State University
Charles S. Yentsch	Bigelow Laboratory for Ocean Sciences

<sup>a</sup>These individuals were responsible for conducting the primary productivity algorithm round-robin experiment. They agreed not to participate by testing algorithms of their own.



of the photosynthetic response of phytoplankton to light, temperature, and other environmental variables, and some also incorporate models of the vertical distribution of these properties within the euphotic zone [Balch *et al.*, 1989; Morel, 1991; Platt and Sathyendranath, 1993; Howard, 1995; Antoine and Morel, 1996a; Behrenfeld and Falkowski, 1997a; Ondrusek *et al.*, 2001]. Algorithms have been used to estimate global oceanic primary production from CZCS data [Antoine and Morel, 1996b; Longhurst *et al.*, 1995; Behrenfeld and Falkowski, 1997a; Howard and Yoder, 1997], and more recently from Sea-viewing Wide Field-of-view Sensor (SeaWiFS) data [Behrenfeld *et al.*, 2001]. Global maps of the average daily primary production for varying periods (weeks, months, and years) are now being produced from Moderate Resolution Imaging Spectroradiometer (MODIS) data.

[5] While many of the photosynthetic responses (to light, temperature, etc.) are commonly represented, model-based algorithms differ with respect to structure and computational complexity [Behrenfeld and Falkowski, 1997b]. Models may be similar in structure but require different parameters depending on whether they describe daily, hourly, or instantaneous production, and even where these aspects are similar, algorithms often yield different results because of differences in their parameterization. Balch *et al.* [1992] evaluated a variety of algorithms (both empirical and model based), using in situ productivity measurements from a large globally distributed data set, and found that they generally accounted for <50% of the variance in primary production.

[6] In January 1994 the National Aeronautics and Space Administration (NASA) convened an Ocean Primary Productivity Working Group with the goal of developing one or more “consensus” algorithms to be applied to satellite ocean color data. The working group initiated a series of round-robin experiments to evaluate and compare primary productivity algorithms. The approach was to use in situ data to test the ability of algorithms to predict depth-integrated daily production (IP,  $\text{mg C m}^{-2}$ ) based on information amenable to remote sensing. It was decided to compare algorithm performances with one another and with estimates based on  $^{14}\text{C}$  incubations.

[7] Our understanding of primary productivity in the ocean is largely based on the assimilation of inorganic carbon from  $^{14}\text{C}$  techniques [Longhurst *et al.*, 1995], and thus it was considered appropriate to compare the algorithm estimates with  $^{14}\text{C}$ -based estimates. However, it was recognized that the  $^{14}\text{C}$ -based estimates are themselves subject to error [Peterson, 1980; Fitzwater *et al.*, 1982; Richardson, 1991]. The  $^{14}\text{C}$  incubation technique measures photosynthetic carbon fixation within a confined volume of seawater, and there are no methods for absolute calibration of bottle incubations [Balch, 1997]. Furthermore, there is no universally accepted method for measuring and verifying vertically integrated production derived from discrete bottle measurements. Despite this fact, here we treat the  $^{14}\text{C}$ -based estimates as “truth” and refer to the differences between algorithm-derived and  $^{14}\text{C}$ -derived estimates as “errors.” In all statistical analyses, however, the two are recognized as being subject to error.

[8] Participation in the round robin was solicited through a widely distributed “Dear Colleague” letter. A central ground rule was that the algorithms tested would be identified only by code numbers. The first round-robin experiment involved data from only 25 stations and was thus limited in scope. It was decided that a more comprehensive second round was needed. In this paper, we present results of the second round-robin experiment involving data from 89 stations with wide geographic coverage. Round two was open to all participants of round one, as well as to others who had responded positively to the initial invitation.

## 6. Conclusions

[45] Conclusions related to the four questions addressed by this study are summarized as follows:

[46] 1. How do algorithm estimates of primary production derived strictly from surface information compare with estimates derived from  $^{14}\text{C}$  incubation methods? The 12 algorithms tested varied widely in performance. The best-performing algorithms agreed with the  $^{14}\text{C}$ -based estimates within a factor of 2. Two of these algorithms have been adapted by NASA for producing primary productivity maps with MODIS data. Most of the algorithms had significant biases causing them to differ systematically from the in situ data. A concerted effort should be made to understand the cause of the biases and to eliminate them if possible.

[47] 2. How does the error in satellite-derived chlorophyll concentration affect the accuracy of the primary productivity algorithms? The relative errors in primary productivity ( $\Delta_{\text{sat}}$ ) resulting from the simulated errors in surface chlorophyll concentration ( $\Delta_B$ ) were highly correlated with  $\Delta_B$ . This fact reflects the deterministic relationship between production and chlorophyll in the underlying models. The slopes of the regressions ( $\Delta_{\text{sat}}$  versus  $\Delta_B$ ) ranged between 0.3 and 0.8, indicating that errors in surface chlorophyll produce less-than-proportionate errors in IP.

[48] 3. Are there regional differences in the performance of algorithms? There were significant regional differences, as well as algorithm-region interactions, indicated by the ANOVA results. No one region was uniformly better or worse for all algorithms. The region with the most serious biases was the equatorial Pacific, where algorithms underestimated in situ measurements by a factor of 2.

[49] 4. How do algorithms compare with each other in terms of complexity vis-a-vis performance? Many of the algorithms were highly correlated with one another. This was not surprising, since several are based on the same models, but what was surprising was that the level of agreement had no apparent relationship to the mathematical structure or complexity of the algorithms. In some cases, complex algorithms based on depth-, time- and wavelength-resolved models were highly correlated with simpler algorithms that were time and/or depth integrated. There were distinct systematic differences between algorithms. A future effort to understand systematic differences is strongly recommended.

# ERS SAR characterization of coastal polynyas in the Arctic and comparison with SSM/I and numerical model investigations

Sverre Thune Dokken<sup>a,\*</sup>, Peter Winsor<sup>b</sup>, Thorsten Markus<sup>c</sup>, Jan Askne<sup>a</sup>, Göran Björk<sup>b</sup>

<sup>a</sup>*Department of Radio and Space Science, Chalmers University of Technology, Gothenburg, Sweden*

<sup>b</sup>*Department of Oceanography, Earth Sciences Centre, Göteborg University, Gothenburg, Sweden*

<sup>c</sup>*NASA/GSFC-UMBC JCET, Greenbelt, MD, USA*

Received 31 July 2000; received in revised form 21 June 2001; accepted 25 June 2001

## Abstract

Coastal polynyas in the Arctic basin from the winter period (January to April) are characterized using ESA European Remote Sensing satellite (ERS)-1/2 Synthetic Aperture Radar (SAR) Precision (Precise Image, PRI) and Browse images. A SAR polynya algorithm is used to delineate open water, new ice, and young ice, and to define the size and shape of polynyas. In order to extract radiometric and contextual information in the ERS SAR PRI images, three different image classification routines are developed and applied. No in situ data have been available for verification of the polynya shapes and sizes, but one of the ice classification routines have been verified earlier using ground truth data. The SAR polynya algorithm is demonstrated to be able to discriminate between the polynya and the surrounding ice area for 85 analyzed cases. The results from the SAR algorithm are compared to ERS Browse images, passive microwave data (a recent Polynya Signature Simulation Method (PSSM), and the Bootstrap and the NASA Team ice concentration algorithms), and a numerical polynya model (NPM) forced by National Center for Environmental Predictions (NCEP) wind fields and air temperatures. The ERS SAR Browse images show a relatively good correlation with the ERS SAR PRI images (.88) while the Special Sensor Microwave Imager (SSM/I) Bootstrap and the NASA Team ice concentration algorithms both have low correlation coefficients (below .3). The PSSM calculates the polynya shape and size, and delineates open water and thin ice. For polynyas of all sizes it has a correlation of .69 compared to the SAR PRI images. For polynyas with widths greater than 10 km the correlation increases to .83. The NPM computes offshore coastal polynya widths, heat exchange, and ice production. Compared to SAR data, it overestimates the maximum size of the polynya by about 15% and has a correlation of .71 compared to the analyzed SAR PRI images. The polynyas in our main investigation area, located at Franz Josef Land, are found to be primarily wind driven. The surrounding large-scale ice drift and tidal currents have little effect on the polynya behavior. One overall conclusion from this investigation is that SAR images processed through the SAR polynya algorithm in combination with the NPM is a powerful tool for investigating and characterizing polynyas at various scales in the Arctic. © 2002 Elsevier Science Inc. All rights reserved.

## 1. Introduction

Global climate models predict that a possible temperature rise will be amplified in the Arctic because of various feedback mechanisms associated with a strong coupling among the Arctic ice cover, the atmosphere, and the ocean (see e.g., Gloersen & Campbell, 1991; Manabe & Stouffer, 1993). Some of these feedback mechanisms are related to the intense heat transfer between ocean and atmosphere in polynyas and leads with large ice production and release of salt. The heat exchange from the ocean to the atmosphere can be two to three orders of magnitude larger in polynyas compared to the surrounding ice masses with an ice production of up to 5 m per event or some 50% of the seasonal mean in some areas (Winsor & Björk, 2000). Siberian shelf polynyas are capable to form 20–60% of the Arctic intermediate water (Martin & Cavalieri, 1989), and Arctic polynyas in general provide about 30% of the estimated salt flux necessary to maintain the cold halocline layer of the Arctic Ocean (Winsor & Björk, 2000). Knowledge of the

distribution and frequency of coastal polynyas and leads is therefore important in order to understand large-scale climate processes in the Arctic Basin.

Satellite observations is the only possibility to monitor the Arctic ice cover on a basin wide scale. The detection potential of satellite sensors is, however, limited by their radiometric properties and their temporal and spatial resolution. Traditionally, satellite passive microwave sensors have been used to study polynyas because of their continuous temporal and spatial coverage (c.f. Cavalieri & Martin, 1985, 1994; Markus, Kottmeier, & Fahrbach, 1998; Martin & Cavalieri, 1989; Zwally, Comiso, & Gordon, 1985). Due to the typical size of polynya features (6 km average width, Winsor & Björk, 2000), a relatively high spatial resolution of the satellite sensor is required. The relatively coarse spatial resolution of passive microwave sensors (25–50 km) therefore strongly restricts the information that can be retrieved for polynya studies (i.e. they necessitate subpixel classification). There are means to improve the resolution of passive microwave data by

designing a special algorithm for detecting coastal polynyas such as the Polynya Signature Simulation Method (PSSM, Markus & Burns, 1995). The PSSM has an improved spatial resolution (approximately 6 km) compared to traditional methods (e.g. the Bootstrap and the NASA Team ice concentration algorithms), which increases the possibility to detect and characterize polynyas.

The active Synthetic Aperture Radar (SAR) enables high resolution imaging (25 m spatial resolution) of the geographic region of interest independent of daylight and cloud cover. However, satellites carrying this sensor (European Remote Sensing satellite, ERS-1/2) have relatively low temporal resolution and today's SARs only use one polarization and one frequency, further limiting the detection possibilities. However, Radarsat-1, and within soon, Envisat and Radarsat-2 will have improved coverage.

This article presents one of the first approaches to study polynyas in the inner Arctic Basin during the winter months (January to April). A combination of methods is presented in order to detect the size and shape of coastal polynyas. We use both atmospheric and oceanographic data sets and a numerical model in addition to satellite observations. First, we describe routines to identify polynyas in the Arctic, by (1) ERS SAR Browse images for location of polynyas in space and time and Precise Image (PRI) images for detailed study of the polynyas, (2) Special Sensor Microwave Imager (SSM/I) images using the PSSM algorithm, and (3) a numerical polynya model (NPM). A major issue described in some detail is a new wavelet-based SAR polynya algorithm that is used to identify sizes and shapes of polynyas. We investigate to what extent the NPM and the PSSM agree with the polynya characteristics from the SAR algorithm, which we consider the most accurate identification method due to, e.g., its spatial resolution. The different methods are applied for the same geographical region of interest and within the smallest possible time interval.

#### 4. Conclusions

Automatic polynya characterization using SAR with only VV polarization is limited primarily because open water and/or an ice class can mix with each other in the backscatter and/or texture domain. However, the SAR sensor's high spatial resolution, and the SAR polynya algorithm's addition of a "irregularity" parameter and a wavelet-based edge detection method compensate for this weakness. The SAR polynya algorithm is shown to be competitive compared to traditional methods based solely on intensity and texture measures (cf. Fig. 7) and is able to discriminate between the polynya and the surrounding ice areas for 85 analyzed cases. The algorithm consists of three independent loops in order to reduce possible errors. One of the loops (the right loop in Fig. 3) has previously been verified with overlapping aerial photography. The high-resolution SAR images can also be visually interpreted, which enables an additional control of the algorithm's performance. The SAR polynya algorithm is suitable to serve as a reference when

compared to the Polynya SSM/I signature model (Markus & Burns, 1995) and an NPM (Winsor & Björk, 2000).

The NPM-estimated average offshore width of coastal polynyas in the Arctic is about 6 km. This is too small for effective monitoring with the SSM/I Bootstrap and the NASA Team ice concentration algorithms. Results from these algorithms have traditionally been used for polynya identification and classification but they give low correlation (less than .3) with the measured SAR polynya sizes (see Fig. 8). The PSSM, however, significantly increases the applicability of the SSM/I data, given the coarse resolution of approximately 6 km. When only larger-sized polynyas (>10 km) are compared, it has a thin ice correlation coefficient of .83 compared to SAR derived young ice. When all sizes of polynyas are compared (54 cases) it has an offshore width correlation of .69 compared to the SAR (see Table 1).

Numerical modeling of polynyas is effective even at small scales and in the dynamic environment typical of coastal polynyas. SAR PRI images provides the most useful data set to validate NPMs and the use of SAR in combination with an NPM significantly contributes to characterize and to gain knowledge about the dynamics of polynyas. This SAR investigation shows that the NPM-computed polynya widths (and thereby the ice and salt productions) are overestimated by approximately 15% for areas with high polynya activity. This investigation also shows that the NPM is mostly hampered by uncertainties in the atmospheric forcing and the large-scale ice drift in the basin. The NPM-computed offshore width has a correlation of .71 compared to SAR open water/new ice for 61 analyzed cases.

Future enhancement of the SAR polynya algorithm will be to combine different image representations (e.g. curvelets and wavelets) in order to improve the delineation of young ice types inside the polynya. A further operational combination of the PSSM and the SAR methods (applicable when SAR data are not available) can enhance the distinction between different new and young ice types in the PSSM model. This distinction is very important for a better understanding of the dynamics and processes in polynyas as well as for a more accurate description of the ocean to atmosphere heat exchange.

One overall conclusion from this investigation is that SAR images processed through the SAR polynya algorithm in combination with the NPM is a powerful tool for investigating and characterizing polynyas at any scale in the Arctic.

The future development of SAR satellite imagery is promising. Forthcoming SAR satellites (Envisat and Radarsat-2) will have full polarization and increased temporal and spatial coverage that will further increase the usage of this sensor. Envisat will have the same orbit configuration as ERS (35-day repeat cycle) and a maximum available swath width of 485 km (while ERS has 100 km).

# A Two-Parameter Wind Speed Algorithm for Ku-Band Altimeters

J. GOURRION

*IFREMER, Département d'Océanographie Spatiale, Plouzané, France*

D. VANDEMARK AND S. BAILEY

*NASA Goddard Space Flight Center, Wallops Island, Virginia*

B. CHAPRON

*IFREMER, Département d'Océanographie Spatiale, Plouzané, France*

G. P. GOMMENGINGER, P. G. CHALLENGOR, AND M. A. SROKOSZ

*The James Rennell Division, Southampton Oceanography Centre, Southampton, United Kingdom*

(Manuscript received 5 July 2001, in final form 15 March 2002)

## ABSTRACT

Globally distributed crossovers of altimeter and scatterometer observations clearly demonstrate that ocean altimeter backscatter correlates with both the near-surface wind speed and the sea state. Satellite data from TOPEX/Poseidon and NSCAT are used to develop an empirical altimeter wind speed model that attenuates the sea-state signature and improves upon the present operational altimeter wind model. The inversion is defined using a multilayer perceptron neural network with altimeter-derived backscatter and significant wave height as inputs. Comparisons between this new model and past single input routines indicates that the rms wind error is reduced by 10%–15% in tandem with the lowering of wind error residuals dependent on the sea state. Both model intercomparison and validation of the new routine are detailed, including the use of large independent data compilations that include the SeaWinds and ERS scatterometers, ECMWF wind fields, and buoy measurements. The model provides consistent improvement against these varied sources with a wind-independent bias below  $0.3 \text{ m s}^{-1}$ . The continuous form of the defined function, along with the global data used in its derivation, suggest an algorithm suitable for operational application to Ku-band altimeters. Further model improvement through wave height inclusion is limited due to an inherent multivaluedness between any single realization of the altimeter measurement pair  $[\sigma^0, H_s]$  and observed near-surface winds. This ambiguity indicates that  $H_s$  is a limited proxy for variable gravity wave properties that impact upon altimeter backscatter.

## 1. Introduction

Empirical models have been devised to improve satellite altimeter ocean wind speed retrieval using many differing numerical approaches and datasets (Brown et al. 1981; Dobson et al. 1987; Chelton and McCabe 1985; Witter and Chelton 1991; Glazman and Greysukh 1993; Young 1993; Lefèvre et al. 1994; Freilich and Challenor 1994). The global altimeter ocean wind product is mostly limited to validation and climatological usage (e.g., Young 1999) because the altimeter's nadir-pointing geometry only permits estimates of surface wind speed along a narrow ( $\approx 2 \text{ km}$ ) swath and precludes wind direction detection. However, accurate wind speed estimates are also important because they are used in the point-by-point correction of an altimeter's estimate of mean sea surface height via the electromagnetic bias algorithm. Freilich and Challenor (1994) and Glazman and Greysukh (1993) expand on these points and suggest that objective model improvement metrics should include the minimization of wind speed biases and root-mean-square error, removal of nonwind geophysical impacts such as sea state, and functional continuity (finite first derivative) such that the wind speed histogram is not distorted.

The operational altimeter wind speed product for TOPEX is derived from interpolation over the look up table known as the modified Chelton–Wentz algorithm (MCW) of Witter and Chelton (1991). This model directly maps measured Ku-band altimeter backscatter ( $\sigma^0$ ) to the wind speed  $10 \text{ m}$  above the ocean ( $U_{10}$ ). The overall bias,  $\langle U_{\text{err}} \rangle$ , for this algorithm is suggested to be  $0.48 \text{ m s}^{-1}$  ( $U_{\text{err}} = U_{\text{altim}} - U_{\text{insitu}}$ ) and the root-mean-square (rms) error lies between  $1.5$  and  $2.0 \text{ m s}^{-1}$  (e.g., Witter and Chelton 1991; Gower 1996; Freilich and Challenor 1994; Wu 1999). Numerous studies have suggested that the form for this single parameter algorithm could be improved upon (e.g., Freilich and Challenor 1994). However, the limited amount of validation data combined with the generally small level of improvement in algorithm performance leaves MCW as the current choice for new altimeters such as the GEOSAT Follow-On (GFO) and *Jason-1*.

A goal that remains of interest for altimeter wind retrieval is the detection and correction of wind speed errors associated with longer ocean waves that are not necessarily closely coupled to the local wind field. Evidence for a sea-state effect on altimeter-derived wind has been addressed in several studies (Monaldo and

Dobson 1989; Glazman and Pilorz 1990; Glazman and Greysukh 1993; Lefèvre et al. 1994; Freilich and Challenor 1994; Hwang et al. 1998). Reported results range from substantial impacts to no impact (cf. Wu 1999). The central and unique factor here is an altimeter's coincident and accurate measure of significant wave height,  $H_s$ .

Motivation for the present study follows from compilation of a large number of TOPEX altimeter observations made coincident with National Aeronautics and Space Administration (NASA) scatterometer (NSCAT) surface wind estimates. The global coverage, fidelity, and volume of this dataset leads to a much clearer picture of  $H_s$  variation impacts upon altimeter backscatter and wind inversion over a range of wind speeds from 1 to 20  $\text{m s}^{-1}$ . We develop two models, a forward and an inverse solution, using neural network methods to map between altimeter and scatterometer observations and incorporating a globally derived correction for sea-state impacts using the altimeter-derived  $H_s$  estimate. Numerous independent datasets containing collocation between altimeter and ancillary wind estimates are then used to evaluate a best-choice routine and its applicability for operational usage. This paper is derived from an earlier report by Gourrion et al. (2000). That effort includes wind speed models for the C-band altimeter aboard TOPEX, but the present effort concentrates solely on Ku-band model definition.

## 7. Summary

This study defines and validates a two-input altimeter wind speed algorithm applicable for operational use, where a Ku-band altimeter's coincident  $\sigma^\circ$  and  $H_s$  estimates are utilized in the point-to-point inversion. An analytical formulation (termed  $f_1$ ) is prescribed with nine coefficients as detailed in section 4. Motivation comes from the new capability to assemble large, globally distributed and high fidelity model training sets composed of coincident satellite altimeter and scatterometer crossovers. The dataset chosen for model training and subsequent validation is a 96 000 sample compilation of TOPEX and NSCAT crossings. Limiting NSCAT usage to only higher incidence angle retrievals strengthens our assumption that the scatterometer wind product is itself free of sea-state impacts. Subsequent validations using buoy and ECMWF winds provide further support.

The empirical development is focused to define an improved and robust wind inversion that incorporates  $H_s$  into the solution. This routine should be applicable for all Ku-band altimeters such as those aboard the ERS, ENVISAT, GFO, and *Jason-1* platforms.  $f_1$  intercomparison to past altimeter models and numerous independent validations demonstrates modest, but measurable, success in improving upon the current operational MCW model. These independent data sources include an extensive buoy compilation, the ERS scatterometer, the SeaWinds scatterometer, and the ECMWF model. The  $f_1$  inversion ( $[\sigma^\circ, H_s] \rightarrow [U_{10N}]$ ) delivers an overall

rms improvement of 10–15%, 0.1 to 0.2  $\text{m s}^{-1}$  in absolute terms. The domain for model application covers all values of  $H_s$  and wind speeds ranging from 1 to 20  $\text{m s}^{-1}$ . Error statistics were evaluated over the range of 1–17  $\text{m s}^{-1}$ . Wind speed bias is below 0.3  $\text{m s}^{-1}$  throughout this range. Improvement in rms error is significant up to winds of about 12  $\text{m s}^{-1}$  and equivalent to MCW above this point. The weighting of  $H_s$  within the model becomes negligible at these high wind levels. While wind speeds above 20  $\text{m s}^{-1}$  are infrequent, a slight modification of  $f_1$  that aligns the altimeter inversion with that predicted by the *QSCAT-1* model function is proposed in appendix B. Statistically, the GG2 algorithm provides similar improvement, but we recall that this classification scheme leads to point-to-point estimate discontinuities and a bi-modal wind speed distribution. TOPEX wind speed histograms, derived using  $f_1$ , provide marked improvement over the MCW result in comparison to either buoy, model or scatterometer results. This affirms the continuous nature of the network solution and its applicability for operational use. The TOPEX-generated model is also shown to work well when applied to *ERS-2* altimeter data. The model is adjusted for differing altimeters using a constant  $\sigma^\circ$  bias and is also relatively insensitive to  $H_s$  estimate errors.

Physically, one expects that  $H_s$  is a limited proxy for actual gravity wave slope variations that affect the nominal relation between the observed radar cross section and wind speed. Observations and model functions depict measurable correlations amongst the three variables [ $\sigma^\circ$ ,  $H_s$ ,  $U_{\text{NSCAT}}$ ] but they also exhibit a multivaluedness that inhibits further wind estimate improvement in the absence of additional surface roughness information. This ambiguity leads to an increased altimeter wind speed noise if one attempts to use the forward ( $f_2$ ) model for  $U_{10}$  inversion. This effect occurs even though  $f_2$  is the most effective at removing residual error associated with  $H_s$ . Another repercussion is the inability of the  $f_1$  model to correct altimeter wind underestimation during fetch-limited events. These events are rare within the global data set and the neural network minimization solution gives little weight (by design) to this mapping within the domain of possible outcomes.

These points emphasize that present empirical and global-mean model functions do not fully capture the scattering physics. Their application to specific case study will not dramatically improve upon results derived using the MCW model. It is clear, however, that the  $f_1$  algorithm is a measurable improvement that can directly replace the single parameter routine. As importantly, the documented correlation between  $\sigma^\circ$  and  $H_s$  at any chosen wind speed needs to be considered within the empirical modeling of the altimeter sea state bias correction (cf. Chapron et al. 2001). Future work combining the altimeter's unique coincident measure of  $H_s$  with multifrequency  $\sigma^\circ$  (e.g., at S-, C-, Ka- and/or Ku-band) signatures is certain to bring further refinement to these geophysical inversions on both global and local scales.





# Tracking the SeaWiFS record with a coupled physical/biogeochemical/radiative model of the global oceans

Watson W. Gregg

*NASA/Goddard Space Flight Center, Laboratory for Hydrospheric Processes, Greenbelt, MD 20771, USA*

Accepted 16 June 2001

## Abstract

The Sea-Viewing Wide Field-of-view Sensor (SeaWiFS) has observed multiple years of routine global chlorophyll observations from space. The mission was launched into a record El Niño event, which eventually gave way to one of the most intense and longest-lasting La Niña events ever recorded. The SeaWiFS chlorophyll record captured the response of ocean phytoplankton to these significant events in the tropical Indo-Pacific basins, but also indicated significant interannual variability unrelated to the El Niño/La Niña events. This included large variability in the North Atlantic and Pacific basins, in the North Central and equatorial Atlantic, and milder patterns in the North Central Pacific.

This SeaWiFS record was tracked with a coupled physical/biogeochemical/radiative model of the global oceans using near-real-time forcing data such as wind stresses, sea surface temperatures, and sea ice. This provided an opportunity to offer physically and biogeochemically meaningful explanations of the variability observed in the SeaWiFS data set, since the causal mechanisms and interrelationships of the model are completely understood.

The coupled model was able to represent the seasonal distributions of chlorophyll during the SeaWiFS era, and was capable of differentiating among the widely different processes and dynamics occurring in the global oceans. The model was also reasonably successful in representing the interannual signal, especially when it was large, such as the El Niño and La Niña events in the tropical Pacific and Indian Oceans. The model provided different phytoplankton group responses for the different events in these regions: diatoms were predominant in the tropical Pacific during the La Niña, but other groups were predominant during El Niño. The opposite condition occurred in the tropical Indian Ocean. Both situations were due to the different responses of the basins to El Niño. Interannual variability in the North Pacific was exhibited as an increase in the spring bloom in 1999 and 2000 relative to 1998. This resulted in the model from a shallower and more rapidly shoaling mixed layer, producing more average irradiance in the water column and preventing herbivore populations to keep pace with increasing phytoplankton populations. However, several aspects of the interannual cycle were not well-represented by the model. Explanations range from inherent model deficiencies, to monthly averaging of forcing fields, to biases in SeaWiFS atmospheric correction procedures.

## 1. Introduction

The Sea-Viewing Wide Field-of-view Sensor (SeaWiFS; McClain et al., 1998) has provided the first multi-year global chlorophyll observations from space since the Coastal Zone Color Scanner (CZCS). It represents an unprecedented data set in terms of coverage, continuity, and duration that enables us for the first time to make meaningful observations about the state of biological components in the global oceans, their spatial variability, and their medium-term (seasonal to interannual) variability. This latter point especially differentiates SeaWiFS from the two previous large-scale-coverage missions, the CZCS, which did not provide routine global coverage in its 8-year lifetime (Feldman et al., 1989), and the Ocean Color and Temperature Scanner (OCTS), which failed after nine months of on-orbit operations (Shimoda, 1999).

The comprehensive SeaWiFS data set, beginning in September 1997, provides an opportunity to observe the behavior of ocean phytoplankton in response to seasonal and interannual variability. If analysis of this record is combined with the outputs of a coupled physical/biogeochemical model whose dynamical features are completely understood, then insights may be gained into the causes of this variability, especially when the results are in agreement. Even when they are not, this combination of analysis methodologies can help us infer what processes are not incorporated into the model and their apparent importance.

#### **4. Conclusions**

The nearly 3-year SeaWiFS record from launch (September 1997) to June 2000 has given us our first comprehensive glimpse of interannual variability of ocean chlorophyll dynamics. Moreover, SeaWiFS was launched as one of the largest El Niño events was underway, and which eventually gave way to one of the largest, most intensive, and longest-lasting La Niña events ever recorded (continuing at the end of the record). The SeaWiFS chlorophyll record captured the response of ocean phytoplankton to these significant events in the tropical Indo-Pacific basins, but also indicated significant interannual variability unrelated to the El Niño/La Niña. This included large variability in the North Atlantic and Pacific basins, large variability in the North Central and equatorial Atlantic, and milder patterns in the North Central Pacific, the latter of which may be due partially to the El Niño. The Southern Hemisphere exhibited, in contrast, relatively little interannual variability during the SeaWiFS record.

We are fortunate to live in an era when global atmospheric data sets are routinely and nearly immediately available. Thus we have the opportunity to drive a coupled physical/biogeochemical/radiative model of the global oceans with actual near-real-time forcing data such as wind stresses, SSTs, shortwave radiation, and sea ice. Our only limitation is cloud cover and thickness data, which are necessary to evaluate the spectral irradiance with depth, which drives phytoplankton dynamics. Although this is a shortcoming, the availability of the other forcing data gives us an opportunity to track the SeaWiFS record with a global coupled model and attempt to provide physically and biogeochemically meaningful explanations of the variability observed in the SeaWiFS data set.

Even without cloud data, the coupled model was able to represent the seasonal distributions of chlorophyll during the SeaWiFS era, and was capable of differentiating among the widely different processes and dynamics occurring in the global oceans. The model was also reasonably successful in representing the interannual signal, especially when it was large, such as the El Niño and La Niña events in the tropical Pacific and Indian Oceans. In these two regions the model provided different phytoplankton group responses for the different events. The interannual variability in the North Pacific, which was exhibited in SeaWiFS data as an increase in the spring bloom in 1999 and 2000 relative to 1998, was represented and resulted in the model from a more rapidly shoaling mixed layer, inhibiting herbivore population development, thus preventing maximum and immediate utilization of available nutrients from winter convection. However, several aspects of the interannual cycle were not well-represented by the model. Some of which may be due to the model deficiencies of a lack of topographic and coastal influences such as the North Indian Ocean, some may be related to the lack of monthly cloud data, some may be due to riverine influences missing in the model such as the equatorial Atlantic, and finally some may be the result of biases in SeaWiFS atmospheric correction procedures such as absorbing aerosols which are common in the equatorial and mid-latitude eastern Atlantic and the North and equatorial Indian Oceans. Nevertheless, broad agreement suggests confidence in the large scale (synoptic and basin scale) processes in the model and its ability to provide plausible explanations for some the variability observed in this unique spaceborne data set.

# NOAA–NASA Coastal Zone Color Scanner Reanalysis Effort

Watson W. Gregg, Margarita E. Conkright, John E. O'Reilly, Frederick S. Patt,  
Menghua H. Wang, James A. Yoder, and Nancy W. Casey

Satellite observations of global ocean chlorophyll span more than two decades. However, incompatibilities between processing algorithms prevent us from quantifying natural variability. We applied a comprehensive reanalysis to the Coastal Zone Color Scanner (CZCS) archive, called the National Oceanic and Atmospheric Administration and National Aeronautics and Space Administration (NOAA–NASA) CZCS reanalysis (NCR) effort. NCR consisted of (1) algorithm improvement (AI), where CZCS processing algorithms were improved with modernized atmospheric correction and bio-optical algorithms and (2) blending where *in situ* data were incorporated into the CZCS AI to minimize residual errors. Global spatial and seasonal patterns of NCR chlorophyll indicated remarkable correspondence with modern sensors, suggesting compatibility. The NCR permits quantitative analyses of interannual and interdecadal trends in global ocean chlorophyll. © 2002 Optical Society of America

OCIS codes: 010.4450, 010.1290, 280.0280.

## 1. Introduction

NASA and the international scientific communities have established a record of nearly continuous, high-quality global ocean color observations from space since 1996. The Ocean Color and Temperature Scanner (OCTS; November 1996–June 1997), the Sea-viewing Wide Field-of-view Sensor (SeaWiFS; September 1997–present), and the Moderate-Resolution Imaging Spectroradiometer (MODIS; September 2000–present) have provided an unprecedented view of chlorophyll dynamics on global scales by use of modern, sophisticated data processing methods. A predecessor sensor, the Coastal Zone Color Scanner (CZCS; November 1978–June 1986), utilized processing methodologies and algorithms that are outdated by modern standards. Thus the CZCS archive is severely limited for scientific analyses of interannual and interdecadal variability. This is an issue of fundamental importance to the study of global change.

In response, the National Oceanic and Atmospheric Administration (NOAA) and NASA established an effort to reanalyze the CZCS record by utilizing advances in algorithms that are shared by modern remote sensing missions. In this paper we describe the methods and results of this effort, called the NOAA–NASA CZCS Reanalysis Effort (NCR). Our methods involve the application of (1) recent algorithms to CZCS data to enhance quality and provide consistency with the modern sensors OCTS, SeaWiFS, and MODIS and (2) blending techniques<sup>1</sup> combining satellite data and the extensive *in situ* archives maintained by the National Oceanographic Data Center (NODC) Ocean Climate Laboratory (OCL) to minimize bias and residual error.

Our objective is to provide a high-quality blended satellite *in situ* data set that will enable a consistent view of global surface ocean chlorophyll and the primary production patterns in two observational time segments (1978–1986 and 1996–present) spanning two decades. By reconstructing the historical CZCS data set, we can gain new insights into the processes

and interactions involved in producing the interannual and interdecadal chlorophyll signals.

## 2. Background

### A. Coastal Zone Color Scanner and the Modern Ocean Color Sensors

The CZCS was a demonstration mission with two objectives: (1) to establish the technological and scientific feasibility of mapping ocean phytoplankton pigment concentrations from satellites and (2) to determine the improvements that must be made for successful follow-on ocean color missions. The CZCS amply demonstrated the first objective. It also clearly indicated deficiencies in its design and operations that required correction to meet the scientific objectives of a successor mission. In approximate order of priority, these deficiencies, or required improvements, were

- (1) the need for routine, continuous global synoptic observations;
- (2) better methods to characterize aerosols;
- (3) the need for a dedicated calibration and validation program over the lifetime of the mission;
- (4) methods to account for multiple scattering by aerosols and the interaction between scattering by molecules and aerosols;
- (5) better signal-to-noise ratios (SNRs);
- (6) the need to produce estimates of chlorophyll, not pigment;
- (7) new information about chromophoric dissolved organic matter;
- (8) the need to account for whitecap and foam reflectance; and
- (9) improved pixel navigation.

All the modern global missions meet the scientific requirements for ocean color observations. They are dedicated, routine observational platforms. They contain spectral bands in the near-infrared region of the spectrum to enable improved determination of aerosol characteristics. Dedicated, high-quality *in*



*situ* calibration and validation activities were established before launch. Complex algorithms were developed to account for aerosol multiple scattering and interactions with molecules. SNRs were improved so that all the global missions have at least 500:1 for the visible wavelengths<sup>2</sup> instead of 200:1 for the CZCS.<sup>3</sup> All the missions produce chlorophyll distributions as the primary geophysical product. A new spectral band was included at short wavelengths (near 410 nm) to help determine the distribution and abundance of chromophoric dissolved organic matter. Whitecap and foam reflectance algorithms were developed and refined. Finally, precise navigation methods were developed prelaunch, including improved orbit determination, sensor attitude information, and geolocation algorithms.

#### B. Coastal Zone Color Scanner Algorithm Deficiencies

Of course, some of the deficiencies of the CZCS data set, such as sensor design and operation activities, cannot be improved after the fact. However, recent advances in our understanding of atmospheric and oceanic optical principles that affect ocean color observations can be applied to the archive. The global CZCS data archive generally available from the NASA Goddard Earth Sciences (GES) Distributed Active Archive Center (DAAC) was produced in 1989 with algorithms that were standard for the time.<sup>4</sup> All the subsequent algorithm improvements (AIs) are utilized in the atmospheric correction and bio-optical algorithms for the modern sensors OCTS, SeaWiFS, and MODIS and in future sensors such as the medium resolution imaging spectrometer, Global Imager, and the visible infrared imaging radiometer suite.

The CZCS archive contains eight major algorithm deficiencies compared with modern sensors: (1) calibration, (2) navigation, (3) constant aerosol type, (4) single-scattering approximation for aerosols and no Rayleigh–aerosol interaction, (5) production of pigment rather than chlorophyll, (6) lack of whitecap and foam reflectance correction, (7) lack of correction to Rayleigh scattering because of nonstandard atmospheric pressure, (8) lack of accounting for water-leaving radiance at 670 nm in high chlorophyll.

These deficiencies affect the representation of global chlorophyll and are a major reason for differences observed between the CZCS era and the modern satellite observations of chlorophyll (shown in Section 4).

#### C. Blending of Coastal Zone Color Scanner and *in situ* Data for Analysis of Seasonal Variability

Gregg and Conkright<sup>1</sup> combined the extensive archive of NOAA NODC OCL chlorophyll data (>130,000 profiles) with the global CZCS archive at the GES DAAC using the blended analysis of Reynolds<sup>5</sup> to improve the quality and accuracy of global chlorophyll seasonal climatologies. The blended analysis produced a dramatically different representation of global, regional, and seasonal chlorophyll distributions than the archived CZCS.<sup>1</sup> Generally,

the CZCS appeared to underestimate chlorophyll concentrations globally by 8–35%. On regional and seasonal scales, larger underestimates were common (20–40%, and occasionally the differences exceeded 100%).

Although the blending approach appeared to have improved many of the deficiencies of the CZCS seasonal climatologies, vast areas of the ocean lacked *in situ* observations, limiting the ability of the method to correct for the deficiencies in the CZCS processing. Further improvements by use of the blended method require better CZCS data.

### 5. Summary and Conclusions

We revised the CZCS global ocean chlorophyll archive using compatible atmospheric correction and bio-optical algorithms with modern generation ocean color sensors, such as OCTS, SeaWiFS, and MODIS. The revision involved two components: (1) AI, where CZCS processing algorithms were improved to take advantage of recent advances in atmospheric correction and bio-optical algorithms; and (2) blending, where *in situ* data were incorporated into the final product to provide improvement of residual errors. The combination of the two components is referred to as the NOAA–NASA CZCS reanalysis effort. The results of the NCR are compared with *in situ* data and indicate major improvement from the previously available CZCS archive maintained by the NASA GES DAAC. Blending with *in situ* data produced only a 21% adjustment to the CZCS AI field, compared with a 75% percent adjustment required for the DAAC CZCS. This represented a 72% improvement. Global annual means for the NCR suggested a small overestimate of 9.7% from the CZCS AI, compared with a mean 26% underestimate for the DAAC CZCS blend. Frequency distributions of normalized water-leaving radiances at 520 and 550 nm were in close agreement with expected. Finally, observations of global spatial and seasonal patterns indicated remarkable correspondence with SeaWiFS, suggesting data set compatibility.

This revision can permit a quantitative comparison of the trends in global ocean chlorophyll from 1979–1986, when the CZCS sensor was active, to the present, beginning in 1996 with OCTS, SeaWiFS, and MODIS. The overall spatial and seasonal similarity of the data records of CZCS and SeaWiFS strongly suggests that differences are due to natural variability, although some residual effects that are due to CZCS sensor design or sampling may still exist. We believe that this reanalysis of the CZCS archives can enable identification of interannual and interdecadal change. NCR CZCS data are available through the GES DAAC.

# The Low-Frequency Variability of the Tropical Atlantic Ocean

SIRPA HÄKKINEN

*NASA Goddard Space Flight Center, Greenbelt, Maryland*

KINGTSE C. MO

*Climate Prediction Center, NOAA/NWS/NCEP, Camp Springs, Maryland*

(Manuscript received 16 November 2000, in final form 7 May 2001)

## ABSTRACT

Upper-ocean temperature variability in the tropical Atlantic is examined from the Comprehensive Ocean–Atmosphere Data Set (COADS) as well as from an ocean model simulation forced by COADS anomalies appended to a monthly climatology. The findings are as follows: Only the sea surface temperatures (SST) in the northern Tropics are driven by heat fluxes, while the southern tropical variability arises from wind-driven ocean circulation changes. The subsurface temperatures in the northern and southern Tropics are found to have a strong linkage to buoyancy forcing changes in the northern North Atlantic. Evidence for Kelvin-like boundary wave propagation from the high latitudes is presented from the model simulation. This extratropical influence is associated with wintertime North Atlantic oscillation (NAO) forcing and manifests itself in the northern and southern tropical temperature anomalies of the same sign at depths of 100–200 m as result of a Rossby wave propagation away from the eastern boundary in the wake of the boundary wave passage. The most apparent association of the southern tropical sea surface temperature anomalies (SSTA) arises with the anomalous cross-equatorial winds that can be related to both NAO and the remote influence from the Pacific equatorial region. These teleconnections are seasonal, so that the NAO impact on the tropical SST is the largest at midwinter but in spring and early summer the Pacific remote influence competes with NAO. However, NAO appears to have a more substantial role than the Pacific influence at low frequencies during the last 50 years. The dynamic origin of SSTA is indirectly confirmed from the SST–heat flux relationship using ocean model experiments that remove either anomalous wind stress forcing or atmospheric forcing anomalies contributing to heat exchange.

## 1. Introduction

Variability of the tropical Atlantic has been of wide interest due to its relationship to rainfall in the surrounding landmasses, primarily northeastern Brazil (Nordeste), Sahel, and Angola, Africa (Hastenrath 1978; Moura and Shukla 1981; Folland et al. 1986; Hirst and Hastenrath 1983). These climatic conditions are associated with a dipole of SST anomalies in the Tropics that is the second empirical orthogonal function (EOF) of SST anomalies (Hastenrath 1978; Houghton and Tourre 1992). The existence of this dipole pattern has been questioned (Houghton and Tourre 1992; Enfield and Mayer 1997; Enfield et al. 1999) because the two centers are not anticorrelated with each other at zero lag.

This work will explore the dynamical origin of the decadal variability in the tropical Atlantic Ocean. So far the studies are inconclusive as to whether the decadal variability is internal to the Tropics (Chang et al. 1997) arising from so-called wind–evaporation–SST feedback (Xie and Philander 1994), or driven remotely by the Pacific, or related to the extratropical North Atlantic, or whether a well-defined “decadal” signal in the Atlantic exists at all (Dommenget and Latif 2000). The study by Tourre et al. (1999) finds a tropical–extratropical oscillatory mode with a period of 11.4 yr that displays a

tropical dipole as a part of a joint sea level pressure (SLP) and SST pattern. The SLP pattern associated with their decadal mode resembles the North Atlantic oscillation (NAO). Rajagopalan et al. (1998) found a significant association with NAO and tropical variability at decadal timescales, but arrived at an opposite conclusion by suggesting that the decadal variability is internal to the Tropics. Based on model experiments, Xie and Tanimoto (1998) and Tanimoto and Xie (1999) suggest that the tropical low-frequency variability is likely to derive from extratropical forcing.

The key element in resolving any of the issues related to the tropical decadal variability is to identify the atmospheric forcing associated with the decadal SST anomalies. Tanimoto and Xie (1999) show that a NAO-like SLP pattern dominates the North Atlantic when the tropical north–south temperature gradient has extreme values. The heat flux associated with NAO has three centers of action: subpolar gyre, western subtropics (20°–40°N), and eastern North Atlantic (5°–25°N) off the African coast (Cayan 1992), which are also the centers of the leading EOF mode for surface heat flux (Häkkinen 1999). The center off the African coast coincides with the area of the tropical dipole, and thus a natural linkage between the northern Tropics and NAO exists. The role of local heat flux as a source of northern tropical SST anomalies has been discussed by Carton et al. (1996) and Enfield and Mayer (1997). However, the forcing of southern tropical SST anomalies appear to be problematic. Enfield and Mayer (1997) could not find

Corresponding author address: Sirpa Häkkinen, NASA Goddard Space Flight Center, Code 971, Greenbelt, MD 20771.  
E-mail: hakkinen@gsfc.nasa.gov

any relationship to heat flux while Chang et al. (1997) could construct empirical modes for joint SST–heat flux variability involving both the southern and northern Tropics.

Since heat flux forcing may not be the leading cause of the southern tropical anomalies, we have to explore the role of ocean circulation changes, either driven by local wind stress or remotely forced. One such candidate is the meridional wind variability that appears to be strongly correlated with southern tropical SST anomalies (Bojariu 1997). The work of Philander and Pacanowski (1981a) shows that southerly winds set up a shallow equatorial cell with southerly flow at the surface and northerly flow at subsurface. This cell is associated with upwelling in the southern side and downwelling in the northern side. They also suggest that the southerly winds are responsible for the temperature distribution of the tropical Atlantic where a cold tongue is found in the southeast (SE) sector of the Tropics in an equilibrium state (in a viscous fluid). The other candidate for tropical SST anomalies is the thermohaline circulation that would mainly influence the subsurface temperatures.

Our objective is to study the relationship between the heat flux, wind stress, SST, and upper-ocean temperature anomalies in the Atlantic Tropics. Furthermore we will examine how the SST anomalies in the tropical Atlantic relate to the extratropical ocean, NAO, and the variability in the equatorial Pacific. Analyses are done for SST and atmospheric data based on the Comprehensive Ocean–Atmosphere Response Experiment (COADS; daSilva et al. 1994), which have been used to simulate the oceanic variability from 1946 to 1993. All results from COADS were cross validated by the 51-yr dataset from the National Centers for Environmental Prediction–National Center for Atmospheric Research (NCEP–NCAR) reanalysis.

We will show that the southern tropical SST anomalies are closely linked to the northern tropical subsurface anomalies even though the SST anomalies on either side of the equator are not correlated. This linkage is achieved through the NAO influence, where the subsurface signal propagates from high latitudes to the Tropics. Secondly we will show that SST in the Atlantic Tropics is influenced by the Pacific low-frequency variability. The Pacific and NAO impact on the southern SST takes place mainly through a dynamic adjustment to meridional wind stress anomalies in the central equatorial region, but in the northern Tropics the SST anomalies are driven by local heat flux. The NAO and Pacific impact are not completely separated seasonally, and since SST anomalies can persist for several months, the influence of the two forcings compete in the surface signal. The contents are divided so that the observational and model-simulated datasets along with the ocean model and its forcing, are discussed in section 2. The comparison of observed and simulated SST is presented in section 3a. The variability of the simulated oceanic anomalies in the upper 200 m are discussed in section 3b. The forcing of the northern and southern SST anomalies are considered in section 4. Section 5 presents a summary of interactions between the northern and southern Tropics in the Atlantic.

## 6. Discussion

The Atlantic upper-ocean temperature variability is studied from COADS observations and from an ocean model simulation forced by COADS anomalies appended to a monthly climatology. The starting point of this study is the SST–heat flux relationship: we find that in the northern Tropics the heat flux anomalies force the temperature anomalies, but in the southern Tropics the relationship between the heat flux and temperature anomalies is neutral, and closer to the equator a weak damping is evident. A comparison with a model experiment without wind stress anomalies but retaining atmospheric anomalies contributing to surface heat exchange shows that the southern tropical SST anomalies would be forced by the local atmosphere as opposed to being neutral or damped as in the full simulation (also in the COADS data). This behavior is consistent with a strong coupling between the atmosphere and the ocean, where SSTA practically drives the atmospheric temperature anomalies. The difference in the surface heat exchange between the two experiments suggests that the southern anomalies have to arise from other processes such as wind-driven circulation changes. Our study suggests that the initial appearance of SSTA in the southern Tropics is a forced response to ocean circulation changes, but does not exclude the possibility of a subsequent atmospheric response as put forward in Robertson et al. (2000).

Specifically the low-frequency southern tropical SST variability is found to be tied to the cross-equatorial wind stress. Based on Philander and Pacanowski (1981a) the meridional wind stress in the Tropics leads to a shallow overturning cell at the equator and pycnocline changes along the boundaries such that southerly winds would cause a strong cold tongue in the eastern southern Tropics. Analogous to this, the northerly wind stress component would lead to deeper pycnocline and warm SST anomalies in the STA region. The significance of the meridional wind component has been brought up by Bojariu (1997) in search of connections between NAO and the tropical variability. We find a connection between NAO and STA that is quite specific to the boreal winter season and that during spring–early summer the Pacific remote forcing is also associated with STA, again through a meridional wind stress signal at the equator.

This difference in the dynamic origin of the northern and southern variability is limited to the surface. At the subsurface (at 100 m and below) the model results show that temperature anomalies of the same sign exist on both sides of the equator. This in-phase relationship is expected from the studies of oceanic adjustment to high-latitude buoyancy forcing that would give rise to equatorward-propagating boundary waves, transforming into equatorial Kelvin waves along the equator and branching into both hemispheres on the eastern boundary and generating westward-propagating Rossby waves in their wake (Wajsbowicz 1986; Kawase 1987). The wave dynamics of the extratropical origin determine that the anomalies at depth on both sides of the equator are of the same sign.

# Assessment of the relative accuracy of hemispheric-scale snow-cover maps

DOROTHY K. HALL,<sup>1</sup> RICHARD E. J. KELLY,<sup>2</sup> GEORGE A. RIGGS,<sup>3</sup> ALFRED T. C. CHANG,<sup>1</sup>

JAMES L. FOSTER<sup>1</sup>

<sup>1</sup>*Hydrological Sciences Branch, NASA Goddard Space Flight Center, Code 974, Greenbelt, MD 20771, U.S.A.*

<sup>2</sup>*Goddard Earth Sciences and Technology Center, University of Maryland, Baltimore County, 1000 Hilltop Circle, Baltimore, MD 21250, U.S.A.*

<sup>3</sup>*Science Systems and Applications, Inc., Lanham, MD 20706, U.S.A.*

**ABSTRACT.** There are several hemispheric-scale satellite-derived snow-cover maps available, but none has been fully validated. For the period 23 October–25 December 2000, we compare snow maps of North America derived from the Moderate Resolution Imaging Spectroradiometer (MODIS) and operational snow maps from the U.S. National Oceanic and Atmospheric Administration (NOAA) National Operational Hydrologic Remote Sensing Center (NOHRSC), both of which rely on satellite data from the visible and near-infrared parts of the spectrum; we also compare MODIS maps with Defense Meteorological Satellite Program (DMSP) Special Sensor Microwave/Imager (SSM/I) passive-microwave snow maps for the same period. The maps derived from visible and near-infrared data are more accurate for mapping snow cover than are the passive-microwave-derived maps, but discrepancies exist as to the location and extent of the snow cover even between operational snow maps. The MODIS snow-cover maps show more snow in each of the 8 day periods than do the NOHRSC maps, in part because MODIS maps the effects of fleeting snowstorms due to its frequent coverage. The large ( $\sim 30$  km) footprint of the SSM/I pixel, and the difficulty in distinguishing wet and shallow snow from wet or snow-free ground, reveal differences up to  $5.33 \times 10^6$  km<sup>2</sup> in the amount of snow mapped using MODIS vs SSM/I data. Algorithms that utilize both visible and passive-microwave data, which would take advantage of the all-weather mapping capability of the passive-microwave data, will be refined following the launch of the Advanced Microwave Scanning Radiometer (AMSR) in the fall of 2001.

## INTRODUCTION

The areal extent of snow cover has been monitored continuously from satellite observations by the U.S. National Oceanic and Atmospheric Administration (NOAA) since 1966 (Matson and others, 1986). Although several weaknesses have been identified (Robinson 1993) in the long-term operational snow product, it is nevertheless the longest climatological time series of snow cover available. Passive-microwave maps of snow cover have been produced since 1978, providing information on snow extent as well as some information on snow-water equivalent. In order to improve the snow-cover record to optimize future long-term climate studies, and as input to general circulation models, it is important to develop an objective way of mapping snow globally, if trends in snow cover, such as those discussed in Brown (1997), are to be validated. In addition, the accuracy of the snow-cover input data needs to be verified in order to establish the accuracy of the model output (Derksen and LeDrew, 2000).

In December 1999, the Moderate Resolution Imaging Spectroradiometer (MODIS) sensor was launched by the National Aeronautics and Space Administration (NASA), and some daily, global maps of snow cover at a spatial resolution of 500 m began to be available in February 2000. Snow maps have been orderable through the U.S. National Snow and Ice Data Center, Boulder, CO, since 13 September 2000. In this paper, we compare 8 day composite MODIS

snow maps, NOAA/National Operational Hydrologic Remote Sensing Center (NOHRSC) operational maps, and passive-microwave-derived maps from the Defense Meteorological Satellite Program (DMSP) Special Sensor Microwave/Imager (SSM/I). Each map is known to have a unique set of problems or limitations. The 30 m resolution Landsat Enhanced Thematic Mapper Plus (ETM+) and the NOAA operational product, the Interactive Multisensor Snow and Ice Mapping System (IMS), are used as ancillary data and are considered "ground truth" for this work.

## BACKGROUND

### MODIS-derived snow maps

The MODIS snow-mapping algorithm is fully automated, which makes the results consistent from scene to scene. The algorithm uses reflectances in MODIS bands 4 (0.545–0.565  $\mu\text{m}$ ) and 6 (1.628–1.652  $\mu\text{m}$ ), uncorrected for atmospheric effects, to calculate the normalized-difference snow index (NDSI) (Hall and others, in press). Snow cover is mapped using a grouped-criteria technique algorithm. A pixel will be mapped as snow if the NDSI is  $\geq 0.4$  and reflectance in MODIS band 2 (0.841–0.876  $\mu\text{m}$ ) is  $\geq 11\%$ . However, if the MODIS band 4 reflectance is  $< 10\%$ , then the pixel will not be mapped as snow even if the other criteria are met. This prevents pixels containing very dark targets from being



mapped erroneously as snow. MODIS bands 1 (0.620–0.670  $\mu\text{m}$ ) and 2 (0.841–0.876  $\mu\text{m}$ ) are used to calculate the normalized-difference vegetation index (NDVI). An additional test using the NDSI and NDVI is used to improve the detection of snow in dense forests (Klein and others, 1998). A cloud mask (Ackerman and others, 1998) and a land/water mask are inputs to the MODIS snow-cover maps.

## DISCUSSION AND CONCLUSION

Analysis of the eight time periods, beginning on 23 October and ending on 25 December 2000, reveals that the MODIS maps nearly always show more snow cover than do the NOHRSC maps. MODIS, because of its frequent coverage, permits the mapping of some fleeting snowstorms that may be missed (either accidentally or intentionally) in both the NOAA operational products (NOHRSC and IMS). Since the NOHRSC and IMS products are subjective, the analysts who construct the maps may use ground data, in addition to satellite data, to refine the snow maps. Some minor snow events, located at the edges of areas mapped as snow by both maps, may not be deemed significant enough to label as snow if the snow cover is not continuous or persistent, a common occurrence especially at the beginning of the snow season. Or, the mapping techniques will miss the effects of these storms if the maps are not produced on a frequent basis. In general, there were not eight NOHRSC maps for each 8 day period, while the MODIS maps were produced from 8 days of data (except the 1–7 November period). NOAA's IMS product is produced daily. The greater temporal resolution of the MODIS maps is advantageous for mapping maximum snow cover, because several swaths of data may be obtained on the same day.

However, the MODIS maps exaggerate the amount of snow in some locations, as determined from comparisons with NOHRSC, IMS and ETM+ images. This is obvious in the Pacific Northwest (western Washington, Oregon and northern California). While there is snow in these locations — often only scattered snow cover — the MODIS maps show nearly continuous snow cover in some cases. The binning technique to map the 500 m resolution MODIS maps into  $1/4^\circ \times 1/4^\circ$  resolution maps may permit overestimation of snow cover in some cases. Where only a small amount of the cell is snow-covered, in these early MODIS products, the entire  $1/4^\circ \times 1/4^\circ$  pixel will be mapped as snow. An improved binning technique is under development. Maps will be produced at  $1/20^\circ \times 1/20^\circ$ , or 5.6 km resolution, beginning in the fall of 2001, and fractional snow cover will be provided as well. This should enhance the utility of the maps considerably.

A modification of the Chang and others (1987) algorithm, and the Grody and Basist (1996) SSM/I algorithm were studied, and the Grody and Basist (1996) algorithm was found to map even less snow cover in the early part of the snow season than did the Chang and others (1987) modified algorithm. It was therefore decided that the Chang and others (1987) modified algorithm was superior for the purposes of this work.

As the winter progresses, agreement between the MODIS and SSM/I maps improves. This was also noted by Armstrong and Brodzik (1999) in their comparison study using the SSM/I maps and the NESDIS weekly maps. As the snow deepens during winter, and the temperatures are

consistently colder, the SSM/I mapping improves, and the agreement between the visible and passive-microwave maps improves. Areas of discrepancy are still present, however, especially in coastal areas where mixed pixels of SSM/I data erroneously map the coastal areas as snow-free when in fact there is snow. An example of this may be seen in northern Quebec on the 18–25 December 2000 MODIS/SSM/I difference map (Fig. 2).

The results herein are specific to the North American continent. There are likely to be circumstances on other continents that affect the results of snow mapping with the MODIS algorithms, and these can only be discovered by performing such studies on other continents.

With the launch of NASA's Aqua satellite in 2001, snow-mapping algorithms will be developed using the Advanced Microwave Scanning Radiometer–EOS (AMSR-E) sensor (Chang and Koike, 2000) that should utilize the superior mapping capabilities of the visible sensors, and the all-weather capabilities of the passive-microwave sensors (Tait and others, 2000). The improved spatial resolution of the AMSR-E data (up to 12.5 km), relative to the coarser resolution of the SSM/I, will facilitate comparison with visible and near-infrared snow maps.

Near-term improvements in the MODIS snow-mapping algorithm include providing the 8 day composite snow-cover maps at 5.6 km resolution, and improving the usage of the cloud mask (Ackerman and others, 1998), so that fewer clouds are mapped erroneously as snow.

While the intent of this work was not to establish which product is the most accurate, it is obvious that the passive-microwave data are less accurate in terms of mapping total snow-covered area. This is due to the relatively low ( $\sim 30$  km) spatial resolution of the data, and the fact that the wet snow and shallow snow may not be mapped by the existing automated passive-microwave algorithms, especially in the early part of the snow season.

Relative errors in snow-cover mapping, using both visible/near-infrared and passive-microwave maps, are easier to ascertain than absolute errors. This is because it is very often impossible, in retrospect, to determine which map is the most accurate, or precisely where the snow was located. A technique that combines ground measurements with determination of snow-mapping accuracy in different land-cover types (e.g. Hall and others, 2001) is an attempt to begin to assess the absolute accuracy of snow-cover maps.

MODIS and NOHRSC maps often agree very well, except that the MODIS nearly always maps more snow cover than does the NOHRSC (Table 1). MODIS maps show more snow than the NOHRSC maps, especially at the beginning of the snow season when the more frequent temporal coverage of MODIS permits mapping of shallow snow deposits from fleeting storms. However, we do not know which map is the more accurate since none of the hemispheric-scale snow maps has been fully validated. We can only study the relative accuracy of the maps at this time, augmented by accuracy assessments in selected locations where we have access to either ground measurements or Landsat ETM+ data.

## MODIS snow-cover products

Dorothy K. Hall<sup>a,\*</sup>, George A. Riggs<sup>b</sup>, Vincent V. Salomonson<sup>c</sup>,  
Nicolo E. DiGirolamo<sup>b</sup>, Klaus J. Bayr<sup>d</sup>

<sup>a</sup>*Hydrological Sciences Branch, NASA/Goddard Space Flight Center, Code 974, Greenbelt, MD 20771, USA*

<sup>b</sup>*Science Systems and Applications, Inc., Lanham, MD 20706, USA*

<sup>c</sup>*NASA/Goddard Space Flight Center, Code 900, Greenbelt, MD 20771, USA*

<sup>d</sup>*Department of Geography, Keene State College, Keene, NH 03431, USA*

Received 1 April 2001; received in revised form 20 December 2001; accepted 1 February 2002

### Abstract

On December 18, 1999, the Terra satellite was launched with a complement of five instruments including the Moderate Resolution Imaging Spectroradiometer (MODIS). Many geophysical products are derived from MODIS data including global snow-cover products. MODIS snow and ice products have been available through the National Snow and Ice Data Center (NSIDC) Distributed Active Archive Center (DAAC) since September 13, 2000. MODIS snow-cover products represent potential improvement to or enhancement of the currently available operational products mainly because the MODIS products are global and 500-m resolution, and have the capability to separate most snow and clouds. The MODIS snow-mapping algorithms are automated, which means that a consistent data set may be generated for long-term climate studies that require snow-cover information. Extensive quality assurance (QA) information is stored with the products. The MODIS snow product suite begins with a 500-m resolution, 2330-km swath snow-cover map, which is then gridded to an integerized sinusoidal grid to produce daily and 8-day composite tile products. The sequence proceeds to a climate-modeling grid (CMG) product at 0.05° resolution, with both daily and 8-day composite products. Each pixel of the daily CMG contains fraction of snow cover from 40% to 100%. Measured errors of commission in the CMG are low, for example, on the continent of Australia in the spring, they vary from 0.02% to 0.10%. Near-term enhancements include daily snow albedo and fractional snow cover. A case study from March 6, 2000, involving MODIS data and field and aircraft measurements, is presented to show some early validation work.

© 2002 Elsevier Science Inc. All rights reserved.

### 1. Introduction

Snow-cover maps of the Northern Hemisphere have been available since 1966 from the National Oceanic and Atmospheric Administration (NOAA). These maps have continually been improved as new satellite data have become available. These maps, however, are not global and they rely on analysts to fine-tune the maps. For operational use, this is an advantage. However, for long-term climate studies, it is imperative to have a data set that is developed using an objective technique for snow mapping so that the data from the maps can be consistent when used as input to climate models.

On December 18, 1999, the Earth Observing System (EOS) Terra spacecraft was launched with a complement of five instruments, one of which is the Moderate Resolution Imaging Spectroradiometer (MODIS). MODIS data are now being used to produce snow-cover products from automated algorithms at Goddard Space Flight Center in Greenbelt, MD. The products are transferred to the National Snow and Ice Data Center (NSIDC) in Boulder, CO, where they are archived and distributed via the EOS Data Gateway (EDG).

The MODIS snow-cover maps represent a potential improvement relative to hemispheric-scale snow maps that

are available today mainly because of the improved spatial resolution and snow/cloud discrimination capabilities of MODIS, and the frequent global coverage. Their accuracy, however, has not yet been established, nor has the accuracy of existing operational maps. The difficulty in establishing the accuracy of any of these maps is that it is not known which map is the “truth” (if any) and the techniques used to map snow cover in the various maps are different, resulting in different products. The improved spatial resolution of the MODIS snow maps (500 m), relative to snow maps derived from other available sensors, e.g. NOAA’s Advanced Very High Resolution Radiometer (AVHRR) at 1.1-km resolution, should benefit hydrologists for snow-cover mapping. In this paper, we describe the MODIS snow products, and discuss a case study of early validation efforts from a field and aircraft experiment near Keene, NH, in March 2000, and field measurements in December 2000.

### 2. Background

#### 2.1. Instrument descriptions

##### 2.1.1. MODIS

MODIS is an imaging spectroradiometer that employs a cross-track scan mirror, collecting optics, and a set of

individual detector elements to provide imagery of the Earth's surface and clouds in 36 discrete, narrow spectral bands from approximately 0.4 to 14.0  $\mu\text{m}$  (Barnes, Pagano, & Salomonson, 1998). Key land-surface objectives are to study global vegetation and land cover, global land-surface change, vegetation properties, surface albedo, surface temperature, and snow and ice cover on a daily or near-daily basis (Justice et al., 1998). The spatial resolution of the MODIS instrument varies with spectral band, and ranges from 250 m to 1 km at nadir.

#### 2.1.2. MODIS Airborne Simulator (MAS)

The MAS is a spectroradiometer designed to acquire calibrated radiances. The spectral coverage and radiometric response of an existing multichannel instrument were modified to approximate the narrow spectral bands of the MODIS for measuring scientific parameters of cloud and terrestrial surface targets (King et al., 1996). The MAS, with 50 spectral bands in the wavelength range from 0.55 to 14.2  $\mu\text{m}$ , is flown aboard a NASA ER-2 research aircraft at an altitude of about 20 km. Data from MAS channels 1–10, in the visible, near-infrared and short-wave-infrared parts of the spectrum, are discussed in this paper. The MAS views  $43^\circ$  on either side of nadir with an Earth swath width of 37.25 km. The 15-cm aperture spatial instantaneous field-of-view is 2.5 mrad, or 50-m spatial resolution at nadir from the nominal aircraft height.

#### 2.1.3. The Landsat Enhanced Thematic Mapper Plus (ETM+)

The ETM+ was launched on April 15, 1999, on the Landsat-7 satellite (<http://www.landsat.gsfc.nasa.gov/project/satellite.html>). The ETM+ has eight discrete bands ranging from 0.45 to 12.5  $\mu\text{m}$ , and the spatial resolution ranges from 15 m in the panchromatic band, to 60 m in the thermal-infrared band. All of the other bands have 30-m resolution. ETM+ data can be accessed as browse products and ordered from the USGS EROS Data Center in Sioux Falls, SD from the following Web address: <http://www.edcns17.cr.usgs.gov/EarthExplorer/>. ETM+ data provide a high-resolution view of snow cover that can be compared with the MODIS and operational snow-cover products. However, ETM+ data are only acquired once every 16 days and are therefore not frequent enough for mapping changing snow-cover conditions operationally.

### 2.2. Snow maps

#### 2.2.1. NOAA operational snow maps

2.2.1.1. *National Environmental Satellite, Data and Information Service (NESDIS).* The Satellite Analysis Branch of NOAA's NESDIS began to generate Northern Hemisphere Weekly Snow and Ice Cover analysis charts derived from NOAA's GOES and POES visible satellite

imager, in November 1966. Maps were manually constructed and the spatial resolution of the charts was 190 km. However, since 1997, a new Interactive Multi-Sensor Snow and Ice Mapping System (IMS) is used by analysts to produce products daily at a spatial resolution of about 25 km, and utilizes a variety of satellite data to produce the maps (Ramsay, 1998). NOAA also produces a daily product, developed by automated techniques, which uses visible, near-infrared and passive-microwave data to map snow cover, and agrees in 85% of the cases studied, with the IMS product (Romanov, Gutman, & Csiszar, 2000).

2.2.1.2. *The National Operational Hydrologic Remote Sensing Center (NOHRSC) maps.* NOHRSC snow-cover maps, generated by National Weather Service NOHRSC hydrologists, are distributed electronically in near real time, to local, state and federal users during the snow season (Carroll, 1995). The NOHRSC 1-km maps are generated primarily from the NOAA polar-orbiting satellites and the Geostationary Orbiting Environmental Satellite (GOES) satellites to develop daily digital maps depicting the areal extent of snow cover for the coterminous United States, and Alaska, and portions of southern Canada.

### 4. Discussion and conclusion

A sequence of MODIS snow-cover products is presented. The swath products are mapped to the integerized sinusoidal grid to create the daily tile product. Eight days of the daily tile products are used to produce the 8-day composite tile product. These products are at 500-m resolution. The CMG product is produced at  $0.05^\circ$  ( $\sim 5.6\text{-km}$ ) resolution and consists of daily and 8-day composite products. Examples of the products are shown, focusing on the site of a field and aircraft experiment from March 6, 2000, and fieldwork on December 23, 2000. The MODIS snow map shows patchy snow cover on March 6th, as confirmed by the field measurements. However, nearly complete snow cover is mapped near Keene on December 23rd, which is an over-estimation of snow cover as compared to the ETM+-derived map for the same day, as confirmed by field measurements but is likely due to the greater resolution of the MODIS image relative to the ETM+ image.

Other work shows that the MODIS snow-cover maps compare favorably with current operational maps (Hall et al., in press), and perform better than do passive microwave-derived snow-cover maps during the daytime and in the fall months in the Northern Hemisphere when the snow is still wet.

Future enhancements to the MODIS snow maps include daily snow albedo (Klein et al., 2000), which should be available in the fall of 2002, and fractional snow cover at 500-m spatial resolution. Future re-processing will allow all of the MODIS snow maps to be processed in a consistent manner.

# Satellite observation of Chromophoric Dissolved Organic Matter (CDOM) variability in the wake of hurricanes and typhoons

Frank E. Hoge

National Aeronautics and Space Administration, Goddard Space Flight Center, Wallops Flight Facility, Wallops Island, Virginia, USA

Paul E. Lyon

E. G. & G. Inc., Goddard Space Flight Center, Wallops Flight Facility, Wallops Island, Virginia, USA

Received 13 March 2002; accepted 5 June 2002; published 4 October 2002.

[1] Satellite observation of Chromophoric Dissolved Organic Matter (CDOM) absorption coefficient variability in the wake of numerous hurricanes and typhoons is reported here for the first time. Storm-induced vertically-mixed CDOM from deeper depths has a higher absorption coefficient than the photochemically degraded CDOM within the undisturbed pre-storm upper mixed layer. Principal findings are: (1) Little variability is observed prior to storm encounter at which time the CDOM-defined wake rapidly develops a notable right side asymmetry. (2) The more robust right-side CDOM absorption coefficient elevation is visible up to ~30 days depending on storm intensity. In a way that is similar to existing sea surface temperature imagery applications, the techniques in this paper are proposed as a complementary new research tool for the study of atmosphere-ocean interactions. *INDEX TERMS*: 4504 Oceanography: Physical: Air/sea interactions (0312); 4572 Oceanography: Physical: Upper ocean processes; 4847 Oceanography: Biological and Chemical: Optics; 4552 Oceanography: Physical: Ocean optics. **Citation**: Hoge, F. E., and P. E. Lyon, Satellite observation of Chromophoric Dissolved Organic Matter (CDOM) variability in the wake of hurricanes and typhoons, *Geophys. Res. Lett.*, 29(19), 1908, doi:10.1029/2002GL015114, 2002.

## 1. Introduction

[2] Dissolved organic matter (DOM) in seawater represents one of the largest reservoirs of reduced carbon on the earth's surface [Hedges and Farrington, 1993]. There is as much carbon in DOM in the oceans as there is carbon in CO<sub>2</sub> in the atmosphere [Hansell and Carlson, 1998]. The absorbing form can be remotely observed and is frequently described as chromophoric or colored dissolved organic matter (CDOM). The CDOM absorption coefficient is quite easily retrieved from satellite observations by inversion of an oceanic radiance model [Hoge et al., 1995; Hoge et al., 2001]. However, this CDOM absorption coefficient varies (1) temporally as downwelling irradiance photodegrades or photo-oxidizes the material in the upper ocean layer and (2) with depth since CDOM molecules receive less irradiance at-depth and thus incur less photodegradation [Vodacek et al., 1997; Chen and Bada, 1992; Siegel and Michaels, 1996]. Vertical differences in the CDOM absorption coefficient are especially pronounced under stratified conditions where a strong thermocline acts as an effective barrier

separating the overlying water mass (which is exposed to high solar radiation) from the underlying water mass (which receives little or no insolation). During the period of maximum hurricane activity (July–September) stratification of the oceans of the northern hemisphere are at a maximum, extending as far north as hurricanes are sustained.

[3] Prior to the work reported herein, the principal satellite-derived observations of hurricane forcing of the upper ocean mixed layer have been via sea surface temperature (SST) [Bates and Smith, 1985; Stramma et al., 1986; Shay et al., 1992; Shay et al., 2000]. These observations (and modeling studies) have shown that the maximum SST response generally occurs to the right of the storm track and is known as the rightward bias. This rightward bias of the maximum SST cooling is dominated by vertical mixing processes [Shay et al., 1992; Price et al., 1994]. Sea surface fluxes and upwelling underneath the hurricane track generally contribute less to the SST cooling pattern [Jacob et al., 2000].

[4] The application of satellite-derived inherent optical properties imagery to vertical redistribution of chromophoric dissolved organic matter (CDOM) by hurricanes and typhoons is reported here for the first time. Herein, we hypothesize that CDOM, vertically mixed from deeper depths as a result of storm-forcing, provides the source of the CDOM absorption coefficient increases observed in the SeaWiFS retrievals described in this paper. The techniques in this paper are proposed as a complementary new research tool for the study of atmosphere-ocean interaction in much the same way sea surface temperature imagery has historically been used.

## 2. Methods

### 2.1. Retrieval of Oceanic Inherent Optical Properties (IOP) from SeaWiFS Water-Leaving Reflectances

[5] All the SeaWiFS global area coverage (GAC) Level 2 reflectances for the complete September 1997 to December 2001 were processed by linear matrix inversion of an oceanic radiance model [Hoge and Lyon, 1996; Hoge et al., 1999a; Hoge et al., 1999b; Hoge and Lyon, 1999; Hoge et al., 2001]. The inherent optical properties (IOPs), CDOM absorption coefficient, phytoplankton absorption coefficient, and backscattering coefficient, at each invertible pixel are binned into 0.09 square degree bins. When a bin contains more than one valid pixel for a single day of



orbits, then the pixels are averaged together. Multiple pixels in a single bin typically exist only near the polar regions due to the SeaWiFS global coverage period of  $\sim 2$  days. The complete global averaged binned data are called daily global maps.

[6] The oceanic CDOM variability images to be discussed later were created from a 25-day sliding mean global IOP map, where 24 previous daily global maps and the current day's global map are averaged together. Thus, for the next day's image, the oldest day's data is dropped and a new day's data is included to constitute the new 25 day mean. The process is progressively repeated as each oldest day is dropped and a new day is added. Due to orbit configurations and cloud cover, each sliding mean bin does not necessarily contain an average of 25 valid pixels, but is usually an average of less than 12 valid pixels. The 25-day sliding mean results in more contiguous imagery by removing the clouds from the images and reduces uncertainty in the retrieved IOPs (effects caused by errors in the atmospheric correction to the reflectance spectra).

[7] Data used in the hurricane and typhoon track line extractions (encounter diagrams to be discussed) were produced with a 3-day sliding mean of the daily global maps to eliminate artifacts in the encounter diagrams that are caused by the global coverage period of SeaWiFS. The 3-day sliding mean also allows better estimates of the duration and rate of the increase seen in the CDOM absorption coefficient than the 25-day sliding mean data.

### 3. Results

[8] We have observed CDOM wakes in at least 40 hurricanes/typhoons during global survey of the 1997, 1998, 1999, 2000 CDOM signatures derived from SeaWiFS reflectances. Although our studies are continuing, CDOM wakes have been found in  $\sim 50\%$  of the hurricanes/typhoons in the North Atlantic Ocean and Eastern Pacific Ocean. In the Western Pacific Ocean the occurrence of CDOM wakes is highly variable ranging from  $\sim 10\%$  to  $50\%$  of the typhoons depending on the location: typhoons that traverse low CDOM areas were much more likely to leave tracks than the typhoons that mainly traverse very high CDOM absorption waters (the latter providing little visual contrast).

### 4. Summary and Discussion

[14] It has been shown that wakes from major oceanic storm events can be identified by their CDOM absorption coefficient increases measured relative to (a) pre-storm values, (b) adjacent undisturbed regions, (c) post-storm photochemically degraded surface waters. The right-side asymmetry seen in the CDOM absorption coefficient is consistent with historic sea surface temperature findings from satellites, aircraft, ships, and buoys. CDOM absorption coefficient increases of  $\sim 100\text{--}200\%$  are common. Non-contemporaneous ship data [Vodacek *et al.*, 1997] strongly suggest that these CDOM absorption coefficient increases are due to vertically-mixed [Shay *et al.*, 1992; Price *et al.*, 1994] water whose CDOM has not yet been photochemically degraded to the lower prevailing values routinely found at the sea surface. No change in the average number of carbon atoms in the water column is inferred from these

observations; simply a higher optical activity for those chemical species brought to the surface by the storm [Siegel and Michaels, 1996]. While satellites can offer observations over large space and time scales, cloud cover can severely limit timely observations. This is true of SST as well as ocean color measurements. The delay time until the cloud cover clears can induce unwanted diurnal heating in the case of (a) SST and (b) CDOM photodegradation/mixing in the case of ocean color. The photodegradation is however mitigated somewhat by the reduced sunlight due to cloud cover.

[15] The current state of our analysis of the SeaWiFS post hurricane/typhoon imagery permits us to retrieve CDOM absorption changes over oceanic basin wide scales. We have made no attempt to tie these findings to observations made by other investigators using data acquired from satellite SST imagery or to any physical oceanographic data that may have been collected by moorings or drifters (if these even exist for hurricane Gert or super typhoon Keith). These observations were discovered in the course of developing SeaWiFS CDOM absorption imagery to observe its distribution in the world's oceans. One of the goals of this paper is to introduce new observational methods to the physical oceanography and meteorological communities who study coupling of intense storms into the upper ocean. We hope that this new tool will complement the physical oceanographic measurements now in use. The large dynamic range of the change in CDOM absorption coefficient may enable more detailed studies of the effects caused by ocean and atmosphere interactions.

[16] The enhanced CDOM absorption coefficient has been seen in numerous named storms and can possibly be seen in less intense storms but these lesser magnitude storms have not yet been sought nor studied by our group. However, it seems safe to conjecture that their effects may eventually be seen under certain pre-existing/storm-driven wind, wave, and current conditions. The CDOM increases have been seen within the tropical storm portions of Gert and Keith (tropical storm wind speeds of  $\sim 17$  to  $\sim 33$  m/s). We have seen, but have not yet reported, significant CDOM increases due to known periodic sustained wind events. Thus, the threshold wind speed for CDOM absorption coefficient increases is yet to be established for specifically defined or pre-existing oceanographic conditions.

[17] The phytoplankton absorption coefficient showed no significant signature within the imagery and therefore are not shown. Absence of a phytoplankton bloom is validated by the concurrent absence of an increase in the backscattering coefficient that would accompany phytoplankton growth.

[18] While outside the scope of this paper, numerous studies can be devised by the reader using this CDOM absorption coefficient signature. First, nutrients have been found to be correlated with CDOM [Chen and Bada, 1992] and thus studies of the absence of detectable nutrient-facilitated phytoplankton growth and its associated absorption within the CDOM wake is recommended. Second, assuming a known photobleaching rate and upwelling/vertical mixing coefficients, an estimate of the storm energy transfer rate may be possible. Third, an investigation of the intensity and duration of the signature relative to location may be of interest.

# Air and Water Monitoring for Homeland Security

*Paul R. Houser\**

---

Last year's terrorist attacks on the World Trade Center and on the Pentagon have heightened our awareness of actual and potential threats to our nation's safety and security. Assuring homeland security has become a national priority (Bush, 2001), meaning that we must take decisive actions both to prevent and to mitigate future homeland security threats. On 8 October 2001, President George W. Bush established the Office of Homeland Security with the mission to "...develop and coordinate the implementation of a comprehensive national strategy to secure the United States from terrorist threats or attacks" (Executive Order 13228). Homeland security is a challenge of monumental scale and complexity, requiring a comprehensive, long-term strategy that involves partnership with State and local governments, the private sector, and citizens. The president's strategy will build an emergency management system that is better able to manage not just terrorism but all hazards affecting our nation and its people.

A critical element of homeland security lies in the vitality of our environment, which is primarily defined by the availability and quality of our air and water resources. Homeland security efforts must therefore include advanced understanding, assessment, and prediction of natural and human-induced variations in our environment, enabling retooled policies and planning, allocation of resources, and partnership strategies. Whether the cause is a terrorist, an accident, or a natural disaster, the efforts needed to avoid and to alleviate air- and water-related threats are similar. We must be able to identify and assess the magnitude of current threats, to evaluate various preventative and corrective actions, and to predict future threats.

Over the past few decades, we have made substantial progress in our ability to monitor, assess, and predict air quality and water resources. However, only the scientific community has effectively realized these developments with marginal returns to management and operations. Now, more than ever, we must take action to make the necessary links for improved homeland security through knowledge-added disaster preparation, assessment, and mitigation. We must also view homeland air and water security at the global and multi-national levels, encompassing not only terrorism and vandalism but also natural disasters and potential adversities from human-induced change.



Proposed Hydrospheric State Mission to observe soil moisture and soil freezing.

---

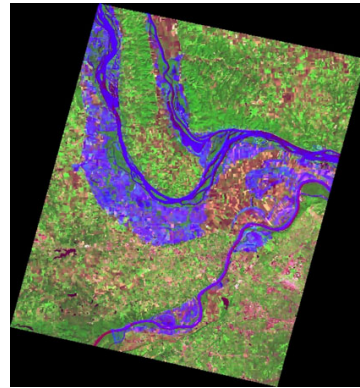
\* Published in August 2002 special NASA Earth Science Enterprise issue of *Earth Observation Magazine*, 11(8):33–36.

## Planning, Communication, and Implementation

A traditional disconnect between the environmental management and the scientific research communities has prevented the definition of a mutually beneficial research agenda and the free flow of information to address new threats. As a result, a significant time lag occurs before scientific advancements are implemented to the benefit of society. Environmental management policy is often based on outdated knowledge and technology. Further, scientific research is often performed without understanding stakeholder needs. This paradigm lock has come about because the two main groups have become isolated: scientists by the lack of proven utility of their findings and stakeholders by legal and professional precedence and by disaggregated institutions. For example, global change research is largely focused on mean climate impacts (such as global temperature) of century-scale greenhouse gas changes, while environmental managers need a reliable prediction of extreme event variations (such as floods and droughts) in the seasonal to decadal timeframe.

We must take decisive action to eliminate this paradigm lock. It is essential that we continuously modernize and integrate our air and water observation, assessment, and prediction tools to provide reliable and timely information for homeland security. But this information is meaningless unless accompanied by timely and adequate mitigation action. Communication must be established to transmit information to users quickly, to evaluate various response options in a prediction system, to enable planning, and to take decisive mitigation action. The NOAA weather radio and the network of media resources can deliver hazard emergency messages to the public effectively. We must encourage and demonstrate similar bridge-building dialogue between scientists and policy makers to establish real pathways to define a society-relevant research agenda and to transfer state-of-the-art data and tools to the users who need them.

We will likely be surprised by future attacks and by environmental variability, but we do not have to be unprepared. One way to reduce the adverse impact of surprise is to maintain an acceptable level of preparedness at all times. We must improve terrorism and hazard response plans so that when improved warnings become available, decision makers will know how to take action. Improving both air and water monitoring, prediction, and preparation will allow warning and response to work synergistically, providing enhanced homeland security.



Flood images in the area around St. Louis, Missouri, in July and August 1993 produced by the Institute for Technology Development/Space Remote Sensing Center (ITD/SRSC). The broad blue areas, derived from ERS-1 radar data, show the extent of the flooding and are overlaid on an older SPOT image to delineate the rivers under normal circumstances.

# Surface Soil Moisture Retrieval and Mapping Using High-Frequency Microwave Satellite Observations in the Southern Great Plains

THOMAS J. JACKSON AND ANN Y. HSU

*USDA-ARS Hydrology and Remote Sensing Laboratory, Beltsville, Maryland*

PEGGY E. O'NEILL

*Hydrological Sciences Branch, Laboratory for Hydrospheric Processes, NASA Goddard Space Flight Center, Greenbelt, Maryland*

(Manuscript received 16 November 2001, in final form 10 July 2002)

## ABSTRACT

Studies have shown the advantages of low-frequency (<5 GHz) microwave sensors for soil moisture estimation. Although higher frequencies have limited soil moisture retrieval capabilities, there is a vast quantity of systematic global high-frequency microwave data that have been collected for 15 yr by the Special Sensor Microwave Imager (SSM/I). SSM/I soil moisture studies have mostly utilized antecedent precipitation indices as validation, while only a few have employed limited ground observations, which were typically not optimal for this particular type of satellite data. In the Southern Great Plains (SGP) hydrology experiments conducted in 1997 and 1999, ground observations of soil moisture were made over an extended region for developing and validating large-scale mapping techniques. Previous studies have indicated the limitations of both the higher-frequency data and models for soil moisture retrieval. Given these limitations, an alternative retrieval technique that utilizes multipolarization observations was implemented and tested for the SGP region. A technique for extracting algorithm parameters from the observations was developed and tested. The algorithm was then used to produce soil moisture maps of the region for the two study periods.

## 1. Introduction

The potential of passive microwave remote sensing for measuring surface soil moisture has been demonstrated over a range of microwave frequencies (Choudhury and Golus 1988; Paloscia et al. 1993; Lakshmi et al. 1997; Drusch et al. 2001) and a variety of platforms (Wang 1985; Jackson et al. 1999; Jackson and Hsu 2001). These studies clearly show the advantages of low-frequency (<5 GHz) microwave sensors for this application. Although low-frequency sensors are recognized as the best direction for future soil moisture measurement systems, there is still a good reason in the meantime to consider the use of higher frequencies: the vast quantity of global systematic high-frequency microwave data that have been collected for the past 15 yr by the Special Sensor Microwave Imager (SSM/I).

Despite the fact that high-frequency microwave sensors will have limited retrieval capabilities, there are some conditions under which these observations can provide useful soil moisture information. Most studies using SSM/I and other passive microwave satellite systems to estimate soil moisture have utilized antecedent precipitation indices (APIs) as validation (Choudhury and Golus 1988; Ahmed 1995; Teng et al. 1993; Owe et al. 1992). Morland et al. (2001) compared APIs to soil moisture in estimating SSM/I emissivity. In that study they found APIs to be less correlated to emissivity and concluded that rapid drying of the soil layer, which determines the microwave emission was not adequately reflected in APIs.

A few investigations have employed limited observations from ground networks that were not optimally designed for this particular type of satellite data. The ground networks were either sparse, such as in Koike et al. (2000) (one measurement station per one SSM/I footprint) and in Vinnikov et al. (1999) (17 soil moisture stations for the entire state of Illinois), or the soil moisture layer observed was much deeper than that which determines the microwave response, such as in Owe et al. (1992) (20 cm) and in Vinnikov et al. (1999) (10 cm).

As part of the Southern Great Plains (SGP) hydrology experiments conducted in 1997 (SGP97) and 1999 (SGP99), ground observations of soil moisture were made over an extended region in order to contribute to the validation and demonstration of large-scale mapping of soil moisture using SSM/I data. In a previous investigation the use of a single-channel soil moisture retrieval algorithm was evaluated with limited datasets collected over the region in 1992 and 1994 (Jackson 1997). An investigation by Drusch et al. (2001) used the SGP97 SSM/I data and a more sophisticated radi-

TABLE 1. SSM/I satellite platforms.

Satellite	Dates of operation	Ascending equatorial crossing time (UTC)
F8	Jun 1987–Apr 1994	0612
F10	Dec 1990–Nov 1997	2215
F11	Nov 1991–May 2000	1925
F13	Mar 1995–present	1754
F14	Apr 1997–present	2046
F15	Dec 1999–present	2120
F16	2003 launch	TBD



ative transfer approach that fully considered atmospheric effects to study soil moisture and brightness temperature relationships.

These previous studies have indicated the limitations of both the high-frequency data and the models used for soil moisture retrieval. In the current investigation an alternative retrieval technique utilizing multipolarization observations and based upon the work of Njoku and Li (1999) was implemented and tested for the SGP region. Available information on parameters needed by the soil moisture retrieval algorithm at high frequencies is lacking. As part of the current investigation, a technique for extracting algorithm parameters from the observations was developed and tested. The algorithm was then used to produce soil moisture maps of the region for the two study periods.

## 2. The SSM/I instrument

The SSM/I is a conical scanning total power microwave radiometer system operating at a look angle of  $53^\circ$  at four frequencies: 19.4, 22.2, 37, and 85.5 GHz. The 22.2-GHz channel operates in V polarization and the other three channels in both V and H polarization. Spatial resolution [effective field of view (EFOV) 3-dB beamwidth] ranges from 69 km by 43 km at 19.4 GHz to 15 km by 13 km at 85.5 GHz. The orbital period is about 102 min, which results in 14.1 orbits per day. For a given satellite, coverage is possible twice a day approximately 12 h apart on the ascending and descending passes. Additional information can be found in Hollinger et al. (1990).

SSM/I instruments have been a component of the Defense Meteorological Satellite Program since 1987. Table 1 summarizes some aspects of the data records available from this series of satellites.

## 7. Conclusions

Previous studies have suggested that microwave data with frequencies higher than 10 GHz are not appropriate for soil moisture estimation since the vegetation will strongly mask surface information. However, a number of investigations using SSM/I data have presented evidence that there is a usable soil moisture signal under some conditions. Much of this work has been qualitative in nature, relying on indices and not the surface soil moisture for validation.

There are well-established theories describing the microwave emission of the land surface. Vegetation is important in these models but is less significant at low frequencies. At higher frequencies the vegetation is a more dominant feature, and soil moisture retrievals are more sensitive to the representation and parameterization of vegetation effects. Estimating algorithm parameters a priori, as suggested for low frequencies, may not be reliable. For this reason we evaluated a retrieval technique utilizing dual-polarization observations.

Data collected in two field experiments in the Southern

Great Plains of the United States were used with SSM/I measurements to better understand the behavior of soil moisture and emissivity at these higher frequencies. The region used for the investigation was well suited to the limitations of using 19-GHz data to estimate soil moisture.

For each of three study areas, a linear relationship was observed between soil moisture and emissivity. Areas with lighter vegetation and the use of H-polarization data produced better linear regression results based on correlation and standard error of estimate values.

An attempt was made to describe the observed linear trends using a radiative transfer model in which the vegetation parameters were optimized. This is essentially the same as using the single-polarization approach described in Jackson (1997). Analysis resulted in values of the vegetation optical depth and the single-scattering albedo that were reasonable based upon published data. The single-channel algorithms had higher SEE than the linear regressions but low bias. These results suggest that there is a limitation on accuracy that is attributed to either the model structure or the quality of the ground observations. Both causes are considered possible.

The dual-polarization algorithm explicitly incorporates parameters that were lumped in the single-channel optimization. It utilizes the same equations but makes assumptions about the effects of polarization on some parameters. If these assumptions on vegetation effects are valid, it is a potentially robust solution. The most significant problem in applying this approach is reducing the number of unknowns to two (i.e., soil moisture and the vegetation parameter  $b$ ).

The availability of data to perform atmospheric corrections and to estimate effective soil temperature at the time of SSM/I observation may add some restrictions to the application of this approach to areas without meteorological network and radiosonde observations. As an alternative to estimating temperature, van de Griend (2001) demonstrated that effective temperature could be estimated using 37-GHz V-polarization brightness temperature and some climatologic records over semiarid areas. The *Aqua* satellite, recently launched by NASA, includes sensors that can provide atmospheric profile information. With these additional measurements this approach can be extended to other areas with sparse vegetation.

An error analysis of the dual-polarization algorithm revealed that it produced good results for two of the test areas (CF and LW) but poor results at ER. This is attributed to the sources of error identified in previous investigations (Jackson et al. 2002).

Subject to the assumptions made in its implementation, the dual-polarization algorithm worked well in these tests with SSM/I data. We acknowledge that conditions in the SGP region are benign for the frequency used. However, it is anticipated that with lower-frequency channels available with AMSR that the assumptions and limitations imposed by vegetation on soil moisture estimation will be improved.

# Remote sensing of subpixel snow cover using 0.66 and 2.1 $\mu\text{m}$ channels

Yoram J. Kaufman,<sup>1</sup> Richard G. Kleidman,<sup>2</sup> Dorothy K. Hall,<sup>1</sup> J. Vanderlei Martins,<sup>3</sup> and Jonathan S. Barton<sup>4</sup>

Received 5 June 2001; revised 8 February 2002; accepted 17 February 2002; published 23 August 2002.

[1] Hydrologic models increasingly require knowledge of the amount of snow cover within a pixel in order to provide accurate estimates of snow covered area. Present methods for remote sensing of subpixel snow cover require knowledge of the spectral reflectance properties of the snow as well as the background material, making these methods difficult to apply globally. Similar problems were encountered in global remote sensing of aerosol particles over varying land terrain. Since both aerosol and snow are dark at 2.1  $\mu\text{m}$ , we suggest a method for sub-pixel snow mapping based on experience with remote sensing of aerosols. Here the pixel reflectance at 2.1  $\mu\text{m}$  is used to estimate the reflectance of the non-snow regions in the pixel at 0.66  $\mu\text{m}$ . The difference between the total pixel brightness at 0.66  $\mu\text{m}$  and the derived brightness of the same pixel without the snow is used to estimate the sub-pixel snow cover with an error usually  $< \pm 0.05$ . **INDEX TERMS:** 1610 Global Change: Atmosphere (0315, 0325); 1827 Hydrology: Glaciology (1863)

## 1. Introduction

[2] Remote sensing of subpixel snow cover is hindered by the unpredictable variability of the spectral properties of the subpixel non-snow surface cover. To overcome this difficulty, spectral mixing modeling techniques have been applied to the mapping of snow cover [Rosenthal, 1993; Nolin et al., 1993]. These techniques represent the mixed pixel spectral properties and composition by combining several classes of surface covers from the image classification. The resultant fraction of snow represents the fraction of snow subpixel cover. This technique is scene based and very difficult to implement on a large scale. Automated techniques to map the subpixel snow cover are reported by Rosenthal and Dozier [1996], but are still problematic for use at the global scale because they apply only to a single scene or a set of scenes. In that work, a decision-tree threshold analysis approach using several spectral channels is used. The numeric thresholds were derived from the same remote sensing data sets that are used for snow detection. Though very useful for regional applications, they are not optimal for global applications because of the need to employ spectral end-members that describe the scene parameters. These end-members are unique to a scene or set of scenes, and it is very difficult to derive end-members that are globally applicable due to the extreme variability in spectral reflectance of non-snow features.

[3] We suggest that a method that must be applied globally, on a routine basis, needs to rely on a much simpler algorithm, and properties globally.

[4] Since February 2000, the Moderate Resolution Imaging Spectroradiometer (MODIS) on the Terra satellite [Kaufman et al., 1998] has been acquiring data, globally at 0.25 to 1 km spatial resolution. MODIS data are used to produce operationally, binary snow maps [Hall et al., in press]. Subpixel snow cover is a necessary enhancement of this product. A computationally-frugal technique for subpixel snow cover detection is required for automated, global snow cover mapping.

[5] We find the problem of remote sensing of subpixel snow to be similar to remote sensing of aerosol [Kaufman et al., 1997a]. In both cases the optical properties of the background surface cover, as observed from space, are mixed with the subpixel snow or the aerosol above the surface, each with its own spectral properties. The method to separate the aerosol and surface contribution is

based on the fact that fine aerosol is transparent and non-reflective at the long solar wavelengths (e.g. 2.1  $\mu\text{m}$ ) and therefore its contribution at 2.1  $\mu\text{m}$  is negligible. Snow is also very dark in this wavelength, in particular if the snow is not fresh, with large grain sizes and therefore its contribution to the pixel reflectance is small. In the case of aerosol the reflectance of the surface under the aerosol at 0.66  $\mu\text{m}$  is estimated using an empirical relationship of surface reflectance in 0.66 and 2.1  $\mu\text{m}$  [Kaufman et al., 1997b; Karnieli et al., 2000]:

$$\rho_{0.66} = [0.5 \pm 0.05]\rho_{2.1} \quad (1)$$

This relationship provides a simple method to estimate the surface reflectance under the aerosol layer over the land. It eliminates the need to generate and update global maps of surface reflectance values. The aerosol optical thickness, a measure of the aerosol column concentration, is determined from the difference in the surface reflectance measured at the top of the atmosphere,  $\rho_{0.66}^a$  that includes the surface, molecular scattering and aerosol:

$$\Delta\rho_{0.66-2.1} = \rho_{0.66}^a - 0.5\rho_{2.1} = \text{aerosol optical thickness}$$

The technique was validated against ground based measurements around the world and resulted in accurate values of aerosol optical thickness over the land [1998; 2002]. A similar technique is developed here for the subpixel snow cover in the pixel from the difference  $\Delta\rho_{0.66-2.1}$ , thus avoiding the need for global maps of the surface reflectance.

## 2. Approach

[6] After applying an atmospheric correction to the Landsat data [e.g., Vermote et al., 1997] the corrected surface reflectance,  $\rho_{0.66}^c$ , is derived from the measured one,  $\rho_{0.66}^m$ . The basic approach to derive the snow fraction from the corrected reflectance is:

$$f_{\text{snow}} = (\rho_{0.66}^c - 0.5\rho_{2.1})/\rho_{0.66}^{\text{snow}} \quad (2)$$

where  $\rho_{2.1}$  is the pixel reflectance at 2.1  $\mu\text{m}$  and  $\rho_{0.66}^{\text{snow}}$  is the reflectance of the snow.

[7] The snow reflectance varies with the direction of observations and age of the snow. It may be determined as the average of the brightest 1–5% of the pixels in a given region with restricted view direction (e.g.  $\pm 20^\circ$ ), in the 250 m MODIS resolution. In the present study we found  $\rho_{0.66}^{\text{snow}} = 0.6$ , and estimate the error as  $\pm 0.2$ . Here we assume that the snow reflectance at 2.1  $\mu\text{m}$  is small and does not distort the relationship between the reflectance at 2.1  $\mu\text{m}$  and 0.66  $\mu\text{m}$  used for the background reflectance.

[8] The applicability of the empirical relationship (1) was originally suggested to hold for  $\rho_{2.1} < 0.15$ . But recently we found in regions with no standing water the relationship can be extended to brighter surfaces ( $\rho_{2.1} < 0.25$ ) [Kaufman et al., 2000; Karnieli et al., 2000]. This finding is also supported by recent modeling study [Kaufman et al., 2002]. Original application of equation 2 to a Landsat-5 Thematic Mapper (TM) scene used by Rosenthal and Dozier [1996], and comparison with their validated technique, showed non-linearity in the errors in the fractional snow retrieval. We associated this non-linearity to variability of the snow reflectance, due to variability in the snow thickness, and grain size as a function of the snow fraction and due to multiple scattering between the snow and vegetation or soil. This leads to an empirical correction of the snow fraction obtained from equation 3:

$$f_{\text{snow}}^c = f_{\text{snow}} \rho_{0.66}^{\text{snow}} / (\rho_{0.66}^{\text{snow}} - 0.09 + 0.07f_{\text{snow}}) \quad (3)$$



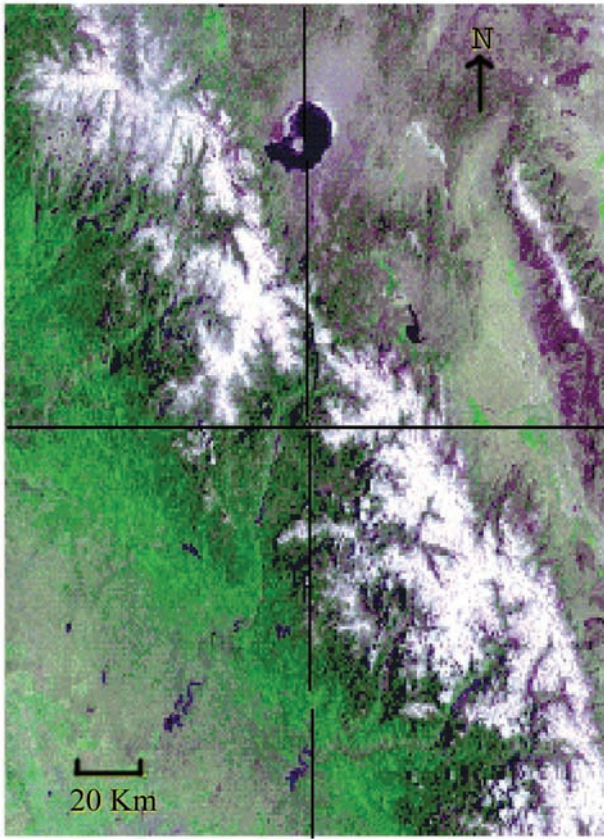


**Figure 1.** Color composite (red - 0.67  $\mu\text{m}$ , green - 0.87  $\mu\text{m}$  and blue - 0.49  $\mu\text{m}$ ) of the Landsat Thematic Mapper image acquired May 10, 1992. The image shows the southern Sierra Nevada range, including Mono Lake, California and the White Mountains to the east. Lines on the image show divisions into the four quadrants discussed in the analysis and in Figure 2. LL-lower left, UL-upper left, LR-lower right, UR-upper right.

### 3. Application

[9] The method is applied to the same Landsat 5 TM image used by *Rosenthal and Dozier* [1996]. The image, acquired May 10, 1992, shows the southern Sierra Nevada mountain range, including Mono Lake, California (Figure 1).

[10] To reduce the atmospheric effect on the snow retrieval, we applied a simple atmospheric correction to the 0.66  $\mu\text{m}$  channel, by estimating the atmospheric reflectance (for black surface) based on the top-of-atmosphere bidirectional reflectance (BRF) of the darkest water body in the image, in this case Mammoth Lake. The correction then follows *Fraser and Kaufman* [1985], assuming that for surface reflectance of 0.4 the atmospheric effect is zero. The reflectance of the water is assumed to be 0.005. The corrected reflectance at 0.66  $\mu\text{m}$ ,  $\rho_{0.66}^c$  is calculated from the top of the atmosphere BRF  $\rho_{0.66}^a$  by:

$$\rho_{0.66}^c = (\rho_{0.66}^a - \rho_{0.66}^{\text{atm}}) \rho_{0.66}^{\text{crit}} / (\rho_{0.66}^{\text{crit}} - \rho_{0.66}^{\text{atm}}) \quad (4)$$

where  $\rho_{0.66}^{\text{atm}}$  is the atmospheric path radiance due to aerosol and molecular scattering ( $\rho_{0.66}^{\text{atm}} = 0.03$ ) and  $\rho_{0.66}^{\text{crit}}$  is the critical surface reflectance (0.4), defined as the value of the surface reflectance for which additional aerosol does not change the apparent brightness observed from space. The subpixel snow fractions derived from equation 2 and from the correction in equation 3 are shown in Figure 2. To demonstrate the repeatability of the technique, we divided the Landsat scene into 4 equal quadrants and compared the snow fraction with the validated technique of *Rosenthal and Dozier* [1996], that is used here as the ground truth for each quadrant (called “measured snow cover”). The results show very

good agreement, mainly for the empirically corrected data. The detailed errors in the 4 quadrants are plotted as a function of the measured snow cover in Figure 3. The average absolute error is between  $\pm 1\%$  and  $2\%$  in the snow cover for the 4 quadrants. An image of the spatial distribution of the errors is seen in Figure 4. The positive and negative errors are clustered in regions with similar surface conditions that have a similar error according to the assumptions in equation 3.

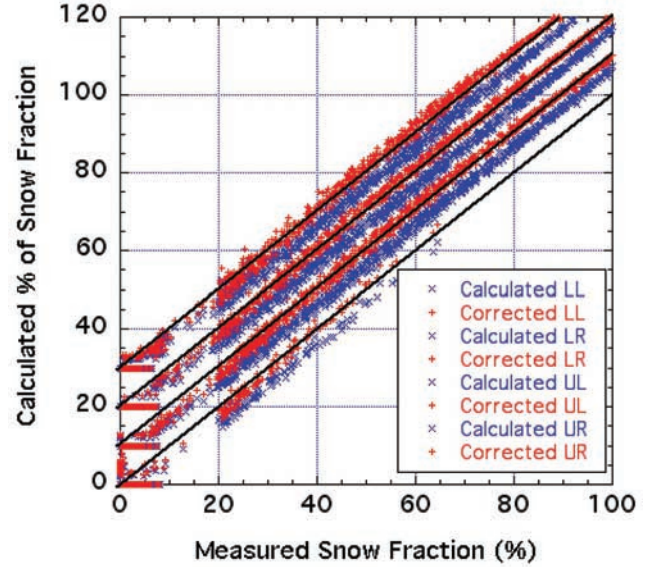


**Figure 2.** Scatter plot of the calculated snow cover (in %) from equation 2 (blue) and the empirically-corrected snow cover from equation 3 (red) as a function of the snow fraction derived by the validated technique of *Rosenthal and Dozier* [1996]. The results for the 4 quadrants were shifted by 10% on the abscissa, for better viewing of the scatter plots. Therefore all the black lines start in their corresponding zero point.

### 6. Conclusions

[13] A new technique to measure sub-pixel snow cover is presented. It is based on principles of remote sensing of aerosol over the land. Both aerosol and sub-pixel snow are dark at 2.1  $\mu\text{m}$  and much brighter at 0.66  $\mu\text{m}$ . A relationship between directional reflectance of the non-snow (vegetation and soils) part of the surface, at 0.66 and at 2.1  $\mu\text{m}$  is used to predict the reflectance at 0.66  $\mu\text{m}$  in the absence of snow. Then the excess reflectance at 0.66  $\mu\text{m}$  at the top of the atmosphere measured from the satellite sensor is attributed to snow. The successful application of this relationship to aerosol suggests that the same relationship between the non-snow surface reflectance between 2.1 and 0.66  $\mu\text{m}$  can also be used for snow. The method is expected to be most accurate for snow fractions smaller than 30%. Error analysis shows that this technique can measure snow fractions of 0.1 with an error of  $\pm 0.03$  while that of 0.3 with an error of  $\pm 0.1$ . Validation using the 4 quadrants of a single Landsat TM image reveal errors of 2–4%. The algorithm was shown to be independent of the spatial scale of the data, at least in the case being studied, and equally accurate for detecting sub-pixel snow in resolutions of 30 m and 500 m. Global validation is yet to be made, however an application to MODIS data collected in the same location of the Landsat data of Figure 1 is shown in Figure 6. MODIS is providing 500-m resolution snow-cover products on a daily basis using a binary snow-detection algorithm. The addition of a subpixel snow-cover algorithm is a planned enhancement, and several algorithms are being tested [*Barton et al.*, 2001]. In Figure 6 we show the subpixel fraction of snow derived from the MODIS data.

# Initial Testing of a Massively Parallel Ensemble Kalman Filter with the Poseidon Isopycnal Ocean General Circulation Model

CHRISTIAN L. KEPPENNE

*Science Applications International Corporation, Beltsville, Maryland*

MICHELE M. RIENECKER

*NASA Seasonal-to-Interannual Prediction Project, Laboratory for Hydrospheric Processes, Goddard Space Flight Center, Greenbelt, Maryland*

(Manuscript received 24 August 2001, in final form 5 March 2002)

## ABSTRACT

A multivariate ensemble Kalman filter (MvEnKF) implemented on a massively parallel computer architecture has been developed for the Poseidon ocean circulation model and tested with a Pacific basin model configuration. There are about 2 million prognostic state-vector variables. Parallelism for the data assimilation step is achieved by regionalization of the background-error covariances that are calculated from the phase-space distribution of the ensemble. Each processing element (PE) collects elements of a matrix measurement functional from nearby PEs. To avoid the introduction of spurious long-range covariances associated with finite ensemble sizes, the background-error covariances are given compact support by means of a Hadamard (element by element) product with a three-dimensional canonical correlation function.

The methodology and the MvEnKF implementation are discussed. To verify the proper functioning of the algorithms, results from an initial experiment with in situ temperature data are presented. Furthermore, it is shown that the regionalization of the background covariances has a negligible impact on the quality of the analyses.

Even though the parallel algorithm is very efficient for large numbers of observations, individual PE memory, rather than speed, dictates how large an ensemble can be used in practice on a platform with distributed memory.

## 1. Introduction

### *a. Background and motivation*

Many of the early advances in ocean data assimilation have emerged from practical applications in the tropical Pacific. These applications have been driven by the need to initialize the ocean state for coupled atmosphere-ocean forecasts of the El Niño–Southern Oscillation (ENSO) phenomenon. In addition, hindcast estimates of the ocean state have been useful in diagnosing the evolution of El Niño. Over much of the world's oceans, large-scale assimilation is facilitated by the availability of satellite altimetry because of the sparsity of in situ data. However, in the tropical Pacific, the ocean observing system was vastly improved by the deployment of the Tropical Atmosphere Ocean (TAO) array of moored buoys (e.g., McPhaden et al. 1998) to support seasonal-to-interannual (SI) climate studies and prediction. One of the major successes of the Tropical Ocean Global Atmosphere program was the emergence of coupled physical models (as opposed to statistical models) with some prediction skill (e.g., Chen et al. 1995; Ji et al. 1996).

Recently, the NASA Seasonal-to-Interannual Prediction Project (NSIPP) has been established to further the utilization of satellite observations for prediction of short-term climate phenomena. NSIPP undertakes routine experimental forecasts in a research framework with global coupled ocean–atmosphere–land surface models. The initial implementation has used an ocean analysis system employing a simple assimilation methodology—

a univariate optimal interpolation (UOI)—with the Poseidon isopycnal ocean general circulation model (OGCM; Schopf and Loughe 1995; Konchady et al. 1998; Yang et al. 1999). Like several other ocean data assimilation systems currently in use at other institutions (e.g., Ji and Leetma 1997), it is based on the assumption that the forecast-error covariances are approximately Gaussian and that the covariances between the temperature-field errors and the salinity-field and current-field errors are negligible.

Largely due to the high-resolution coverage and accuracy of the TAO measurements, the UOI is effective in improving surface and subsurface temperature-field estimates in the equatorial region in comparison with the estimates obtained without temperature assimilation. As a result, its introduction into the NSIPP coupled forecasting system has resulted in significant improvements in the coupled model's hindcast skill of Niño-3 temperature anomalies.

The UOI has the advantage of being inexpensive in terms of computing resources. Nevertheless, it suffers from three major shortcomings: first, it can only be used to assimilate measurements of a model prognostic variable; second, it does not use any statistical information about the expected inhomogeneous distribution of model errors; third, it is based on a steady-state error-covariance model, which gives the same weight to a unit innovation regardless of how accurate the ocean-state estimate has become as a result of previous analyses. Directly linked to this shortcoming is the failure to provide time-dependent estimates of the model errors.



In response to the first two shortcomings, a parallel multivariate OI (MvOI) system has been implemented. The MvOI uses steady-state estimates of the model-error statistics computed from ensemble runs of the OGCM in the presence of stochastic atmospheric forcing from an ensemble integration of the atmospheric general circulation model (AGCM) (Borovikov and Rienecker 2002). Yet, the MvOI cannot adjust to dynamically evolving error statistics. A parallel multivariate ensemble Kalman filter (MvEnKF) has been developed to address this shortcoming. This paper discusses its design, implementation, and initial testing.

#### *b. Overview of the ensemble Kalman filter*

Although the Kalman filter (Kalman 1960) and its generalization to nonlinear systems, the extended Kalman filter, are statistically optimal sequential estimation procedures that minimize error variance (e.g., Daley 1991; Ghil and Malanotte-Rizzoli 1991; Bennett 1992), they cannot be used in the context of a high-resolution ocean or atmospheric model because of the prohibitive cost of time stepping the model-error covariance matrix when the model has more than a few thousand state variables. Therefore, reduced-rank (e.g., Cane et al. 1996; Verlaan and Heemink 1997) and asymptotic (e.g., Fukumori and Malanotte-Rizzoli 1995) Kalman filters have been proposed. Evensen (1994) introduced the ensemble Kalman filter (EnKF) as an alternative to the traditional Kalman filter. In the EnKF, an ensemble of model trajectories is integrated and the statistics of the ensemble are used to estimate the model errors. Closely related to the EnKF are the singular evolutive extended Kalman filter (Pham et al. 1998) and the error-subspace statistical estimation algorithms described in Lermusiaux and Robinson (1999).

Evensen (1994) compared the EnKF to the extended Kalman filter in twin assimilation experiments involving a two-layer quasigeostrophic (QG) ocean model on a square  $17 \times 17$  grid. Evensen and van Leeuwen (1996) used the EnKF to process U.S. Navy Geodesy Satellite (Geosat) altimeter data into a two-layer, regional QG model of the Agulhas current on a  $51 \times 65$  grid. Houtekamer and Mitchell (1998) and Mitchell and Houtekamer (2000) used the EnKF in identical twin experiments involving a three-level, spectral QG model at triangular truncation T21 and parameterized model errors.

Keppenne (2000, hereafter K00) conducted twin experiments with a parallel MvEnKF algorithm implemented for a two-layer, spectral, T100 primitive equation model with parameterized model errors. With about  $2 \times 10^5$  model variables, the state-vector size was small enough in this application to justify a parallelization scheme in which each ensemble member resides in the memory of a separate CRAY T3E processor [hereafter, processing element (PE)]. To parallelize the analysis, K00's algorithm transposes the ensemble across PEs at analysis time, so that each PE ends up processing data from a subregion of the model domain. The influence of each observation is weighted according to the dis-

tance between that observation and the center of each PE region.

To filter out noise associated with small ensemble sizes, Houtekamer and Mitchell (2001) developed a parallel EnKF analysis algorithm that applies a Hadamard (element by element) product (e.g., Horn and Johnson 1991) of a correlation function having local compact support with the background-error covariances. They tested this analysis scheme on a  $128 \times 64$  Gaussian grid corresponding to a 50-level QG model using randomly generated ensembles of first-guess fields. The benefits of constraining the covariances between ensemble members using a Hadamard product with a locally supported correlation function has also been investigated by Hamill and Snyder (2000) in the context of an intermediate QG atmospheric model.

### 5. Summary

This article describes the MvEnKF design and its parallel implementation for the Poseidon OGCM. A domain decomposition whereby the memory of each PE contains the portion of every ensemble member's state vector that corresponds to the PE's position on a 2D horizontal lattice is used. The assimilation is parallelized through a localization of the forecast-error covariance matrix. When data becomes available to assimilate, each PE collects from neighboring PEs the innovations and measurement-functional elements according to the localization strategy. The covariance functions are given compact support by means of a Hadamard product of the background-error covariance matrix with an idealized locally supported correlation function. In EnKF implementations involving low-resolution models, one has the freedom to work with ensemble sizes on the order of hundreds or thousands. Rather, with the state-vector size of approximately 2 million variables considered here, memory, communications between PEs, and operation count limit the ensemble size. In most instances, 40 ensemble members distributed over 256 CRAY T3E PEs are used.

Besides the details of the observing system implementation, the impact of the background-covariance localization on the analysis increments is discussed, as well as performance issues. To confirm that the data assimilation system is working properly, the discussion also includes results from an initial test run in which the MvEnKF is used to assimilate TAO temperature data into Poseidon.

Some issues that must be addressed to improve the MvEnKF are the deficiency of the system-noise model, which only accounts for forcing errors, the problem of ensemble initialization, which can be addressed using a perturbation-breeding approach, and the memory limitations inherent with running the MvEnKF on a MPP with distributed memory. On a machine with globally addressable memory, the memory-imposed constraints would be less severe. Fortunately, the modular, object-oriented approach used to develop the MvEnKF allows an easy port of the implementation from the CRAY T3E to almost every distributed-memory or shared-memory parallel computing architecture.

# Evidence and quantification of the correlation between radar backscatter and ocean colour supported by simultaneously acquired in situ sea truth

I-I Lin, Liang-Saw Wen, and Kon-Ke Liu

National Center for Ocean Research, Taipei, Taiwan

Wu-Ting Tsai

National Chiao-Tung University, Taiwan

Antony K. Liu

NASA Goddard Space Flight Center, USA

Received 5 September 2001; accepted 1 April 2002; published 28 May 2002.

[1] Near simultaneously (within 2 hours) acquired ERS-2 Synthetic Aperture Radar (SAR) and Sea-viewing Wide Field-of-view Scanner (SeaWiFS) data over an upwelling region shows remarkable similarity in feature's location, scale, and boundary. Under uniform wind and sea states, reduction of Normalised Radar Cross Section (NRCS) from SAR is found highly correlated with the increase of SeaWiFS Chlorophyll-a (Chl-a) concentration. Typically, 1 mg/m<sup>3</sup> of chlorophyll-a is correspondent with a 5 dB reduction of NRCS. This relationship is supported by simultaneously collected in situ sea truth measurements. This work provides a direct evidence and exceptional quantification of the relationship between radar backscatter and ocean colour that has long been speculated. **INDEX TERMS:** 4275 Oceanography: General: Remote sensing and electromagnetic processes (0689); 4279 Oceanography: General: Upwelling and convergences; 4219 Oceanography: General: Continental shelf processes; 4504 Oceanography: Physical: Air/sea interactions (0312)

## 1. Introduction

[2] The correlation between Synthetic Aperture Radar (SAR) backscatter and ocean colour is a long being speculated issue [Nilsson and Tildesley, 1995; Clemente-Colón and Yan, 1999; Gower and Vachon, 2001]. Nilsson and Tildesley [1995] found possible cases in using SAR to discriminate different oceanic water masses and they attributed to the cause being that different water masses carrying different surfactants which results in difference in backscatter.

[3] It is well reported that natural films or surfactants can effectively dampen ocean surface roughness causing attenuation of radar backscatter. Under suitable wind condition, these films can be detected in Synthetic Aperture Radar (SAR) imagery [Alpers and Hühnerfuss, 1989; Espedal et al., 1996]. Surfactants are mainly originated from ocean biological activities [Zutic et al., 1981]. Nilsson and Tildesley [1995] thus suggested that, under appropriate condition, SAR may be able to discriminate water masses that have different biological activities via difference in the associated surfactants. They further suggested that it may be possible to discriminate different scales, types, and intensity of ocean biological activities by Normalised Radar Cross Section (NRCS). That is, SAR may carry ocean colour information and there is a potential to retrieve ocean colour

information from SAR NRCS. Similar example in using SAR to discriminate different water masses was also found by Hsu et al. [1997a, 1997b].

[4] However, there are very few co-located/near or co-incident pair of SAR and ocean colour images to confirm the above hypothesis. Clearly the major reason is the lack of operational overlap between SAR (1991 onwards) and ocean colour sensors till the launch of ADEOS-I ocean colour sensor (OCTS) in 1996 and SeaWiFS Sensor in 1997. Liu et al. [2000] is one of the rare published evidence of such correlation. They found strong correlation and the matching of boundary between ERS-2 SAR and SeaWiFS data of coccolithophore bloom in the East Bering Sea during the fall of 1997. However, in Liu et al. [2000], no quantification nor in situ data to support the correlation between SAR NRCS and SeaWiFS Chlorophyll-a (Chl-a) was provided.

[5] This study attempts to provide another pair of evidence between ERS-2 SAR NRCS and SeaWiFS Chl-a. In addition, correlation of the 2 parameters are quantified and supported by simultaneously acquired in situ sea truth data.

## 2. Methodology

[6] In order to confirm the above hypothesis, near simultaneously (within 2 hours) acquisition of ERS-2 SAR image and SeaWiFS image was made on 19 August 2000 over our study site, the upwelling region off Northeastern Taiwan. This upwelling system is formed by upwelling of the subsurface Kuroshio water when Kuroshio encounters the continental shelf break of the East China Sea [Liu et al., 1992] and the system is known to be of active biological activities [Gong et al., 1997]. Previous study has also confirmed the presence of surfactants associated with this system [Hsu et al., 1997a, 1997b]. In order to assess the changes of NRCS due to other potential co-existing processes, sea surface temperature (SST) from the Advanced Very High-Resolution Radiometer (AVHRR), and surface synoptic weather charts and digital weather data from the nearest weather station, Penchiayu (122.07°E, 25.63°N) were also collected at nearest available acquisition time (within 6 hours) for joint analysis. Sea truth data were collected by Taiwan's Research Vessel R/V Ocean Researcher 2 (OR-2) simultaneously during the satellite data acquisition. Sea truth parameters includes temperature, salinity, and chlorophyll-a concentration. Temperature and salinity data were collected using a Seabird CTD device. Chlorophyll-a samples were collected using ultra-clean sampling protocols [Wen et al., 1999] and analysed using fluorescence and spectrophotometric methods [Grasshoff et al., 1983]. Cruise track during the in situ campaign was coordinated

according to the SAR image (Figure 1). ERS-2 SAR passed the study area at 02:28 UTC 19 August 2000, and this SAR image was processed in near real-time (within 6 hours) at Taiwan's Ground Receiving Station. The locations of upwelling features were identified and this information was transmitted to OR-2 which was standing-by in neighboring waters by 08:00 UTC for collecting immediate sea truth.

### 3. Correlation of SAR NRCS and SeaWiFS Chl-a

[7] In Figure 1 a dark feature in the ocean extends northeastward from the northern tip of Taiwan, where upwelling is known to occur [Liu et al., 1992]. Figure 2 illustrates a subscene of the ERS-2 SAR image. In order to compare with the SeaWiFS image (04:37 UTC 19 August 2000), the SAR image was look-averaged from the original 12.5m to 1130m spatial resolution. Prior to look-averaging, antenna pattern correction and  $8 \times 8$  Lee filter (for speckle removal) were applied. This SAR image is displayed in NRCS which was calculated as  $NRCS = 20 \times \log DN - K$ , where  $DN$  is the pixel Digital Number and the  $K$  value is 57.3, given by the ERS-2 SAR Ground Receiving Station at the Center for Space and Remote Sensing Research, National Central University, Taiwan. The NRCS was color-coded for easy distinction and reference.

[8] The dark feature shown in Figure 1 is depicted as the coloured region in Figure 2, which is characterized by various degree of lower NRCS ( $-10.0$  to  $-25.1$  dB) in contrast with the uniformly higher NRCS ( $-7.0$  to  $-10.0$  dB) in the white region. In the co-located SeaWiFS image (Figure 3), there exists a similarly southwest to northeast trending feature, which is characterised by higher Chl-a concentration ( $0.7$  to  $2.0$  mg/m<sup>3</sup>) in contrast to the ambient Chl-a concentration below  $0.7$  mg/m<sup>3</sup>. The features (low NRCS in SAR and high Chl-a in SeaWiFS) found in both images have an almost exact match in their location, scale, and boundary (solid and dashed curves in Figure 3).

[9] To quantify the relationship between NRCS and Chl-a, data from 4 transects in both images are extracted (Figures 2 and 3). Figure 4 illustrates the relationship in one exemplary transect (transect C). The elevated concentration of Chl-a is apparently attributable to the Kuroshio upwelling [Gong et al., 1997]. A clear negative correlation is found between SAR NRCS and Chl-a. It is tantalizing to conclude that the reduction of NRCS within the feature is attributed to the surfactant produced during the active phytoplankton growth, but the reduction may also be caused by other environmental factors, such as wind field or sea surface temperature. To accurately quantifying the NRCS/Chl-a relationship, effects on co-existing factors such as changes in SST and wind must be eliminated [Clemente-Colón and Yan, 1999].

### 4. Wind and SST Effects on NRCS

[10] The effect of the ambient wind field is assessed using the surface synoptic weather charts and digital wind vector time series data of the Penchiayu weather station (data source: Central Weather Bureau, Taiwan) during the study period. It was found that throughout the SAR and SeaWiFS data acquisition period, the wind field has been stable and is dominant by a uniformly weak ( $\leq 5$  m/s) southwesterly wind, typical of the southwestern monsoon condition of the study area during summer. Thus the effect of changes in NRCS due to wind is insignificant and can be ignored.

[11] The theory that changes in SST produces changes in NRCS (via changes in air-sea boundary layer stability) is well established [Friehe et al., 1991; Zheng et al., 1997]. However, in the presence of surfactant, the effect of SST becomes secondary [Clemente-Colón and Yan, 1999]. To assess and quantify the effect of SST on NRCS, two AVHRR SST images are collected at nearest acquisition time (one at 21:00 UTC 18 August 2000, 5 hours before and one at 08:13 UTC 19 August 2000, 5 hours after) from SAR image acquisition. Figure 5 illustrates the co-located AVHRR SST subscene acquired at 08:13 UTC, around 5 hours after the SAR acquisition. It can be seen that the upwelled cold water pockets

are located along the northeastern coast of Taiwan. The corresponding SST is between  $27.4^{\circ}\text{C}$  and  $27.9^{\circ}\text{C}$  in contrast to the ambient warm water in the range of  $28.4^{\circ}\text{C}$  to  $30.0^{\circ}\text{C}$ . The SST image (not shown in this letter) collected before the SAR image acquisition shows similar patterns suggesting that the air-sea system has been stable between these two SST images consistent with the synoptic weather charts (not shown). Thus, Figure 5 is representative of the SST condition during SAR image acquisition. In Figure 5, it can also be seen clearly that the boundary of the cold SST waters deviates greatly from the SAR and SeaWiFS boundaries thus affirming that upwelling features observed in the SAR image (Figure 2) is not dominant by SST effects.

### 5. Quantification of NRCS and Chl-a Relationship

[12] Though SST is not the primary contributor to NRCS, to accurately quantify the relationship between Chl-a and NRCS, the effect of SST on NRCS is removed before quantification of the NRCS/Chl-a relationship. In recent studies of Clemente-Colón and Yan [1999, 2001] over upwelling regions, a  $0.66\text{dB}/^{\circ}\text{C}$  NRCS to SST relationship is obtained for ERS-2 SAR. In this study, this relationship is adopted since the same SAR system, the ERS-2 SAR is used. NRCS attenuation is defined as the local NRCS relative to the average ambient NRCS,  $\approx -7.7\text{dB}$ , outside the upwelling feature. After correction of the effect of SST, NRCS attenuation is plotted against SeaWiFS Chl-a concentration from data along the 4 transects. The number of the total original data pairs from the 4 transects is 1829. As mentioned, to match the spatial resolution of SeaWiFS image, the SAR image was look-averaged. After look-averaging, the data points were then binned into  $0.1$  mg/m<sup>3</sup> chl-a interval and is shown in Figure 6. It can be seen from Figure 6 that higher Chl-a concentration corresponds to higher attenuation of NRCS. In average,  $1$  mg/m<sup>3</sup> Chl-a corresponds to  $5$  dB attenuation of NRCS. The correlation coefficient is around  $0.62$ . A preliminary linear empirical relationship between ERS-2 SAR NRCS attenuation and Chl-a concentration is derived as  $NRCS = 4.64 \times \text{Chl}_a + 1.46$ . The simultaneously acquired in situ Chl-a measurements (3 coloured points) are also depicted. It can be seen that the derived NRCS versus Chl-a relationship is consistent with the sea truth data in a limited range of parameters.

### 6. Conclusion

[13] Results from the multi-sensor analysis found that SAR image is characterized by low NRCS (Normalized Radar Cross Section) in the upwelling region off Northeastern Taiwan. In comparison with the ambient waters, the attenuated NRCS is between  $0$  to  $14$  dB. In the SeaWiFS image acquired two hours later, the upwelling region is characterized by high Chl-a concentration in the range between  $0.7$  to  $2.0$  mg/m<sup>3</sup> whereas the ambient Chl-a concentration is below  $0.7$  mg/m<sup>3</sup>. It is also found that the upwelling features (low NRCS in SAR and high Chl-a in SeaWiFS) found in both images have an almost perfect match in their locations, scales, and boundaries. Furthermore, it is found that the attenuation of the NRCS is correlated with the increase of Chl-a concentration. Potential misinterpretation due to wind effect is eliminated by comparing with near-simultaneously acquired synoptic weather charts and digital wind vector data. Since changes of SST also affect NRCS, the contribution of SST to NRCS is removed by using the co-located and near-time AVHRR/SST data in an empirical model. The corrected NRCS is then used to derive a preliminary linear empirical relationship with Chl-a concentration. In addition, this relationship is consistent with simultaneously acquired in situ sea truth data. This finding provides a direct evidence of the relationship between SAR NRCS and Chl-a which also confirms and quantifies previous investigations [Nilsson and Tildesley, 1995; Liu et al., 2000]. It also supports the hypothesis of the association between the presence of ocean surface slicks and biological activity for global air-sea flux exchange estimation [Asher, 1997; Tsai and Liu, in press].

# **Ocean Surface Layer Drift Revealed by Satellite Data**

By Antony K. Liu, Yunhe Zhao, Wayne E. Esaias,

Oceans and Ice Branch, NASA Goddard Space Flight Center, Greenbelt, MD

Janet W. Campbell and Timothy S. Moore

Ocean Process Analysis Laboratory, Institute for the Study of Earth, Oceans, and Space

University of New Hampshire, Durham, NH

Historically, from low earth orbits, ocean surface feature tracking analyses have been based on data from a single orbital sensor collected over the revisit interval of a single satellite. In this paper, we report the first time that ocean surface layer currents have been derived by performing feature tracking using data from different sensors on different satellites. Satellite ocean color data provide important insight into the marine biosphere by quantifying certain fundamental properties (e.g. phytoplankton pigment concentration, marine primary production) on a global scale. In addition, satellite ocean color data can also be used as a tracer for measuring ocean surface layer currents, because the ocean color signal comprises information from a deeper water depth (10 to 30 meters) than surface signatures (such as sea surface temperature).

At present, there are two major global ocean color sensors in orbit. The Sea-viewing Wide Field-of-View Scanner (SeaWiFS) was launched onboard the Orbview-2 satellite in August 1997 [McClain et al., 1998], and the Moderate Resolution Imaging Spectroradiometer (MODIS) was launched onboard the Terra (EOS AM-1) satellite on December 18, 1999. Both satellites are in polar orbits at 705 kilometer altitudes, and each sensor views greater than 90% of the Earth's surface in 1-2 days. SeaWiFS acquires data in 8 visible and near-infrared bands, and MODIS acquires data in 36 spectral bands (UV-VIS-IR). Several of the MODIS visual

wavelength bands are analogous to the SeaWiFS ocean color bands. These data will provide important new information on the interactions between earth's major climate components and improve our understanding of global physical and biological processes on the land, in the oceans, and in the lower atmosphere [Esaias et al., 1998].

On a daily basis, the global observations of MODIS and SeaWiFS overlap to a large degree, with MODIS currently preceding SeaWiFS by about 70 minutes. The availability of multiple ocean color sensors in orbit allows the production of new data products. One such product, surface layer drift, can be derived when two satellite tracks overlap within a short time (for example, a few hours) without cloud coverage.

In this note, we demonstrate how chlorophyll *a* concentration images provided by MODIS and SeaWiFS can be used to derive surface layer drift. Data from MODIS and SeaWiFS (Figure 1) were collected on May 8, 2000 at 15:45 and 16:52 GMT, respectively, off the east coast of the United States. Major oceanographic features, such as the Gulf Stream boundary and a large cold-core eddy south of the Gulf Stream, can be clearly identified. To validate the results, data from several drifter buoys are compared with the satellite-derived flow field. The qualitative comparison shows a generally consistent pattern.

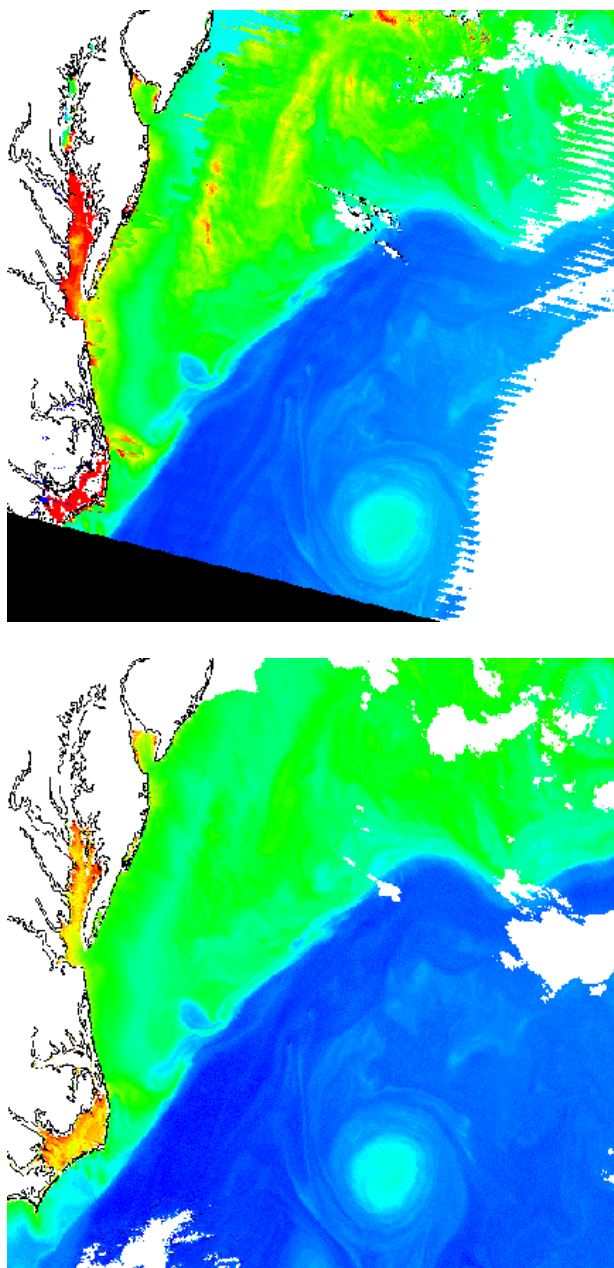


Fig. 1. Chlorophyll-*a* concentration data collected over US east coast from (a) MODIS, and (b) SeaWiFS on May 8, 2000 separated by 67 minutes.

### Comparison of MODIS and SeaWiFS Data

Currently, the comparison between SeaWiFS and MODIS is made with no correction for advection-induced change of chlorophyll values at different times, and is simply a pixel-pixel comparison. Advection between ocean color feature locations will add to the root-mean-square (RMS) errors, especially in high gradient regions. The satellite-derived current field can be used to assess the impact of changing chlorophyll values. Using the derived initial and end pixel numbers of the tracked features or the drift vector, the chlorophyll values at the original and end locations can be compared.

Figure 3 shows the comparison of chlorophyll *a* concentration data from MODIS and SeaWiFS (a) at the same locations, and (b) at the advected locations using the center pixel of a 17 x 17 km box surrounding the vector location. The RMS difference in chlorophyll concentration between these versions of MODIS and SeaWiFS chlorophyll products are 1.0124 mg/m<sup>3</sup> (or 0.1415 in log value) and 0.9701 mg/m<sup>3</sup> (or 0.1358 in log value) at the same locations and at the advected locations, respectively. The linear fit is somewhat improved after including the effects of advection. A reduction of 4 % in RMS error is attributed to correction for surface layer drift which can be derived from satellites. If a simple regression is used to eliminate the bias, the reduction of RMS difference is increased to 6.3%. Most of the points of improvement are at the locations where SeaWiFS predicts higher chlorophyll than the preliminary MODIS algorithm used here. This implies that the low chlorophyll concentration areas near the Gulf Stream were moved into the relatively high concentration locations. Although the improvement is small, it is in the expected direction, and the comparison demonstrates the general first-order accuracy of the drift field derived from satellite data. This comparison also indicates that surface layer drift is generally tangential to chlorophyll concentration gradient, allowing a steady gradient to be maintained. Once advection effects are well constrained, additional nonlinear effects such as biological growth/decay and diffusion processes can be targeted for further investigations.



# The potential of using Landsat 7 ETM+ for the classification of sea-ice surface conditions during summer

THORSTEN MARKUS,<sup>1,2</sup> DONALD J. CAVALIERI,<sup>1</sup> ALVARO IVANOFF<sup>3</sup>

<sup>1</sup>NASA Goddard Space Flight Center, Code 971, Greenbelt, MD 20771, U.S.A.

<sup>2</sup>Joint Center for Earth Systems Technology, University of Maryland, Baltimore County, Baltimore, MD 21250, U.S.A.

<sup>3</sup>Science System and Applications Inc., Lanham, MD 20706, U.S.A.

**ABSTRACT.** During spring and summer, the surface of the Arctic sea-ice cover undergoes rapid changes that greatly affect the surface albedo and significantly impact the further decay of the sea ice. These changes are primarily the development of a wet snow cover and the development of melt ponds. As melt ponds generally do not exceed a couple of meters in diameter, the spatial resolutions of sensors like the Advanced Very High Resolution Radiometer and Moderate Resolution Imaging Spectroradiometer are too coarse for their identification. Landsat 7, on the other hand, has a spatial resolution of 30 m (15 m for the panchromatic band) and thus offers the best chance to map the distribution of melt ponds from space. The different wavelengths (bands) from blue to near-infrared offer the potential to distinguish among different surface conditions. Landsat 7 data for the Baffin Bay region for June 2000 have been analyzed. The analysis shows that different surface conditions, such as wet snow and melt-ponded areas, have different signatures in the individual Landsat bands. Consistent with in situ albedo measurements, melt ponds show up as blueish, whereas dry and wet ice have a white to gray appearance in the Landsat true-color image. These spectral differences enable areas with high fractions of melt ponds to be distinguished.

## INTRODUCTION

Melt ponds and wet snow cover a significant area of the summer Arctic sea ice. Melt features on sea ice can cover more than 50% of the sea-ice area (Derksen and others, 1997; Fetterer and Untersteiner, 1998). As the albedo of wet snow and melt ponds is considerably lower than the albedo of dry ice (down to 0.2 for 30 cm deep ponds (Grenfell and Maykut, 1977)), accurate classification is essential for estimates of the polar summertime energy balance.

Perovich and others (1986) measured the spectral albedos of dry snow, wet snow and melt ponds for several depths. Whereas wet snow reduces the spectral albedo, compared to dry snow, by about the same value over the whole visible range, melt ponds have a greater reduction at longer wavelengths and therefore appear blueish. The spectral albedo of melt ponds for wavelengths greater than 800 nm is about 0.05 independent of melt-pond depth, whereas at 500 nm the albedo decreases from 0.6 for an early-season 0.1 m deep melt pond to 0.25 for a 0.3 m deep old melt pond. Nevertheless, melt ponds can have a range of color tones depending on the underlying ice type and ice thickness. The relative higher blue albedos have also been observed by Morassutti and LeDrew (1996) and Barber and Yackel (1999). Tschudi and others (1997) made use of this spectral difference to identify melt ponds using video data.

For large spatial areas, the Landsat 7 Enhanced Thematic Mapper Plus (ETM+) is an excellent sensor with which to study the surface properties of sea ice during summer. In addition to the different spectral bands, covering the range

from 450 nm (blue) to near-infrared and also thermal infrared, the data have a spatial resolution of 30 m (15 m for the panchromatic band) (Table 1). This high spatial resolution is necessary to enable the identification of melt ponds, as these commonly have diameters of a couple of meters, although melt ponds as large as 400 m across have been measured (Fetterer and Untersteiner, 1998). On first-year ice, melt ponds are generally larger in extent and shallower compared to multi-year sea ice. Therefore, areas of first-year ice only are an excellent test site for investigating melt-pond signatures in the Landsat data.

As part of the pre-launch summer Arctic Earth Observing System (EOS) Aqua Advanced Microwave Scanning Radiometer validation aircraft campaign Meltpond 2000 in June/July 2000 (Cavalieri, 2000), four cloud-free Landsat 7

Table 1. Landsat characteristics

Band No.	Bandwidth	Field of view	Sample distance
	nm	m	m
1	450–515	30	30
2	525–605	30	30
3	630–690	30	30
4	750–900	30	30
5	1550–1750	30	30
6	10400–12500	30	60
7	2090–2350	30	30
8	520–900	13 × 15	15

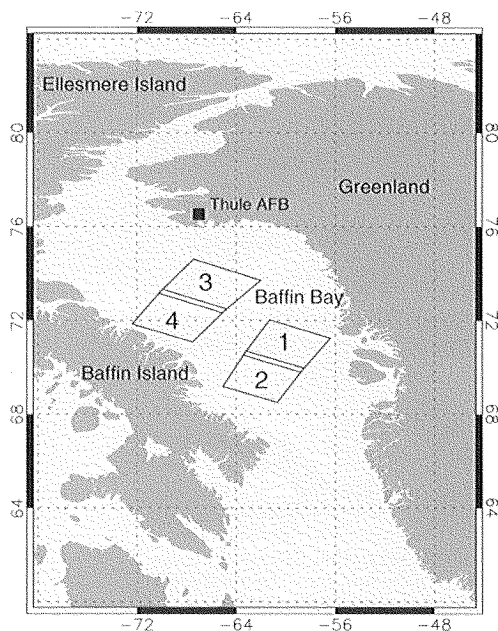


Fig. 1. Overview of the Landsat scenes acquired for 26–27 June 2000 (see Table 2 for details).

scenes over Baffin Bay were acquired (Fig. 1; Table 2). Baffin Bay is a good area for this initial investigation as it does not contain any multi-year ice so that we only have one primary ice type and the observed signatures result from variations in the surface properties only.

## ANALYSIS

After the digital numbers of each Landsat band have been scaled into absolute radiances for each wavelength ( $R_\lambda$ ), respective reflectivities ( $\alpha_\lambda$ ) are calculated following

$$\alpha_\lambda = \frac{\pi R_\lambda}{S_\lambda \cos \theta}, \quad (1)$$

where  $S_\lambda$  is the respective solar irradiance given in the Landsat 7 Science Data User Handbook and  $\theta$  is the solar zenith angle.

## Spectral analysis of melt features

Figure 2a shows a true-color subset of Landsat scene 2 (Table 2) of Baffin Bay where bands 3, 2, 1 are red, green and blue, respectively. The width of the image is 25 km. One can clearly distinguish between open water and individual ice floes. Whereas open water has a very distinct signature, the summertime reflectivities of sea ice vary significantly. Dry snow is generally seen as white, but with the onset of melt and the consequent wetting of the snow/ice cover, various tones of blue and gray are apparent. Only ridges and hummocks, despite some likely wetness, still appear as white. As mentioned above, melt ponds (at least shallow melt ponds) appear as light blue in the true-color images (point A). Additionally, one can identify different shades of blue (points B–D) that are separate from different shades of gray (points E–H). This is even more distinct in the two-dimensional histograms of band 1 vs band 4 and band 1 vs band 3 (Fig. 3). The majority of pixels fall along the ice–water line from point E

Table 2. Details of the Landsat scenes shown in Figure 1

Scene	Date	Time (GMT)	Sun elevation angle
1	26 June 2000	15:41:21	42.33°
2	26 June 2000	15:41:45	43.54°
3	27 June 2000	16:23:48	39.83°
4	27 June 2000	16:24:12	41.07°

(white ice) to point H (open water). Points F and G, which also lie on this line, represent very wet snow or remains of decaying sea ice. The heavy population of pixels with reflectivities of 0.68 in band 1 results from saturation in the high-gain Landsat data. The saturation limits the reflectivities so that expected maximum reflectivities of about 0.9 are not measured. If one continued the H–G–F line until the reflectivity in band 3 was about 0.65, reflectivities of band 1 would reach values of about 0.9. According to Perovich and others (1986), a wet snow cover shifts the albedo by about the same value for the whole visible range. Therefore points F and G lie on the ice–water line. On the other hand, when melt ponds develop, shorter wavelengths remain relatively high compared to the longer wavelengths. Thus, pixels will deviate from the dry-ice–open-water line towards higher band 1 (blue) values, and presumably move from point A to point D as the melt-pond depth increases.

It is noteworthy that points A–D (and similar pixels) lie on the outer margin of the distribution. These pixels have been identified because of their distinct blue signature. We assume that as melt ponds develop and increase in depth, pixels move from point E to A and then to points B, C and D. Pixels between the A–D curve and the E–H line are likely pixels that contain mixtures of melt ponds and ice with different degrees of wetness.

## CONCLUSIONS

This study has demonstrated the potential inherent in Landsat 7 ETM+ data for the classification of summertime sea-ice surface conditions. The Baffin Bay area is an ideal region for investigating melt ponds because all the sea ice is first-year ice and melt ponds tend to be shallower and larger in extent compared to multi-year ice. Areas with a high fraction of melt ponds can easily be distinguished from white and wet ice by their bluish appearance and by their greater negative spectral gradients between bands 2 and 3. Although areas with vast amounts of melt ponds are identifiable in the Landsat images, individual melt ponds may be too small to be detected. The distance of a given pixel in band 3 or 4 from the ice–water line (see Fig. 3) may help to estimate the fraction of melt ponds, but higher-resolution data are needed. As part of the Meltpond 2000 experiment, video data have been obtained which are currently being analyzed. We anticipate that these data will help to quantitatively access the accuracy of the algorithm and to address the problem of “mixed pixels” in the Landsat data. Further investigations are needed to develop a broader range of case-studies and to acquire coincident in situ measurements for enabling a detailed analysis of melt-pond signatures (e.g. relationship to melt-pond depth) in the ETM+ data. Whereas clouds can be detected using band 5 or 7, cloud shadows alter the spectral signatures and therefore must be detected visually before large-scale operational analyses can be carried out.

# Evaluation of Late Summer Passive Microwave Arctic Sea Ice Retrievals

Thorsten Markus and Sverre T. Dokken

**Abstract**—The melt period of the Arctic sea ice cover is of particular interest in studies of climate change due to the albedo feedback mechanisms associated with meltponds and openings in the ice pack. The traditionally used satellite passive microwave sea ice concentration algorithms have deficiencies during the summer months due to the period's highly variable surface properties. A newly developed ice concentration algorithm overcomes some of these deficiencies. It corrects for low ice concentration biases caused by surface effects through the use of 85 GHz data in addition to the commonly used 19 and 37 GHz data and, thus, the definition of an additional ice type representing layering and inhomogeneities in the snow layer. This new algorithm will be the standard algorithm for Arctic sea ice concentration retrievals with the EOS Aqua advanced microwave scanning radiometer (AMSR-E) instrument. In this paper, we evaluate the performance of this algorithm for the summer period of 1996 using data from the special sensor microwave imager (SSM/I) which has frequencies similar to the AMSR instrument. The temporal evolution of summertime passive microwave sea ice signatures are investigated and sea ice concentration retrievals from the standard NASA team and the new algorithm are compared. The results show that the introduction of the additional sea ice type in the new algorithm leads to improved summertime sea ice concentrations. The SSM/I sea ice retrievals are validated using SAR-derived ice concentrations that have been convolved with the SSM/I antenna pattern to ensure an appropriate comparison. For the marginal ice zone, with ice concentrations ranging from 40% to 100%, the correlation coefficient of SAR and SSM/I retrievals is 0.66 with a bias of 5% toward higher SAR ice concentrations. For the central Arctic, where ice concentrations varied between 60% and 100%, the correlation coefficient is 0.87 with a negligible bias.

**Index Terms**—Arctic, passive microwave remote sensing, sea ice.

## I. INTRODUCTION

**D**URING spring and summer, the surface of the Arctic sea ice cover undergoes rapid changes that affect the surface albedo and impact the further decay of the sea ice. Later in the summer, the remaining sea ice cover sets the stage for next winter's sea ice growth. Satellite passive microwave data have widely been used to continuously monitor polar sea ice conditions. Unfortunately, summertime is the most difficult season for using passive microwave sensors to estimate accurately sea ice concentrations, i.e., the areal fraction of sea ice within a satellite pixel. The reason for this is that summer sea ice/snow surface conditions are extremely variable in time as well as in space. After the air temperatures reach 0 °C, the snow layer becomes wet, then melts and forms meltponds. These meltponds eventually melt through the sea ice causing a drainage of the pond and/or a flooding of the floes with sea water. Initially a wet snow surface behaves radiometrically as a blackbody resulting generally in overestimates of ice concentration, whereas meltponds appear as open water in the microwave signal causing an un-

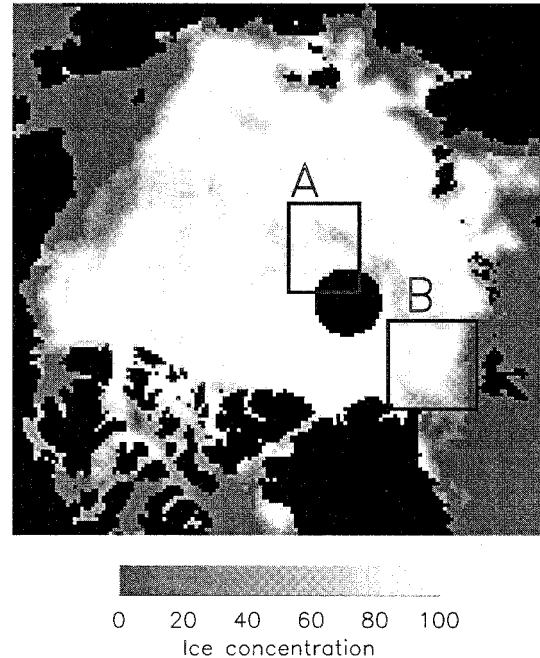


Fig. 1. September 1, 1996 Arctic ice concentration using SSM/I data and the NT2 algorithm as described in section 2. The two black boxes, labeled A and B, indicate the two regions studied in detail in this paper.

derestimate. To increase the complexity further, melt and freeze events frequently intersperse when the air temperature is oscillating about the freezing point. The evolution of summer time passive microwave signatures has been studied by several authors [1], [4], [7]–[9], [11], [14], [15], [19], [20].

A new passive microwave sea ice concentration algorithm has recently been developed [17]. This algorithm, which is briefly described in Section II, overcomes some of the shortcomings of the original NASA Team algorithm [3]; [13] as demonstrated in Comiso *et al.* [7]. In this paper, we are investigating the behavior of the new algorithm during Arctic summer conditions. First, we take ground-based measurements of emissivities of summer sea ice conditions and analyze the resulting ice concentrations for both the NASA Team and the new algorithm (Section III). We also investigate the temporal evolution of SSM/I brightness temperatures and the retrieved sea ice concentrations (Section IV). For validation, we compare the SSM/I ice concentrations with SAR sea ice concentration retrievals during September 1996 (Section V). Fig. 1 shows the two areas investigated (black boxes). In the central Arctic (box A), the SAR data cover the period from September 1, 1996 through September 7, 1996 and for the area closer to the ice edge (box B), SAR data are available for the period September 15,

1996 through September 22, 1996. These areas are coincident with ship-borne measurements. When the cloud cover disappeared, the outgoing thermal radiation often cooled the atmosphere close to the ground forming fog. The average ice thickness varied from 8 cm to 56 cm, with a thin snow cover (8 cm to 15 cm) located at 85 °N, 10 °E and southward to the marginal ice zone. In the eastern high Arctic there were no signs that a summer melt had taken place, since relatively high salinity was found in the surface parts of the second-year ice cores, investigated along the transect 85 °N 149 °E to 160 °E. On the other hand, areas closer to the ice edge i.e., south of 85 °N along 10 cm °E had experienced melting conditions. This conclusion is based on the large number of frozen melt ponds found in this part of the Arctic. Typically, the ponds were covered by 10 to 20 cm of fresh ice above a layer of fresh water on multiyear ice. Preliminary analysis of the scan SAR wide radarsat imagery from 15 and 21 August 1996 indicates that ice concentration in the high Arctic was on average 85%, which was close to visual observations made from the icebreaker bridge.

## II. SSM/I BRIGHTNESS TEMPERATURES AND ICE CONCENTRATIONS

The brightness temperatures ( $T_B$ ) from the DMSP special sensor microwave imager (SSM/I) are daily averages mapped onto a polar-stereographic projection map (commonly referred to as the SSM/I grid) available at the National Snow and Ice Data Center, Boulder, CO [NSIDC, 1992]. Ice concentrations have been derived using an enhanced version of the NASA Team sea ice concentration algorithm [17] (hereafter referred to as the NT2 algorithm). Similar to the original NASA Team (NT) algorithm [3]; [5], [6] it uses ratios of brightness temperatures in order to account for variations in physical temperature, but in addition to the 19 GHz and 37 GHz channels, the enhanced algorithm utilizes also the 85 GHz channels of the SSM/I. The incentive for using the 85 GHz channels was to correct for low concentration biases caused by surface effects primarily in parts of the Antarctic. In the NT algorithm, tiepoints for open water (OW), first-year (FY) ice and multiyear (MY) ice using the polarization at 19 GHz,

$$PR(19) = \frac{T_B(19V) - T_B(19H)}{T_B(19V) + T_B(19H)} \quad (1)$$

and the spectral gradient ratio between 37 GHz and 19 GHz at vertical polarization,

$$GR(37V19V) = \frac{T_B(37V) - T_B(19V)}{T_B(37V) + T_B(19V)} \quad (2)$$

span a triangle in which the fractions for each of the three surface types and thus, ice concentrations are calculated [Fig. 2(a)]. Low ice concentration biases result primarily from the sensitivity of the 19 GHz horizontal polarization channel to inhomogeneities such as layering in the snow cover. These lead to reduced values of  $T_B(19H)$  that result in higher  $PR(19)$  values and thus, in lower ice concentrations. As this sensitivity is not apparent in the horizontal polarization channel at 85 GHz the ratio difference

$$\Delta GR = GR(85H19H) - GR(85V19V) \quad (3)$$

provides an estimate of the amount of layering with  $T_B(19H)$  being the only channel affected. Thus,  $\Delta GR$  enables the identification of an additional surface type, labeled C. With increasing layering effects  $\Delta GR$  will also increase. In order to obtain ice concentrations the NT2 algorithm additionally uses the ratios  $PR_R(19)$  and  $PR_R(85)$ . These are polarizations rotated (therefore the subscript  $R$ ) through an angle,  $\phi$ , which is the angle between the  $GR(37V19V)$ -axis and the FY-MY line [see Fig. 2(a)] following

$$PR_R(\nu) = -GR(37V19V) \times \sin \phi_\nu + PR(\nu) \times \cos \phi_\nu \quad (4)$$

where  $\nu$  is either 19 GHz or 85 GHz. The angles  $\phi_\nu$  for 19 and 85 GHz and for both hemispheres are given in [17]. This makes the rotated polarizations independent of FY and MY ice type fractions. Because of the increasing sensitivity to atmospheric effects with increasing frequency the new algorithm applies a forward atmospheric radiative transfer model to correct for weather in the ice concentration retrievals. Therefore, we not only have one tiepoint for each surface type but several for each modeled atmospheric state. Fig. 2(b) and 2(c) show scatter plots of the same SSM/I data as in Fig. 2(a) for  $\Delta GR$  versus  $PR_R(19)$  and  $\Delta GR$  versus  $PR_R(85)$ , respectively. Modeled ratios (tiepoints) for the pure surface types with different atmospheric conditions are indicated as grey circles. Fig. 3(a) presents a flow chart of the algorithm. The ratios  $PR_R(19)$ ,  $PR_R(85)$ , and  $\Delta GR$  are calculated from the measured SSM/I brightness temperatures (this set is labeled  $\mathbf{R}$  in Fig. 3(a)). We also calculate these ratios from our model data for all ice concentrations (in 1% increments) and various atmospheric conditions ( $\langle \mathbf{R} \rangle$ ) in Fig. 3(a) and then find the best agreement between the measured and modeled ratios for each pixel. It has been demonstrated in [17] that this approach effectively corrects for cloud contamination particularly in areas of lower ice concentrations such as in the marginal sea ice zone.

## VI. CONCLUSIONS

The evolution of summer time passive microwave signatures and ice concentration are investigated and the results are compared with SAR ice concentration retrievals. This analysis shows that the NT2 sea ice concentration algorithm is better than the traditional NASA Team algorithm during the summer season. The agreement of NT2 results with the SAR retrievals is very good whereas the NT algorithm underestimates ice concentration. The reason for the improvement is based on the utilization of the 85-GHz channels and the definition of an added surface type in addition to the standard first-year and multiyear ice types. This new ice type represents areas with significant amount of inhomogeneities or layering in the snow cover. These inhomogeneities are particularly common during the summer when frequent melt and freeze events alter the snow/ice structure. Nevertheless, this study only gives hints of when and why the NT2 algorithm performs better than the NT algorithm. Dedicated high-resolution passive microwave measurements with coincident in-situ measurements of the snow/ice physical and radiative properties as well as with atmospheric observations are needed to more completely evaluate the algorithm and possibly suggest further improvements.

# Modelling the effect of temperature on the maximum growth rates of phytoplankton populations

John R. Moisan <sup>a,\*</sup>, Tiffany A. Moisan <sup>a,1</sup>, Mark R. Abbott <sup>b,2</sup>

<sup>a</sup> Laboratory for Hydrospheric Processes, NASA/GSFC Wallops Flight Facility, Wallops Island, VA 23337-5099, USA

<sup>b</sup> College of Oceanic and Atmospheric Science, Oregon State University, Corvallis, OR 97331-5503, USA

Received 3 January 2001; received in revised form 28 November 2001; accepted 20 December 2001

## Abstract

Functional relationships which parameterize growth based on the Eppley temperature relationship for phytoplankton maximal growth rates are increasingly being used in marine and freshwater ecosystem models. In this paper, we demonstrate the effect of using such generalized relationships in modelling studies. Two suites of numerical experiments are carried out to investigate the sensitivity of models to generalized growth relationships. In each experiment, 100 individual species or groups of phytoplankton are allowed to compete under a variety of growth versus temperature relationships. One suite of experiments is carried out within a simple 'chemostat' type model that is forced with seasonally varying temperature and photosynthetically available radiation (PAR) fields. A second suite of experiments is carried out using a biogeochemical mixed-layer model to demonstrate the sensitivity of these models to various temperature versus growth relationships. The key difference in the biogeochemical mixed-layer simulations is in the timing of the ecosystem response to seasonal variability of the mixed-layer depth and temperature. The Eppley growth versus temperature relationship overestimates phytoplankton growth by as much as 80% during the spring when growth rates are crucial to the timing of the spring blooms. This decrease in growth rates causes a delay in the spring phytoplankton bloom which in turn results in significant changes in all other model constituents. The results from both suites of experiments show that it is important to resolve the intrinsic growth dynamics of a population in order to properly resolve the maximum growth rates of phytoplankton populations. The results also present a possible explanation for why phytoplankton are commonly found growing within water colder than their optimal temperature for growth. A dynamic growth versus temperature model is introduced that is capable of resolving the growth dynamics of a population of phytoplankton under a variety of temperature forcing scenarios. This new growth versus temperature model/relationship will be useful in global biogeochemical models and demonstrates the importance of underlying population dynamics in controlling bulk community growth estimates. © 2002 Elsevier Science B.V. All rights reserved.

**Keywords:** Phytoplankton; Temperature; Maximum growth rate; Population

## 1. Introduction

General circulation models (GCM) are currently being coupled to ecosystem models in order to simulate global ocean ecosystems. These circulation models are based on well-understood equations of motion, state, and continuity. Marine ecologists have yet to discern such relationships or 'laws'. The development of ecological theory with

applicable equations for use in models has been slow, and the testing of these theories has been difficult due to the complex interactions between organisms and their environment.

Historically, modelling the ocean's ecosystem has been approached from an empirical perspective. Typically, ecosystem modelers develop or assemble a set of empirically-derived functions for

\* Corresponding author. Tel.: +1-757-824-1312; fax: +1-757-824-1036.

E-mail addresses: jmoisan@osb.wff.nasa.gov (J.R. Moisan), tmoisan@osb.wff.nasa.gov (T.A. Moisan), abbott@oce.orst.edu (M.R. Abbott).

<sup>1</sup> Tel.: +1-757-824-1046; fax: +1-757-824-1036.

<sup>2</sup> Tel.: +1-541-737-4045; fax: +1-541-737-2064.



each of the specific trophic levels and use these to control the flow of material between the model's components. These functions are then a fixed set of equations that are not allowed to acclimate to changes in the ecosystem that may arise naturally, such as changes in nutrient flux, temperature, light, species succession, competition, food availability, predation, and phenotypic, or on longer time scales, genotypic, changes. There are currently no ecosystem models that are based entirely on first principles (Behrenfeld and Falkowski, 1997a; Evans and Fasham, 1993). Models are generally based upon some level of empirical or bulk parameterizations. The task is to decide upon what level to parameterize the individual processes in order to accurately quantify the observed system response.

Microalgae are capable of carrying out photosynthesis and cellular division over a wide range of temperatures. The effects of temperature on marine algae have been studied extensively for many years (Berry and Bjorkman, 1980; Berry and Raison, 1981; Davison, 1991). It is well-known that phytoplankton have an optimal temperature for growth (Li, 1980). Below the optimal temperature, plant growth rates increase with temperature according to their individual  $Q_{10}$  value. The  $Q_{10}$  relationship is often parameterized using the Arrhenius function, but in a physical chemistry framework, its shape is controlled by the net effect of the Maxwell–Boltzmann relationships from all of the cellular processes which are linked to Calvin cycle enzymatic activities (Falkowski, 1980). Above the optimal temperature, growth rates decrease due to inactivation or denaturation of proteins or other factors (Ratkowsky et al., 1983).

While a general shape occurs for each growth versus temperature curve, the individual shapes vary widely between different species, and even clones of the same species (Jorgensen, 1968; Falkowski, 1977; Smayda, 1969; Yoder, 1979; Suzuki and Takahashi, 1995). The reasons for this wide range in variability may not be caused solely by temperature variability but also by changes in nutrient and light conditions under which they were grown. The optimal temperature for the curves also varies with changes in the temperature at which the phytoplankton are grown (Li, 1980). However, despite differences in the shapes of the temperature versus growth curves, a general equa-

tion can be derived for maximal growth. Eppley (1972) assembled a limited data set of growth curves from phytoplankton batch cultures. From this data set, an empirical equation was derived for estimating the maximum growth rate based on temperature,  $\mu_{\max} = \log(2) 0.851(1.066^T)$ , for a given temperature,  $T$ . Other growth rate versus temperature relationships have been proposed using data from other laboratory experiments (Ahlgren, 1987).

## 5. Conclusions

Our results demonstrate the importance of intrinsic population variability on ecosystems. The model results show that phytoplankton population growth rates do not resemble the Eppley (1972) relationship that, to date, all global ecosystem models use, nor many of the other relationships presented in Behrenfeld and Falkowski (1997a), Falkowski et al. (1998). However, the resulting population growth curves (c.f. Fig. 6) are very similar in shape to the growth versus temperature relationship obtained by Behrenfeld and Falkowski (1997b), Balch and Byrne (1994). The major differences in these curves is that the resulting growth relationship presented in this paper does not account for nutrient- and light-limitation. It is hoped that the results from this study will help lead to the development of better primary production models.

A new model for determining the maximum growth rate for a population of phytoplankton is presented that takes into account the general shape of the individual phytoplankton growth versus temperature relationships and the variability of the temperature. This new model is unique in that it is capable of resolving species succession within the global ecosystem and retains the intrinsic variability or dynamics of the population as a whole. At present, this new formulation has yet to be tested within a GCM framework. The results from the new formulation are robust when compared against simulations with 100 plus phytoplankton. Further efforts will focus on the effects of nutrient uptake variability with the hope of establishing a similar global model.



Research Signpost  
37/661 (2), Fort P.O., Trivandrum-695 023, Kerala, India

Recent Res. Devel. Geophysics, 4 (2002): 105-117 ISBN: 81-7736-078-0

## Recent developments in satellite microwave remote sensing of soil moisture

Manfred Owe

Goddard Space Flight Center, S-54967-G, Receiving/Bldg 16W, Code 239, Soil Conservation Road  
Greenbelt, MD 20771-0001, U.S.A

### Abstract

*Significant research developments in microwave remote sensing of soil moisture have occurred over the last ten years. These developments have been brought about largely through a combination of modelling and field studies. Field studies are usually instrument oriented, and typically consist of ground-based radiometer studies, aircraft missions, and often satellite studies. Modelling studies have been conducted both independently and in support of instrument programs. A number of key modelling studies have been conducted with retrospective satellite data sets. The Scanning Multichannel Microwave Radiometer (SMMR), which was carried on board the Nimbus-7 satellite, has provided an important 9-year (1978-1987) global data set of microwave observations, and has been the basis for a number of important microwave-based soil moisture studies. Results from several of these studies, along with results from some instrument field studies are presented.*

### Introduction

Surface moisture is an important link between the land surface and the atmosphere. It has direct influence on the exchange of heat and moisture between these two sinks, and as such is an important element in the global circulation process. Surface soil moisture has been identified as a parameter of significant potential for improving the accuracy of large-scale land surface-atmosphere interaction models. However, soil moisture is quite difficult to measure accurately both temporally and spatially, especially at large spatial scales. Soil moisture changes constantly, as a result of precipitation, evaporation processes (which includes extraction by vegetation), and redistribution within the soil. Soil moisture is highly variable at both small and large spatial scales, due largely to the variability of precipitation and the heterogeneity of the land surface (e.g. vegetation, soil physical properties, topography, etc.). While point sampling of soil moisture is generally thought to be the most accurate, the observed value is usually representative only of a relatively small area immediately surrounding the measurement. Subsequent spatial averaging of these measurements, especially at scales up to  $10^2 - 10^3 \text{ km}^2$  or larger, will often introduce large errors. Since remotely sensed land surface measurements are already a spatially averaged value, they are a logical input parameter to regional or larger-scale land process models. Regular and improved estimates of soil moisture have been shown to significantly enhance the performance of GCM's and certain mesoscale models, such as flood forecast models [1].

Microwave remote sensing has been used to monitor surface soil moisture with increasing degrees of success. Both ground-based [2-5] and airborne radiometer experiments [6,7] have generally provided good results, largely because of good quality observations of supporting land surface properties such as soil moisture,

vegetation, and surface temperature. These experiments are generally supported by intensive soil moisture measuring programs, to ensure optimum spatial representation for comparison. However, satellite-based studies [8-10] have historically been less successful. This is due to a great extent, to a general inadequacy of surface observations at the larger spatial scales. Traditional satellite remote sensing studies have relied heavily on either relatively sparse ground measurements of soil moisture or modelled data, primarily for calibration purposes. These approaches would typically use a radiative transfer model to first solve for the vegetation component, which then would be related to some measurable remote sensing parameter, such as the Normalized Difference Vegetation Index (NDVI).

Recently, however, a number new soil moisture retrieval techniques have been developed. These approaches partition the observed microwave signal into its component parts, and are somewhat unique in that they do not require ground observations of soil moisture or vegetation biophysical properties for calibration purposes. This paper will briefly present some basic microwave theory and then describe the results of several theoretical applied studies which have been conducted during the past several years.

## Discussion and conclusions

Efforts to use remote sensing as a more consistent and cost effective method of monitoring the Earth and providing regular observations of various surface and atmospheric parameters has been highly successful. Certain parameters, such as vegetation biomass, snow cover, snow water equivalent, and land use classification, are reported regularly, and often in near real time through operational satellite monitoring programs. In many instances, historical global data-bases have been compiled, and have proven invaluable as validation tools.

Research in the area of microwave remote sensing has lead to important developments in recent years. A combination of field programs and modelling studies have aimed at improving the interpretation of passive microwave observations of the land surface. Developments in inverse modelling techniques have resulted in improved estimates of important land surface parameters such as soil moisture and vegetation canopy properties. Knowledge of vegetation properties such as single scattering albedo and optical depth is important because they tend to mask and distort the microwave signal. Their effect must be removed in order to obtain accurate estimates of soil moisture.

Surface soil moisture is a key factor in the partitioning of incoming radiation at the land surface. It is a common link between the moisture and energy balances, which are the physical bases for land surface modelling. While the importance of soil moisture is largely understood, independent spatial estimates at local to global scales are still largely unavailable. This lack of soil moisture information has had a negative affect on land process modelling efforts.

Passive microwave remote sensing presents the greatest potential for providing this information at regular spatial and temporal scales. Reliable estimates of surface moisture should provide the necessary input for improved predictions of global circulation. Real time estimates should also improve weather and climate modelling efforts, while the development of retrospective data sets will provide necessary information for simulation and validation of long term climate and global change studies. Additional applications of these data include desertification and drought monitoring, agricultural forecasting, and flood potential prediction.

Research results have demonstrated strong potential for deriving soil moisture from C-band microwave systems, and should provide a basis for further development and application of inverse modelling techniques at this frequency. This is especially important, in light of the upcoming launch of the NASA AQUA platform, and since the development of longer wavelength systems is still uncertain for the foreseeable future.

Plans are currently underway, to develop a more than 20-year database of historical global surface soil moisture. Because the Nimbus-7 SMMR data are available only through mid-1987, the data will be extended with Defense Satellite Mapping Program (DSMP) Special Sensor Microwave/Imager (SSM/I) observations from the beginning of August 1987. However, since the lowest frequency on the SSM/I is 19 GHz, which corresponds to a wavelength of only about 1.6 cm, the SSM/I data product will be somewhat degraded. Nevertheless, it should still be useful for hydrological modelling purposes. The dataset will again revert back to C-band, after the launch of the new AQUA satellite, currently scheduled for late 2001. The database will be in the form of daily global maps of soil moisture. Expected errors will be based on the calculated vegetation optical depth. The data product will be made available to the general public, through the Goddard Space Flight Center Distributed Active Archive Center (DAAC).

# Hydrologic Data Assimilation with the Ensemble Kalman Filter

ROLF H. REICHLE,\* DENNIS B. MCLAUGHLIN, AND DARA ENTEKHABI

*Ralph M. Parsons Laboratory, Department of Civil and Environmental Engineering, Massachusetts Institute of Technology, Cambridge, Massachusetts*

(Manuscript received 28 December 2000, in final form 22 March 2001)

## ABSTRACT

Soil moisture controls the partitioning of moisture and energy fluxes at the land surface and is a key variable in weather and climate prediction. The performance of the ensemble Kalman filter (EnKF) for soil moisture estimation is assessed by assimilating L-band (1.4 GHz) microwave radiobrightness observations into a land surface model. An optimal smoother (a dynamic variational method) is used as a benchmark for evaluating the filter's performance. In a series of synthetic experiments the effect of ensemble size and non-Gaussian forecast errors on the estimation accuracy of the EnKF is investigated. With a state vector dimension of 4608 and a relatively small ensemble size of 30 (or 100; or 500), the actual errors in surface soil moisture at the final update time are reduced by 55% (or 70%; or 80%) from the value obtained without assimilation (as compared to 84% for the optimal smoother). For robust error variance estimates, an ensemble of at least 500 members is needed. The dynamic evolution of the estimation error variances is dominated by wetting and drying events with high variances during drydown and low variances when the soil is either very wet or very dry. Furthermore, the ensemble distribution of soil moisture is typically symmetric except under very dry or wet conditions when the effects of the nonlinearities in the model become significant. As a result, the actual errors are consistently larger than ensemble-derived forecast and analysis error variances. This suggests that the update is suboptimal. However, the degree of suboptimality is relatively small and results presented here indicate that the EnKF is a flexible and robust data assimilation option that gives satisfactory estimates even for moderate ensemble sizes.

## 1. Introduction

Near-surface soil moisture is a key variable in the atmospheric and hydrologic models that are used to predict weather and climate. Since soil moisture controls the partitioning of moisture and energy fluxes at the land surface, it has an important influence on the hydrologic cycle over timescales ranging from hourly to interannual. Land surface fluxes in turn affect the evolution of vertical buoyancy in the atmospheric column and also affect the baroclinicity that develops in the horizontal plane (Pan et al. 1995; Paegle et al. 1996). The formation and growth of clouds as well as the evolution of precipitating weather systems over land are affected by surface fluxes and surface soil moisture (Shaw et al. 1997). In fact, the timescale of soil moisture anomalies is at least on the order of several days, which is the forecast-lead horizon of operational weather forecasts.

At seasonal to interannual timescales, predictability of climatic variables such as precipitation is dependent on the land surface boundary conditions of the climate system. Koster et al. (2000) show that over the United States and other large continental regions soil moisture rivals sea surface temperature in explaining the variance in seasonal precipitation anomalies. Increasingly soil moisture and the memory associated with it are recognized to have important roles in the feedback mechanisms that intensify and prolong climate anomalies.

Despite the importance of soil moisture in weather and climate prediction there are currently no operational networks of in situ sensors that provide data suitable for these applications. Since such networks are logistically infeasible and prohibitively expensive, the focus

has turned to remote sensing techniques that provide additional information about the land surface at large scales. In particular the L-band (1.4 GHz) microwave brightness temperature of the land surface is correlated with surface soil moisture because of the sharp contrast between the dielectric constants of water and soil minerals (Njoku and Entekhabi 1995).

Interpretation of remotely sensed passive and active microwave measurements is complicated by the effects of canopy microwave optical thickness, surface micro-roughness, and physical temperature. Remote sensing measurements are only one of many data sources that provide valuable information about soil moisture. Precipitation, soil texture, topography, land use, and a variety of meteorological variables influence the spatial distribution and temporal evolution of soil moisture. We can gain additional information from a coupled model of the soil–vegetation–atmosphere system that relates the measured variables to one another and to soil moisture. Yet uncertainties in the forcing data, the heterogeneity of the land surface at various scales, and the nonlinear nature of land–atmosphere interactions limit our ability to accurately model and predict the state of the land surface and the associated fluxes.

Modern data assimilation theory provides methods for optimally merging the information from uncertain remote sensing observations and uncertain land model predictions (Errico 1999; Errico et al. 2000). Among the prior work on large-scale soil moisture assimilation are studies by Bouttier et al. (1993) and Rhodin et al. (1999) who assimilate low-level air temperature and relative humidity to estimate soil moisture. This approach

aims at improving numerical weather prediction and treats soil moisture as a tuning parameter. Houser et al. (1998) focus on the four-dimensional assimilation of in situ observations and soil moisture retrievals. The weak-constraint variational method of Reichle et al. (2001b) yields near-optimal estimates of the land surface states from direct assimilation of microwave observations. Reichle et al. (2001a) prove the concept of optimal downscaling for the case where soil moisture estimates are required at scales smaller than the scale of the microwave observations. They also show that soil moisture can be satisfactorily estimated even if quantitative precipitation estimates are not available.

In this paper we examine the feasibility of using the ensemble Kalman filter (EnKF) for soil moisture data assimilation. The EnKF is an attractive option for land surface applications because (i) its sequential structure is convenient for processing remotely sensed measurements in real time, (ii) it provides information on the accuracy of its estimates, (iii) it is relatively easy to implement even if the land surface model and measurement equations include thresholds and other nonlinearities, and (iv) it is able to account for a wide range of possible model errors. On the other hand, the EnKF relies on a number of assumptions and approximations that may compromise its performance in certain situations.

The EnKF and variants have been successfully applied to meteorological and oceanographic problems of moderate complexity in small- to medium-sized domains (Evensen and van Leeuwen 1996; Houtekamer and Mitchell 1998; Lermusiaux 1999; Madsen and Canizares 1999; Keppenne 2000). Hamill et al. (2000) provide an excellent discussion of the state of the art of ensemble forecasting and assimilation methods in the meteorological and oceanographic context. The models of geophysical flow used in most of these studies are chaotic in nature and typically have dominant modes that can grow rapidly within a certain subspace. Most such models also have an attractor and sample only a small subdomain of their phase space (Anderson and Anderson 1999). This greatly increases the potential to successfully apply ensemble filtering methods. By contrast, typical land surface models are dissipative in nature. Perturbations in the initial conditions tend to die out after a certain time rather than amplify. Consequently, the soil moisture ensemble filtering problem has certain distinctive aspects that merit closer investigation.

This paper evaluates the performance and computational burden of the EnKF for a synthetic experiment. As a benchmark for the EnKF we use a variational method that solves the optimal smoothing problem. We begin in section 2 with a brief review of the EnKF. The benchmark variational method is discussed in the cited references, including (Reichle et al. 2001b). In section 3 we briefly describe the land model and the setup of the synthetic experiments we use to investigate design issues. In section 4 we discuss the results of these experiments and compare the EnKF with the variational method. We conclude in section 5 with a summary of major findings.

## 5. Summary and conclusions

In this paper, we discuss the application of the ensemble Kalman filter to hydrologic data assimilation and in particular to the estimation of soil moisture from L-band microwave brightness temperature observations. We also compare the performance of the EnKF to an optimal smoother (weak-constraint variational algorithm). Both methods are applied to the same problem and use identical state and measurement equations, error statistics, and synthetically generated measurements. We conclude that with relatively few ensemble members the EnKF yields reasonable soil moisture estimates. For a state vector dimension of 4608 and a relatively small ensemble size of 30 (or 100; or 500), the actual errors in surface soil moisture at the final update time decrease by 55% (or 70%; or 80%) from the value obtained without assimilation (as compared to 84% for the optimal smoother).

The EnKF significantly underestimates the forecast error variances for 100 ensemble members. However, the error variance estimates derived by the filter are reasonably good when the ensemble size is increased to 500 members. Our results indicate that the forecast error variances vary strongly with time and space. This implies that it is very important to account for dynamic error covariance propagation. Assimilation schemes that use static forecast error covariances (e.g., statistical interpolation) are unlikely to produce the desired near-optimal estimates.

More research is required to better understand the EnKF and its variants. In particular, better understanding is needed of the role of nonlinearities and related asymmetries in the conditional forecast probability density function. We have found that nonlinearities in the model and measurement processes contribute to differences in the filtering and smoothing estimates even at the final update. In our application the state (soil moisture) is bounded above and below and its distribution cannot always be well approximated by a Gaussian pdf. For very wet or dry conditions, in particular, the soil moisture pdf exhibits considerable skewness. It is likely that the variational smoother is superior to the EnKF when dealing with nonlinear and non-Gaussian effects. However, it is important to recognize that the variational approach is designed to estimate the mode of the conditional forecast density while the EnKF is designed to estimate the mean. So even if both approaches work as intended their estimates at the end of the smoothing interval can be expected to differ when the density is asymmetric.

In a practical application of the EnKF, it will probably be necessary to model the forecast covariance rather than to compute it in an exact sense. In the EnKF, covariance modeling could include smoothing out the ensemble-derived covariances before the update or applying the update to subregions of the computational domain. Ultimately, a hybrid filter that combines empirical forecast error covariances with dynamic error propagation via the EnKF (Hamill and Snyder 2000) may be the best approach.



## Extended versus Ensemble Kalman Filtering for Land Data Assimilation

ROLF H. REICHLE

*Goddard Earth Sciences and Technology Center, University of Maryland, Baltimore County, Baltimore, and  
Hydrological Sciences Branch, NASA Goddard Space Flight Center, Greenbelt, Maryland*

JEFFREY P. WALKER

*The University of Melbourne, Parkville, Victoria, Australia*

RANDAL D. KOSTER AND PAUL R. HOUSER

*Hydrological Sciences Branch, NASA Goddard Space Flight Center, Greenbelt, Maryland*

(Manuscript received 1 October 2001, in final form 5 April 2002)

### ABSTRACT

The performance of the extended Kalman filter (EKF) and the ensemble Kalman filter (EnKF) are assessed for soil moisture estimation. In a twin experiment for the southeastern United States synthetic observations of near-surface soil moisture are assimilated once every 3 days, neglecting horizontal error correlations and treating catchments independently. Both filters provide satisfactory estimates of soil moisture. The average actual estimation error in volumetric moisture content of the soil profile is 2.2% for the EKF and 2.2% (or 2.1%; or 2.0%) for the EnKF with 4 (or 10; or 500) ensemble members. Expected error covariances of both filters generally differ from actual estimation errors. Nevertheless, nonlinearities in soil processes are treated adequately by both filters. In the application presented herein the EKF and the EnKF with four ensemble members are equally accurate at comparable computational cost. Because of its flexibility and its performance in this study, the EnKF is a promising approach for soil moisture initialization problems.

### 1. Introduction

Climate prediction at seasonal-to-interannual time-scales depends on accurate initialization of the slowly varying components of the earth's system, most notably sea surface temperature (SST) and soil moisture. While tropical SST is often the dominant source of predictability, its influence appears to be mostly limited to the Tropics (Koster et al. 2000b). Skill in the prediction of summertime continental precipitation and temperature anomalies in the extratropics may instead depend on the initialization of soil moisture and other land surface states. Since soil moisture controls the partitioning of the latent and sensible heat fluxes to the atmosphere, it can influence precipitation recycling.

The initialization of the land surface states for a seasonal climate forecast can be accomplished by assimilating soil moisture observations into the land model up to the start time of the prediction. With assimilation we attempt to combine the information from the observations and the model in an optimum way. Since for seasonal forecasts we are only interested in the estimates at the start time of the prediction, sequential assimilation methods like Kalman filters are ideally suited to the task. The well-known extended Kalman filter (EKF) can be used for nonlinear applications, but the computational demand resulting from the error covariance integration limits the size of the problem (Gelb 1974). For this reason, the EKF has been used mostly for problems that focus on the estimation of the vertical soil moisture profile (Katul et al. 1993; Entekhabi et al. 1994). More

recently, Walker and Houser (2001) have applied the EKF to soil moisture estimation across the North American continent by neglecting all horizontal error correlations and treating surface hydrological units (catchments) independently. This yields an effectively low-dimensional filter.

The ensemble Kalman filter (EnKF) is an alternative to the EKF (Evensen 1994). The EnKF circumvents the expensive integration of the state error covariance matrix by propagating an ensemble of states from which the required covariance information is obtained at the time of the update. Reichle et al. (2002) applied the EnKF to soil moisture estimation and found that it performed well against a variational assimilation method. Since the variational approach generally requires the adjoint of the hydrologic model, which is not usually available and is difficult to derive, the obvious choices for advanced land assimilation algorithms are the EKF and the EnKF. There are many variants of the EKF and the EnKF that have been used in meteorology and oceanography, notably reduced-rank square root algorithms (Verlaan and Heemink 1997), particle filters (Pham 2001), methods that use pairs of ensembles (Houtekamer and Mitchell 1998), and hybrid approaches that combine ensembles with reduced-rank approaches (Heemink et al. 2001; Lermusiaux and Robinson 1999) or with variational methods (Hamill and Snyder 2000). In this paper, we focus on the relative merits of using the traditional EKF and EnKF for soil moisture assimilation.

The major differences between the EKF and the EnKF are (i) the approximation of nonlinearities of the hydrologic model and the measurement process (the EKF uses a linearized equation for the error covariance propagation while the EnKF nonlinearly propagates a finite ensemble of model trajectories), (ii) the range of model errors that can be represented (the EnKF can account for a wider range of model errors), (iii) the ease of implementation (the EKF requires derivatives of the nonlinear hydrologic model, evaluated numerically or from a tangent-linear model), (iv) computational efficiency (it must be determined how many ensemble members are needed in the EnKF to match the performance of the EKF), and (v) the treatment of horizontal correlations in the model or measurement errors (the EKF cannot account for horizontal error correlations in large systems for computational reasons). Insights into many important issues can be gained from low-dimensional versions of both filters.

Although approximate nonlinear filters such as the EKF and the EnKF have been found to work well in some applications, their value in a particular nonlinear problem cannot be assessed a priori but must be determined by simulations (Jazwinski 1970). We investigate the above differences in the context of soil moisture initialization for seasonal prediction using synthetic data in a twin experiment. Since all uncertain inputs are known by design, such experiments are well suited for a first assessment of algorithm performance. Tests with actual observations will be conducted in future studies. For retrospective analysis, surface soil moisture can be retrieved from the Scanning Multifrequency Microwave Radiometer (SMMR) for the period 1979–87 (Owe et al. 2001). These retrievals are derived from the 6.6-GHz (C band) and 37-GHz channels. Similar retrievals should soon be available from the Advanced Microwave Scanning Radiometer for the Earth Observing System (AMSR-E). In the future, passive 1.4-GHz (L band) sensors should also become available (Kerr et al. 2001).

## 5. Summary and conclusions

In this paper, we compare two promising data assimilation methods for soil moisture initialization in seasonal climate prediction. The extended Kalman filter (EKF) and the ensemble Kalman filter (EnKF) were used to assimilate synthetic surface soil moisture observations into the Catchment Model, with model error parameters calibrated against actual estimation errors. The best results are obtained for both filters when the model error in the root zone excess is large compared to the model errors in the surface excess and the catchment deficit. Using the calibrated filter parameters we find that the EKF and the EnKF produce satisfactory estimates of soil moisture.

The EKF and the EnKF (with four ensemble members) show comparable performance for comparable computational effort. For 10 or more ensemble members, the EnKF outperforms the EKF. This is ascribed to the EnKF's flexibility in representing nonadditive

model errors. The actual estimation errors of the EnKF converge quickly with increasing ensemble size, even though the filter-derived (expected) error covariances are noisy for small ensembles. The numerical differentiation scheme used in the EKF requires frequent checks in order to avoid divergent error covariances or loss of positive definiteness. Although these checks interrupt the integration of the error covariances, and information from earlier updates is partially lost, they are not a major source of error.

The normalized innovations are found to be inconsistent with a standard normal distribution. This is because our representation of model errors cannot fully account for the effects of uncertainties in the forcing and imperfectly known model parameters that we use in our twin experiment. Nonlinearities in the land model generate skewness in the distribution of ensemble states. But this skewness information is only very approximately used in the EnKF update and is not available in the EKF. Fortunately, the nonlinearities are not a dominant source of error, because the local linearization strategy of the EKF is for the most part successful and because the nature of the soil moisture bounds limits the actual estimation errors.

Catchment-to-catchment error correlations could arise from large-scale errors in the forcing or from unmodeled lateral fluxes such as river or groundwater flow. Moreover, satellite data are likely to exhibit horizontal error correlations. The present paper compares the EKF and EnKF under the assumption that horizontal error correlations can be neglected. The importance of such correlations is a topic of active research. If horizontal error correlations turn out to be important, information can be spread laterally, in particular from observed to unobserved catchments. When horizontal error correlations are taken into account in the EnKF, small error correlations associated with observations that are far apart must be filtered out (Mitchell and Houtekamer 2000). For computational reasons, the EKF must be approximated using a rank-reduction technique such as the reduced-rank square root method (Verlaan and Heemink 1997).

Before soil moisture assimilation can become a routine tool for seasonal climate prediction, many more questions will need to be addressed. Important areas of research include the investigation of multivariate assimilation using more Catchment Model prognostic variables as states, the direct assimilation of radiances as opposed to soil moisture retrievals, and the assimilation of other types of remote sensing data such as soil temperatures or vegetation parameters. Finally, soil moisture estimates from the assimilation must then be shown to improve the accuracy of seasonal climate forecasts. In summary we can say that the EnKF is more robust and offers more flexibility in covariance modeling (including horizontal error correlations). This leads to its slightly superior performance in our study and makes the EnKF a promising approach for soil moisture initialization of seasonal climate forecasts.

# Coastal polynyas in the southern Weddell Sea: Variability of the surface energy budget

Ian A. Renfrew and John C. King

British Antarctic Survey, Cambridge, UK

Thorsten Markus

NASA Goddard Space Flight Center, Greenbelt, Maryland, USA

Received 16 November 2000; revised 13 August 2001; accepted 26 September 2001; published 28 June 2002.

[1] The surface energy budget of coastal polynyas in the southern Weddell Sea has been evaluated for the period 1992–1998 using a combination of satellite observations, meteorological data, and simple physical models. The study focuses on polynyas that habitually form off the Ronne Ice Shelf. The coastal polynya areal data are derived from an advanced multichannel polynya detection algorithm applied to passive microwave brightness temperatures. The surface sensible and latent heat fluxes are calculated via a fetch-dependent model of the convective-thermal internal boundary layer. The radiative fluxes are calculated using well-established empirical formulae and an innovative cloud model. Standard meteorological variables that are required for the flux calculations are taken from automatic weather stations and from the National Centers for Environmental Prediction/National Center for Atmospheric Research reanalyses. The 7 year surface energy budget shows an overall oceanic warming due to the presence of coastal polynyas. For most of the period the summertime oceanic warming, due to the absorption of shortwave radiation, is approximately in balance with the wintertime oceanic cooling. However, the anomalously large summertime polynya of 1997–1998 allowed a large oceanic warming of the region. Wintertime freezing seasons are characterized by episodes of high heat fluxes interspersed with more quiescent periods and controlled by coastal polynya dynamics. The high heat fluxes are primarily due to the sensible heat flux component, with smaller complementary latent and radiative flux components. The average freezing season area-integrated energy exchange is  $3.48 \times 10^{19}$  J, with contributions of 63, 22, and 15% from the sensible, latent, and radiative components, respectively. The average melting season area-integrated energy exchange is  $-5.31 \times 10^{19}$  J, almost entirely due to the radiative component. There is considerable interannual variability in the surface energy budget. The standard deviation of the energy exchange during the freezing (melting) season is 28% (95%) of the mean. During the freezing season, positive surface heat fluxes are equated with ice production rates. The average annual coastal polynya ice production is  $1.11 \times 10^{11}$  m<sup>3</sup> (or 24 m per unit area), with a range from  $0.71 \times 10^{11}$  (in 1994) to  $1.55 \times 10^{11}$  m<sup>3</sup> (in 1995). This can be compared to the estimated total ice production for the entire Weddell Sea: on average the coastal polynya ice production makes up 6.08% of the total, with a range from 3.65 (in 1994) to 9.11% (in 1995). **INDEX TERMS:** 3349 Meteorology and Atmospheric Dynamics: Polar meteorology; 4540 Oceanography: Physical: Ice mechanics and air/sea/ice exchange processes; 4207 Oceanography: General: Arctic and Antarctic oceanography; 4504 Oceanography: Physical: Air/sea interactions (0312); **KEYWORDS:** polynyas, sea ice, Weddell Sea, surface energy budget, surface fluxes, high-salinity shelf water

## 1. Introduction

[2] Coastal polynyas are regions of open water, or thin ice, formed by offshore winds blowing the sea ice pack out to sea. Their fixed locations provide a focus for wintertime air-sea-ice interactions within the polar regions, as the exposure of belts of relatively warm water to the cold polar atmosphere allows the exchange of vast quantities of heat, cooling the surface ocean and warming the boundary layer of the atmosphere. If the ocean is at freezing point, the cooling results directly in ice production; hence there is a release of latent heat and a rejection of salt as ice is formed. The rejected salt-enriched brine acts as a positive density forcing [e.g., Curry and Webster, 1999]. The atmospheric warming leads to changes in boundary layer dynamics, for

example, the generation of convective plumes and, in general, an increase in boundary layer winds due to downward momentum transport [e.g., Dare and Atkinson, 1999]. The latent heat of fusion released as ice forms within wind-generated polynyas means they are often referred to as “latent heat” polynyas [e.g., Smith *et al.*, 1990].

[3] The impact of coastal polynyas on the ocean is important for several reasons. The fixed location, tied to the coastline and in regions prone to strong wind forcing, means the density forcing of the ocean is also spatially fixed. Indeed, as the air-sea exchange within a polynya is 1 or 2 orders of magnitude greater than through the surrounding sea ice, the local ocean forcing is likely to be dominated by the coastal polynya contribution. In this study we focus



on the coastal polynyas that habitually form off the Ronne Ice Shelf, in the southern Weddell Sea (Figure 1). This is an important region oceanographically as it is in the Weddell Sea that the major portion of Antarctic Bottom Water (the most extensive water mass in the world ocean) is thought to be generated through a number of pathways [e.g., *Foldvik and Gammelsrød*, 1988]. Most of the pathways have as a starting point High Salinity Shelf Water, a dense water mass formed by salinization of Circumpolar Deep Water over the continental shelf. The salinization is caused by the production of sea ice, and as coastal polynyas tend to be located over the continental shelves, they are thought to be the primary production sites of High Salinity Shelf Water.



**Figure 1.** A map of the southern Weddell Sea region. The study region is marked by the inner rectangle.

## 6. Conclusions

[51] The surface energy budget of coastal polynyas in the southern Weddell Sea has been investigated through the combination of satellite observations, meteorological data, and simple physical models. The surface energy budget time series are illustrated through Figures 10–15 and Tables 4–7. For coastal polynyas in the freezing season, positive sensible heat fluxes dominate the surface energy budget, with latent and radiative heat fluxes generally augmenting the oceanic cooling. The turbulent heat fluxes are characterized by episodes of high heat fluxes, interspersed with more quiescent periods. Coastal polynya dynamics set the timescales for these changes: strong offshore winds blow open the polynyas, which then refreeze at rates determined by the atmospheric and oceanic conditions. The total wintertime energy exchange is related to the cumulative coastal polynya area (indeed, the turbulent heat fluxes are strongly related); however, the varying atmospheric boundary layer is also important in modifying the fluxes. On average, the total

energy exchange is  $3.48 \times 10^{19}$  J, with contributions of 63, 22, and 15% from the sensible, latent, and radiative terms, respectively. The wintertime energy exchange is not related to the length of the freezing season. For coastal polynyas in the melting season the area-integrated fluxes are dominated by the absorption of shortwave radiation. Over the 7 year period from 1992 to 1998 the ocean warms more than it cools through the presence of coastal polynyas. In particular, the anomalous summertime open water area of 1997–1998 allowed an enormous area-integrated warming of the ocean.

[52] During the freezing season, positive surface heat fluxes have been equated with ice production rates. The mean average coastal polynya ice production per unit area is 24.0 m, with a range from 15.6 (in 1998) to 31.7 m (in 1992). In terms of total annual coastal polynya ice production the mean is  $1.11 \times 10^{11}$  m<sup>3</sup> with a range from  $0.71 \times 10^{11}$  (in 1994) to  $1.55 \times 10^{11}$  m<sup>3</sup> (in 1995). The interannual variability is large: the standard deviation is 28% of the annual mean. Ice production has roughly a normal distribution over the freezing season, with strong modifications due to the episodic nature of the time series, for example, coastal polynya opening episodes may span a couple of months. These ice production calculations are compared to estimates of the ice production in the entire Weddell Sea from passive microwave data and an assumed average ice thickness of 0.5 m. The mean coastal polynya ice production is 6.08% of the entire Weddell Sea ice production, although this ratio varies from 3.65 (in 1994) to 9.11% (in 1995). The total annual Weddell Sea ice production does not vary that much: the standard deviation is only 5% of the mean. Hence variability in the ratio is determined primarily by changes in the coastal polynya ice production.

[53] An estimate of the accuracy of these results can be made through a comparison of the 1998 AWS and NCEP surface energy budgets. In the mean the components match remarkably well (to within  $10 \text{ W m}^{-2}$ ). The correlation coefficients are over 0.75, and the linear regression slopes are over 0.8. The differences in mean monthly ice production are 8% over the whole year but only 2% if the anomalous months of February and March 1998 are ignored. This suggests that the use of the NCEP model data is well founded. For example, we would expect the time series to be accurate to within  $\sim 5\%$  in terms of annual ice production. In addition to this however, there will be errors associated with (1) the determination of the sea ice cover, (2) the representativeness of the meteorological data, (3) the neglected physical processes in the CIBL model, and (4) the use of simple formulae for the radiative terms. We would estimate absolute errors associated with the above to be of the order 20%, in terms of the annual ice production, for example, but much less than that, of order 10%, when examining the interannual variability within the climatology. We are therefore confident that the interannual variability described here is genuine.

[54] A number of directions for future research have become apparent during this study. The transformation of this surface energy budget into an oceanic buoyancy forcing is one objective of future work. To do this will involve the assessment of a number of physical processes that affect both the heat flux and, in particular, the freshwater flux, for example, precipitation, blowing snow deposition, ice shelf melt, and changes in the oceanographic conditions. The buoyancy forcing is a key ingredient for ongoing studies of sub-ice shelf oceanography and bottom water formation [Nicholls and Makinson, 1998; Comsio and Gordon, 1998], and so, a study along these lines is planned.

# A Parameterized Surface Reflectivity Model and Estimation of Bare-Surface Soil Moisture With L-Band Radiometer

Jiancheng Shi, *Senior Member, IEEE*, K. S. Chen, *Senior Member, IEEE*, Qin Li, Thomas J. Jackson, *Fellow, IEEE*, Peggy E. O'Neill, and Leung Tsang, *Fellow, IEEE*

**Abstract**—Soil moisture is an important parameter for hydrological and climatic investigations. Future satellite missions with L-band passive microwave radiometers will significantly increase the capability of monitoring earth's soil moisture globally. Understanding the effects of surface roughness on microwave emission and developing quantitative bare-surface soil moisture retrieval algorithms is one of the essential components in many applications of geophysical properties in the complex earth terrain by microwave remote sensing. In this study, we explore the use of the integral equation model (IEM) for modeling microwave emission. This model was validated using a three-dimensional Monte Carlo model. The results indicate that the IEM model can be used to simulate the surface emission quite well for a wide range of surface roughness conditions with high confidence. Several important characteristics of the effects of surface roughness on radiometer emission signals at L-band 1.4 GHz that have not been adequately addressed in the current semiempirical surface effective reflectivity models are demonstrated by using IEM-simulated data. Using an IEM-simulated database for a wide range of surface soil moisture and roughness properties, we developed a parameterized surface effective reflectivity model with three typically used correlation functions and an inversion model that puts different weights on the polarization measurements to minimize surface roughness effects and to estimate the surface dielectric properties directly from dual-polarization measurements. The inversion technique was validated with four years (1979–1982) of ground microwave radiometer experiment data over several bare-surface test sites at Beltsville, MD. The accuracies in random-mean-square error are within or about 3% for incidence angles from 20° to 50°.

**Index Terms**—L-band radiometer, soil moisture, surface emission.

## I. INTRODUCTION

SOIL MOISTURE is a key parameter in numerous environmental studies, including hydrology, meteorology, and agriculture. Previous investigations have established the fundamentals of passive microwave remote sensing as an important tool in determining the physical properties of soils [1]–[8]. The ability to estimate soil moisture in the surface layer to an approximately 5-cm depth by microwave remote sensing at 1.4 GHz has been demonstrated under a variety of topographic and land cover conditions. Application of microwave retrieval of soil moisture to hydrological and meteorological sciences has been influenced by the natural variability and complexity of the vegetation canopy and surface roughness that significantly affect the sensitivity of emission measurements to soil moisture. At high frequencies (C-band or higher), it is well understood that the instrument's ability to monitor soil moisture is limited by vegetation cover. At lower frequencies, this problem can be greatly reduced. Two possible future spaceborne L-band multipolarization passive microwave techniques—two-dimensional synthetic aperture interferometry

[5], [8] and filled-aperture mesh deployable reflectors [9]—will significantly increase the capability of monitoring earth's soil moisture globally. In addition to operating at long wavelengths, these multipolarization instruments provide an opportunity to utilize multiple polarization data in the estimation of soil moisture. The full utilization of these data will require a further understanding of surface roughness effects on the emission signals, especially on the relationships of the emission signals at different polarizations, in order to develop a quantitative algorithm for global soil moisture mapping.

The surface reflectivity model is one of the essential components in many applications of microwave remote sensing of geophysical properties in complex earth terrain. It is a direct component in monitoring soil moisture in bare or vegetated surfaces and serves as the boundary condition in studying snow, vegetation, and atmospheric properties. Currently, there are two types of approaches used to model surface reflectivity:

- 1) *semiempirical approach*: this type of model is generally found to be easy to use without significant computing efforts and is generally easy to implement as an inversion model;
- 2) *physical modeling approach*: the surface reflectivity can be obtained by integrating the bistatic scattering coefficient over the upper hemisphere [10].

The most commonly used semiempirical model that describes the bare-surface emission as a function of the surface roughness and dielectric properties is the so-called Q/H model [11], [12]. The parameter Q describes the energy emitted in orthogonal polarizations due to surface roughness effects. H is a measure of the effect of surface roughness to increase surface emissivity. However, it has been recognized that there can be a great difference between the direct physical measurements of surface roughness in the field and those derived by fitting the Q/H model with observed soil moisture or dielectric constant measurements [13], [14]. Commonly, the surface roughness parameter in the Q/H model has to be determined empirically from the experiment data and often is called "effective roughness." This is an inconvenient technique to apply in either the forward calculation to relate the soil moisture with microwave radiometer measurements or the inverse calculation, since there are no quantitative relationships between the empirical roughness parameter and the commonly used measurable surface roughness characteristics such as the root-mean-square (rms) height  $s$ , the autocorrelation length  $l$ , and the autocorrelation function.

Attempts to improve understanding of the effects of surface roughness and how traditional surface roughness parameters can



be directly related to emission signals have resulted in the development of several surface reflectivity models. In comparison with the Q/H model, all of these models determined that the Q parameter is not very important [14]–[17]. Depending on the empirical data sources and the techniques used to develop the reflectivity models, the H parameter can have a variety of different forms.

- Mo and Schmugge [15] simulated the effects of surface roughness on the effective surface reflectivity using the Kirchhoff model and compared L- and C-band measurements from three field sites with different roughness conditions. They found that the H parameter depends on soil moisture and the ratio of  $s/l$  and that it varies with the incidence angle and polarization.
- Saatchi *et al.* [16] used the traditional surface scattering models—small perturbation model, physical optical model, and geometric optical model—to simulate the effect of surface roughness for horizontal (H) polarization and compared the results with experimental data over a frequency range of 1–12 GHz. A parameterized reflectivity model was developed with two (coherent and noncoherent) components. Unfortunately, vertical (V) polarization was not studied.
- Wegmüller and Mätzler [14] developed an empirical rough-surface reflectivity model using ground radiometer measurements with frequencies ranging from 1–100 GHz and with incidence angles of  $20^\circ$  to  $70^\circ$ . The reported accuracies of the surface reflectivity in terms of the random-mean-square errors (rmse) were 0.095 and 0.061 for H and V polarizations, respectively. This level of accuracy is about 20% of the dynamic range of the surface emission response to soil moisture.
- Wigneron *et al.* [17] also developed an empirical rough-surface reflectivity model using experimental measurements over seven different roughness conditions at L-band 1.4 GHz and incidence angles  $\leq 40^\circ$ . The reported accuracy for the surface reflectivity was 0.031 (rmse). This study concluded that the H parameter is independent of both incidence angle and polarization.

## VII. CONCLUSION

Understanding the effects of surface roughness on microwave emission and developing quantitative bare-surface soil moisture retrieval algorithms are essential to many applications of geophysical properties in complex earth terrain by microwave remote sensing. In this study, we first validated the IEM model with a highly accurate but complex 3-D Monte Carlo model. A comparison showed that the IEM model slightly overestimates the emissivity for V polarization with rmse of 0.008 and 0.013 at  $40^\circ$  and  $50^\circ$  incidence angles, respectively. For H polarization, the errors were more random with rmse of 0.01 and 0.017 at  $40^\circ$  and  $50^\circ$ . The results indicate that the IEM model can be used to simulate the surface emission quite well for a wide range of surface roughness and conditions.

Then, we used an IEM model to simulate a database with a wide range of surface roughness and dielectric conditions.

Using the IEM-simulated data, we demonstrated several important characteristics of surface roughness effects on microwave emission signals that were not incorporated in currently used surface effective reflectivity models. It was found that the effects of surface roughness on microwave emission signals at V and H polarization might be different in both magnitude and direction, depending on the incidence angle, surface roughness, and dielectric properties. The overall effect of surface roughness can be explained by the combined effects from two components: the coherent component that decreases as the surface roughness increases and the noncoherent component that increases as the roughness changes. As a result, the total reflected energy may have two outcomes when comparing rough and flat surfaces. If the amount of reduction in the coherent component of the reflected energy is greater than the increase in noncoherent scattering, surface roughness reduces the effective reflectivity. This represents all cases for H polarization at all incidence angles. However, when the amount of the reduction in the coherent component of the reflected energy is less than the increase in the noncoherent scattering, surface roughness actually increases the effective reflectivity. This only occurs in V polarization. As a result, the surface effective reflectivity in V polarization could be greater than its corresponding Fresnel reflectivity depending on the incidence angle, surface roughness, and dielectric properties. This also impacts roughness effects on the polarization ratio V/H measurements. These two important characteristics have been not incorporated in the currently available semiempirical surface effective reflectivity models.

We developed a surface effective reflectivity model for L-band (1.4 GHz) utilizing both V and H polarizations and three typical correlation functions (gaussian, 1.5-power, and exponential) by parameterizing the IEM model simulated data for a wide range of surface soil moisture and roughness properties. When compared to the IEM model simulated data, the parameterized model in (4) has the accuracy (rmse) better than 0.01 for V polarization at all incidence angles with the best accuracy (0.0035) at  $40^\circ$ . For H polarization, the accuracy increases as the incidence angle increases with the worst accuracy (0.011) at  $20^\circ$  and the best accuracy (0.0028) at  $60^\circ$ . These results indicate that the parameterized model can reproduce the IEM model predictions over a wide range of surface roughness conditions.

Using the IEM model simulated database for a wide range of surface soil moisture and roughness properties, we developed an inversion model that uses dual polarization measurements to minimize surface roughness effects and to estimate surface dielectric properties directly. For the IEM model simulated data, the algorithm in (8) has an accuracy of 1.68% at  $20^\circ$ . The accuracy increases as the incidence angle increases. The best accuracy can be seen at  $45^\circ$  with 0.55%. Validation of this inversion technique with ground microwave radiometer experiment data indicated that there was an overall trend for soil moisture underestimation in the algorithm performance. However, all rmse are within or about 3% for incidence angle between  $20^\circ$  and  $50^\circ$ .

# Influence of Microphysical Cloud Parameterizations on Microwave Brightness Temperatures

Gail M. Skofronick-Jackson, *Member, IEEE*, Albin J. Gasiewski, *Senior Member, IEEE*, and James R. Wang, *Senior Member, IEEE*

**Abstract**—The microphysical parameterization of clouds and rain cells plays a central role in atmospheric forward radiative transfer models used in calculating microwave brightness temperatures. The absorption and scattering properties of a hydrometeor-laden atmosphere are governed by particle phase, size distribution, aggregate density, shape, and dielectric constant. This study investigates the sensitivity of brightness temperatures with respect to the microphysical cloud parameterization. Calculated wideband (6–410 GHz) brightness temperatures were studied for four evolutionary stages of an oceanic convective storm using a five-phase hydrometeor model in a planar-stratified scattering-based radiative transfer model. Five other microphysical cloud parameterizations were compared to the baseline calculations to evaluate brightness temperature sensitivity to gross changes in the hydrometeor size distributions and the ice–air–water ratios in the frozen or partly frozen phase. The comparison shows that enlarging the raindrop size or adding water to the partly frozen hydrometeor mix warms brightness temperatures by as much as 55 K at 6 GHz. The cooling signature caused by ice scattering intensifies with increasing ice concentrations and at higher frequencies. An additional comparison to measured Convection and Moisture Experiment (CAMEX-3) brightness temperatures shows that in general all but two parameterizations produce calculated  $T_B$ s that fall within the CAMEX-3 observed minima and maxima. The exceptions are for parameterizations that enhance the scattering characteristics of frozen hydrometeors.

**Index Terms**—Clouds, electromagnetic scattering, millimeter wave radiometry, rain, remote sensing, snow.

## I. INTRODUCTION

OVER the past four decades, significant effort has been devoted to understanding the microphysical cloud characteristics of convective storms (e.g., [1]–[3]). The microphysics of clouds is of considerable interest in a wide range of interdisciplinary studies. These studies include improving global climate models for understanding climate variability, investigating the role of hydrometeors in lightning generation, examining chemical interactions and rain evolution in clouds for pollution research, studying radar and lidar remote sensing applications, and developing precipitation parameter retrievals from satellite-based passive microwave imagery.

Of interest here is improving our understanding of the relationships between the microphysics of hydrometeors in a convective storm and the upwelling microwave brightness temperatures for the purposes of rain rate and precipitation parameter retrieval. A comprehensive understanding of these relationships is hindered by the lack of accurate and sufficiently detailed atmospheric microphysical profile truth [4], [5]. Difficulties in obtaining microphysical cloud profile truth for convective systems stem from limitations in remotely sensed measurements, aircraft sampling capabilities, and the extremely inhomogeneous

and complex nature of convection [6], [7]. The dynamics of convection complicate the *in situ* measurements of hydrometeor size, shape, total water content and the ice–air–water ratio, and Nyquist spatial and temporal sampling of these quantities remains a formidable challenge.

A microphysical cloud parameterization used in radiative transfer models requires specifying the size distributions and ice–air–water ratios for each hydrometeor type at each atmospheric level along with vertical profiles of temperature, relative humidity, and pressure. Parameterizations have been developed using statistics from physical models of particle growth and coalescence as well as knowledge from limited *in situ*, radar, and lidar observations. Early cloud parameterizations (e.g., [8]) used in radiative transfer models allowed for a uniform rain layer and separate cloud water layer with no ice particles. Later models added an ice layer (e.g., [9]–[12]).

Contemporary microphysical cloud parameterizations allow for multiple liquid and ice phases (e.g., [2], [4], [13], [14]). Several research studies have indicated that five hydrometeor phases adequately represent a convective storm [5], [15] from the standpoint of passive microwave signatures. The five hydrometeor phases are generally classified as cloud water, rain drops, cloud ice, snow (or ice aggregates), and graupel (including hail). The rain drops are commonly modeled by the Marshall–Palmer (MP) [16] size distribution. However there appear to be no universally accepted size distribution parameterizations or ice–air–water ratios for the other four hydrometeor types [6]. In general, the microphysical parameterizations used by radiative transfer modelers are appropriate for only specific storm occurrences.

As satellite passive microwave sensing of rain rate and other precipitation parameters (e.g., cell top altitude, see [17]) matures, it is important to understand the impact of the various common hydrometeor parameterizations on the upwelling microwave brightness. Accordingly, the purpose of this work is to study the sensitivity of computed microwave brightness temperatures to changes in the microphysical parameters. The analysis of these changes is facilitated using wideband microwave aircraft data. Since identifying the best parameterization requires detailed collocated and coincident *in situ*, radar, and radiometer observations, we instead focus on identifying a plausible class of parameterizations. Indeed, cloud parameterizations are case specific. The work of [18] and [19] are two examples where parameterizations that best match case-specific radiometer observations have been determined. Even though an optimal parameterization cannot be identified in this study, inappropriate and unrealistic parameterizations can be identified and avoided in future work.

In studying microphysical cloud parameterizations and their effect on computed brightness temperatures, a planar-stratified atmosphere and a midlatitude oceanic surface are assumed. The simple planar model is adequate for all but the most localized cumuluform convection. The highly reflective oceanic background is more uniform and provides greater sensitivity to hydrometeor scattering and absorption than would a land background, and thus represents the more conservative of the two backgrounds. For comparison purposes, four cloud profiles are selected to represent the early cumulus, evolving, mature, and dissipating stages of a convective storm. Six microphysical cloud parameterizations were selected for use in evaluating brightness temperature sensitivities to the hydrometeor size parameters, and frozen particle ice–air–water ratios. A five-hydrometeor-phase (cloud water, rain, cloud ice, dry snow, and dry graupel) parameterization is considered to be the baseline case. Brightness temperatures at twelve frequencies (6.0, 10.69, 18.7, 23.8, 36.5, 89.0, 150.0, 183.31 + 7.0, 220.0, 325 + 8.0, 340.0, and 410.0 GHz) were computed for each of the four cloud stages and six parameterizations using the planar-stratified scattering-based radiative transfer model of [11]. We discuss herein the variations in brightness temperature values when the microphysical cloud parameterization is changed in the radiative transfer calculations.

While convective storms under different prevailing conditions (e.g., tropical, midlatitude, maritime, or continental) have differing hydrometeor characteristics, this study nonetheless identifies several issues. First, in order to select the proper parameterization for any specific condition, one requires a set of detailed atmospheric truth profiles along with a collocated and coincident set of brightness temperature observations. Second, we show the sensitive relationship between the brightness temperature and the underlying hydrometeor profile. In identifying these issues we first briefly describe the radiative transfer model and calculations, including the ocean surface and top-of-atmosphere conditions. Dielectric mixing theory for heterogeneous snow and graupel particles is outlined. Section III details the six microphysical cloud parameterizations. The comparison among the six parameterizations (Section IV) and to the aircraft data (Section V) is described with a summary in Section VI.

## VI. SUMMARY

Brightness temperatures at twelve frequencies between 6.0 and 410.0 GHz were computed for four storm stages obtained from the simulated GCE model set of [36]. The four profiles used in the comparison represent a convective storm in its early cumulus, evolving, mature, and dissipating stages. The investigation illustrates how specific microphysical cloud parameterizations can affect oceanic microwave brightness temperatures.

The densities of the five hydrometeor types of the GCE data were mapped into six different microphysical cloud parameterizations. The parameterizations were designed to evaluate brightness temperature sensitivity to particle size distributions and ice–air–water ratios. A comparison among the six parameterizations, four convective storm stages, and twelve frequencies

was performed. A five hydrometeor-phase parameterization [2], [13] was considered as the baseline case.

The comparisons generally showed that increasing the emphasis of water or rain warmed the brightness temperatures. When the size distribution of rain was changed to that of the Joss *et al.* thunderstorm size distribution (which favors larger particle diameters), the  $T_B$  values at 6 GHz were warmed by up to 55 K. At 18 and 23.8 GHz the larger-sized Joss particles initiate liquid scattering more so than the smaller-sized MP size distribution, resulting in a small  $T_B$  cooling. From 10.69 GHz to 36.5 GHz, a transition from mostly absorptive (characterized by warmer  $T_B$  values) to mostly scattering (characterized by cooler  $T_B$  values) occurs. At stage C (the early cumulus profile), a change from having the coolest  $T_B$  at 10.69 GHz for all parameterizations and pixels (because there is little absorptive warming) to having the warmest  $T_B$  values at 36.5 GHz (because there is little scattering) occurs. Above 36.5 GHz changes in the raindrop size distribution initiated no differences in the  $T_B$  values with respect to the five-phase model due to the strong scattering signatures of storm-top ice at these higher frequencies. Adding liquid water to the snow and graupel hydrometeors caused absorptive warming at the low and middle frequencies.

From 89 GHz to 220 GHz the scattering signature is stronger than the absorptive warming signature. The comparison showed that the cooling signature due to ice scattering at higher frequencies was increased with larger ice concentrations. The ice concentration rose when additional ice was allocated to the ice–air–water ratio. Above 220 GHz the  $T_B$  variability among all six parameterizations and four stages was reduced. The compression was caused by an increasing sensitivity to hydrometeor size as wavelength decreased. This increasing sensitivity caused an increased opacity at the higher frequencies.

Finally, a comparison of the calculated  $T_B$  values with available observed  $T_B$  values from the CAMEX-3 experiment showed reasonable agreement for most stages and parameterizations. Exceptions occurred for the doubled ice-ratio parameterization and the two-phase parameterization. These two parameterizations consistently yielded  $T_B$  values outside the range of the observed minima and maxima, indicating that they are less physically realistic than the others. Another interesting feature is that the 220 and 340 GHz  $T_B$  calculations are well within the minima and maxima of the observations, thus providing an argument for increasing the diversity and complexity of frozen hydrometeors in models of convective cloud profiles. (The parameterizations used herein do not provide enough diversity at these frequencies.) Finally, there are a few stages/parameterizations/frequencies whose calculations do not fall within the observed minima and maxima. These few inconsistent cases could mean that the clouds were inadequately categorized into cumulus, evolving, mature, and/or dissipating stages or that the parameterizations are not modeling the true cloud microphysics for all cases. A detailed coincident set of  $T_B$  observations and *in situ* PSD measurements might be used to further refine cloud microphysical parameterizations.

# Direct estimation of sea state impacts on radar altimeter sea level measurements

D. Vandemark

NASA/Goddard Space Flight Center, Wallops Island, Virginia, USA

N. Tran<sup>1</sup> and B. D. Beckley

Raytheon/ITSS, Greenbelt, Maryland, USA

B. Chapron

IFREMER/Centre de Brest, Plouzané, France

P. Gaspar

Collecte Localisation Satellites, Ramonville, France

Received 1 July 2002; accepted 9 September 2002; published 17 December 2002.

[1] A new sea state bias modeling approach is presented that makes use of altimeter-derived marine geoid estimates. This method contrasts with previous models that require differencing between repeat altimeter passes for SSB isolation, along with complex bivariate inversion, to derive a relation between wind speed, wave height and SSB. Here one directly bin-averages sea height residuals over the wind and wave correlatives. Comparison with the most current nonparametric repeat-pass model shows close agreement and provides a first validation of this simpler and more direct technique. Success is attributed mainly to extensive space and time averaging. Ease in implementation and benefits in working with absolute levels provide much appeal. Further advantages and potential limitations, centered on the need to effectively randomize large sea level anomaly components to expose the bias, are also discussed. **INDEX TERMS:** 1640 Global Change: Remote sensing; 4275 Oceanography: General: Remote sensing and electromagnetic processes (0689); 4504 Oceanography: Physical: Air/sea interactions (0312); 6959 Radio Science: Radio oceanography; 4215 Oceanography: General: Climate and interannual variability (3309). **Citation:** Vandemark, D., N. Tran, B. D. Beckley, B. Chapron, and P. Gaspar, Direct estimation of sea state impacts on radar altimeter sea level measurements, *Geophys. Res. Lett.*, 29(24), 2148, doi:10.1029/2002GL015776, 2002.

## 1. Introduction

[2] The SSB in a satellite altimeter's range measurement results in a sea level estimate that falls below the true mean. Modeled SSB correction uncertainty is thought to be 1.5–2 cm on average and can exceed 5 cm in high seas [Chelton *et al.*, 2001].

[3] A location's sea surface height (SSH) measurement, uncorrected for SSB, contains the geoid signal ( $h_g$ ), the ocean dynamic topography ( $\eta$ ), the SSB, and other measurement and correction factors ( $w$ ):

$$SSH = h_g + \eta + SSB + w. \quad (1)$$

SSB modeling normally begins by eliminating the dominant marine geoid signal from equation (1) by differencing precise repeat measurements either along collinear tracks

[Chelton, 1994] or at orbit crossover points [Gaspar *et al.*, 1994]. Repeating altimeter measurements typically occur within 3–17 days, thus longer-term variance in the large  $\eta$  term is also removed. Using the two additional radar altimeter products, radar cross section-derived wind speed ( $U$ ) and significant wave height (SWH), SSB estimation relates time-dependent range differences to corresponding wave height and wind speed differences.

[4] While relatively successful, the development of empirical SSB models based on repeat-pass differences presents several limitations [Gaspar *et al.*, 2002]. Key among these is the need to develop a nonparametric model function to resolve nonlinearities obscured within standard regression techniques operating on differenced data. In addition, residual error analysis can only be performed in the space of the differenced variables. Further, large amounts of data and complex, numerically-optimized inversions are also required to properly develop such a model.

[5] Another approach is to solve for SSB directly by imposing a constant *a priori* mean sea level at each altimeter observation location thus eliminating the geoid. While substantial errors residing within equation (1) discouraged this approach in the past, the TOPEX/Poseidon mission has now provided ten years of precise measurements along the same 254 ground tracks across the global ocean. This paper provides a preliminary demonstration of this approach using TOPEX data.

## 2. Methods

[6] Following equation (1), a long-term average for the sea surface at any referenced location  $k$  on an altimeter's ground track can be written as:

$$MSS_k = (h_g + \langle \eta \rangle + \langle SSB - SSB_m \rangle + \langle w \rangle)_k \quad (2)$$

where  $\langle \rangle$  denotes the expectation computed over a given time period.  $SSB_m$  are the model-derived sea state range corrections employed in this surface determination, and  $w$  comprises all other error components (e.g. in sensor range corrections, interpolation errors, orbit, tides, atmospheric terms, etc. . .) built into the mean sea surface  $MSS_k$  estimate. Equation (2) assumes independence between source terms.

[7] An individual height residual,  $\Delta h_k = SSH_k - MSS_k$ , used in SSB estimation is thus:

$$\Delta h_k = (SSB + (\eta - \langle \eta \rangle) - \epsilon_{SSB} + (w - \langle w \rangle))_k \quad (3)$$

where  $\epsilon_{SSB} = \langle SSB - SSB_m \rangle$  at any  $k$  defines the time-independent SSB modeling error within  $MSS_k$ . Note that the many realizations forming every  $MSS_k$  and  $\epsilon_{SSB}$  differ from the arbitrary sample denoted in equation (3). Next, let dynamic sea level variability ( $\eta - \langle \eta \rangle$ ) be joined with ( $w - \langle w \rangle$ ) to form a noise term  $\epsilon$ . By design, the geoid term cancels out to give:

$$\Delta h_k = (SSB + \epsilon_{SSB} + \epsilon)_k \quad (4)$$

Error terms on the right side of the equation depend upon the quality of the estimates used to build  $MSS_k$  including, to some extent, the accuracy of the SSB model(s) used.

[8] An empirical bivariate SSB model is readily built by defining  $MSS_k$  globally and then computing the mean height bias at discrete bins across the  $(U, SWH)$  domain. Each bin holds the average over height residuals for all locations  $(k, ij)$ , meeting the condition that altimeter-derived wind and wave height estimates fall within a  $(U_i, SWH_j)$  bin having width  $(\Delta U, \Delta SWH)$ , given as:

$$SSB(U_i, SWH_j) = \langle (SSH_{ij} - MSS)_k \rangle \quad (5)$$

The  $\epsilon$  terms are dropped in equation (5) under a tentative assumption of weak dependency on sea state effects and assumed convergence of  $\eta$  and  $w$  terms towards zero mean values under long-term global averaging.

[9] Implementing this formula using TOPEX NASA altimeter (TOPEX hereafter) data is straightforward. The sea surface height residuals used are interpolated, georeferenced values computed along the TOPEX track using an established mean sea surface [Wang, 2001]. This surface merges multiple years and several satellite mission data sets (TOPEX, ERS, and Geosat) along the mean tracks of TOPEX [Koblinsky et al., 1998], spanning a time period from 1986 to 1999. The large time period and number of repeat measurements lead to precise geoid determinations along the TOPEX track. This provides not only a reference mean sea level for oceanic studies, but also a low noise  $MSS$  along the altimeter's ground track that was not available in past SSB investigations.

[10] Prior to computing  $\Delta h_k$ , TOPEX measurements are corrected for all geophysical and instrumental effects and the original SSB (version 2.0 algorithm [Gaspar et al., 1994]) is removed from each height estimate. These estimates are given at 1-s along-track intervals ( $\sim$ every 6 km) and interpolated to fixed georeferenced track locations. All Poseidon-1 altimeter and any erroneous (using conventional data quality flagging) TOPEX estimates are eliminated. Pairing of the NASA/GSFC Altimeter Pathfinder dataset with both TOPEX radar cross section  $\sigma_0$  and  $SWH$  data is accomplished using the same georeferencing interpolation. The 10-m wind speed is calculated from  $\sigma_0$  using the modified Chelton and Wentz algorithm [Witter and Chelton, 1991]. One 10-day TOPEX cycle of pathfinder data prepared in this manner provides 350,000–400,000 samples. For direct comparison to the most current SSB model [Gaspar

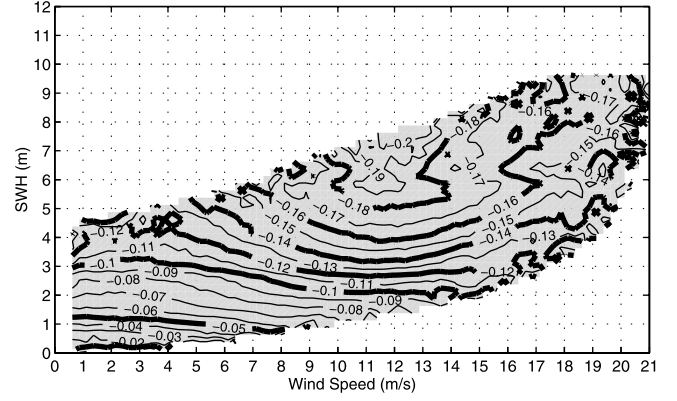


**Figure 1.** Isolines for the global TOPEX SSB estimate (in meters) obtained from bin-averaging into boxes of width (0.25 m/s, 0.25 m) over the  $(U, SWH)$  domain.

et al., 2002] (NP02 hereafter), cycles 21–131, April 1993–April 1996, are examined. The number of samples used in this 3-year average exceeds forty million. For demonstrations here, data are not spatially subsampled to insure independence. Data set size would contract by a factor of 7–10 with such sampling. By comparison, the NP02 cross-over set contains 633,000 points for the same period.

#### 4. Conclusion

[18] This is the first reported direct (non-differenced) realization of on-orbit altimeter SSB impacts. The technique relies upon averaging over a numerous realizations to isolate the small SSB signature. Results from a 3-year global average mirror that obtained using satellite crossover differences and subsequent nonparametric model inversion. It is also shown that an accurate SSB estimate can be obtained over most of the altimeter-derived  $(U, SWH)$  domain with as little as 100 days of data, a substantial improvement. Direct intercomparison corroborates two separate empirical TOPEX SSB derivations, but observed mm-level offsets and estimate differences for infrequently observed locations in the  $(U, SWH)$  domain highlight the need for future refinement.

[19] There is no question that this direct method is simpler to implement from numerous perspectives, foremost the avoidance of complex and numerically-intensive non-parametric inversion. Moreover, one is now working directly with the height residual and its correlatives, rather than time-dependent differences in all terms. These points, among others, suggest the benefit that direct assessment may have in speeding studies to evaluate the relative importance of additional characteristics of sea state beyond altimeter-derived  $(U, SWH)$ . For instance, direct regression of TOPEX height residuals against global model-derived long wave products, unobtainable using the altimeter, are in progress and may identify remaining SSH variance. Further, the sparse time-sampling approach of Figure 2a can also be applied spatially, where basin-scale evaluation of the sea state impacts now becomes more tractable. It is also likely that this SSB methodology is applicable to altimeters aboard ERS, Envisat, or Geosat Follow-On platforms with use of an appropriate mean surface reference.



# Ocean-color optical property data derived from the Japanese Ocean Color and Temperature Scanner and the French Polarization and Directionality of the Earth's Reflectances: a comparison study

Menghua Wang, Alice Isaacman, Bryan A. Franz, and Charles R. McClain

We describe our efforts to study and compare the ocean-color data derived from the Japanese Ocean Color and Temperature Scanner (OCTS) and the French Polarization and Directionality of the Earth's Reflectances (POLDER). OCTS and POLDER were both on board Japan's Sun-synchronous Advanced Earth Observing Satellite from August 1996 to June 1997, collecting approximately 10 months of global ocean-color data. This operation provided a unique opportunity for the development of methods and strategies for the merging of ocean-color data from multiple ocean-color sensors. We describe our approach to the development of consistent data-processing algorithms for both OCTS and POLDER and the use of a common *in situ* data set to calibrate vicariously the two sensors. Therefore the OCTS- and POLDER-measured radiances are bridged effectively through common *in situ* measurements. With this approach to the processing of data from two different sensors, the only differences in the derived products from OCTS and POLDER are the differences that are inherited from the instrument characteristics. Results show that there are no obvious bias differences between the OCTS- and POLDER-derived ocean-color products, whereas the differences due to noise, which stem from variations in sensor characteristics, are difficult to correct at the pixel level. The ocean-color data from OCTS and POLDER therefore can be compared and merged in the sense that there is no significant bias between two.

© 2002 Optical Society of America

OCIS codes: 010.0010, 280.0280, 010.4450.

## 1. Introduction

The Japanese Ocean Color and Temperature Scanner (OCTS)<sup>1</sup> and French Polarization and Directionality of the Earth's Reflectances (POLDER)<sup>2</sup> were both flown on the Japanese Sun-synchronous Advanced Earth Observing Satellite (ADEOS) from August 1996 to June 1997, collecting about 10 months of global ocean color data. ADEOS was on a polar orbit at an altitude of 800 km with local crossing time

(descending node) at around 10:40 am. This was the first time in history that two ocean-color sensors were on board the same platform and viewed the global ocean with the same temporal and similar global spatial coverages. Therefore the operation provides an ideal case for studying and comparing ocean-color data that is derived from two different sensors, hence allowing the development of a strategy for a ocean-color data merger from multiple ocean-color sensors. The primary goal of the National Aeronautics and Space Administration Sensor Intercomparison and Merger for Biological and Interdisciplinary Oceanic Studies (SIMBIOS) project is to develop methods for the meaningful comparison and merging of data products from multiple ocean-color missions.<sup>3</sup> In a recent study, Wang and Franz<sup>4</sup> show that, using a vicarious intercalibration approach between the modular optoelectronic scanner (MOS)<sup>5</sup> and the Sea-viewing Wide Field-of-View Sensor (SeaWiFS)<sup>6,7</sup> (SeaWiFS ocean color data were used as "truth"), one can meaningfully compare the ocean optical property data derived from two sensors. The bias differences

---

M. Wang (wang@simbios.gsfc.nasa.gov), A. Isaacman, B. A. Franz, and C. R. McClain are with the National Aeronautics and Space Administration Goddard Space Flight Center, Greenbelt, Maryland 20771. M. Wang is also with the University of Maryland—Baltimore County, Baltimore, Maryland 21210. A. Isaacman and B. A. Franz are also with the Science Applications International Corporation General Sciences Corporation, Beltsville, Maryland 20705.

Received 7 March 2001; revised manuscript received 19 September 2001.

0003-6935/02/060974-17\$15.00/0

© 2002 Optical Society of America

are reduced significantly between the two products. In the Wang-Franz study,<sup>4</sup> measurements from the two sensors had a temporal difference of about 90 min. In this paper, we compare the ocean-color data derived from OCTS and POLDER measurements using consistent data-processing algorithms for both sensors and vicarious calibrations based on a common *in situ* data set from the Marine Optical Bouy (MOBY)<sup>8</sup> in the waters off Hawaii. Therefore differences in the derived ocean-color products from OCTS and POLDER are associated primarily with differences in instrument characteristics. We first give a brief overview of the sensor characteristics of the OCTS and the POLDER and their differences. Detailed algorithm descriptions for processing OCTS and POLDER data are then presented. Next we outline the vicarious calibration scheme in which the OCTS- and POLDER-measured radiances are calibrated with a common *in situ* MOBY data set. Finally, we provide results that compare OCTS and POLDER ocean-color data with global *in situ* measurements and compare a series of OCTS measurements with those of POLDER over the Sargasso Sea and the Bermuda area.

## 6. Conclusion

We describe a procedure to calibrate vicariously OCTS and POLDER Level-1B data using the MOBY *in situ* measurements. This procedure effectively bridges the OCTS and POLDER Level-1B data through the use of a common set of MOBY *in situ* measurements. The vicarious calibration assumes the band 865-nm gain coefficients are not changed, while the visible bands are adjusted such that the derived normalized water-leaving radiances are forced to be equivalent to the MOBY *in situ* measurements. Using the derived gain coefficients, we can use a consistent atmospheric-correction algorithm to process OCTS and POLDER data from Level-1B to Level-2 products. Therefore the differences in the OCTS and POLDER-derived ocean-color products are mainly from the differences of the sensor characteristics, i.e., with this approach, the retrieved products would be identical if the two sensors were identical.

We demonstrate the efficacy of vicariously recalibrating OCTS and POLDER with a common *in situ* data set and using a consistent atmospheric-correction algorithm for data processing. Both the OCTS- and POLDER-derived normalized water-leaving radiances compare reasonably well with independent *in situ* data. Over the Sargasso Sea and the Bermuda area, the ocean-color products derived from OCTS have a good agreement with data from POLDER measurements. It is particularly important that there are no obvious bias differences be-

tween the OCTS- and POLDER-derived ocean-color data, i.e., the overall ratio values between the OCTS- and POLDER-derived normalized water-leaving radiances at 443, 490, and 565 nm are 1.0004, 1.0103, and 0.9840, while the ratio value in the derived chlorophyll-a concentration is 0.9907. However, the noise differences, which are usually inherited from sensor characteristics, are difficult to remove at the pixel level. These noise differences possibly can be reduced with data-averaging schemes (e.g., averaging Level-2 data to Level-3 products). To resolve the noise problem, however, one will generally need improved instruments, e.g., high sensor signal-to-noise performance, good sensor linearity response, and high radiometric stability. It is found that the POLDER-derived  $[L_w(\lambda)]_N$  are usually more noisy than those of OCTS, in particular, for the 443-nm band products. This most likely results from the POLDER sensor nonlinearity response problem.<sup>37</sup> On the other hand, effects of the subpixel cloud contamination around cloud edge lead to high sparkling values in the POLDER-retrieved ocean color products.

The OCTS and POLDER data-processing procedures and algorithms are scheduled to be implemented in MSL12 within the SeaDAS software,<sup>12</sup> which is freely available. Therefore interested scientists can process OCTS and POLDER data with the widely distributed SeaDAS software package.

The OCTS and POLDER Level-1B data were provided by National Space Development Agency of Japan and Centre National d'Etudes Spatiales of France. We thank J.-M. Nicolas for his assistance with the POLDER Level-1B data, D. Clark and his research group for providing the MOBY data, J. O'Reilly and S. Maritorena for the modified OC2 algorithm, F. Patt for help in OCTS navigation analyses, S. Bailey and J. Werdell for help for the SeaBASS *in situ* data analyses, and two anonymous reviewers for their helpful comments. This research was supported by funding provided by National Aeronautics and Space Administration under the Sensor Intercomparison and Merger for Biological and Interdisciplinary Oceanic Studies (SIMBIOS) project and partly from NASA SIMBIOS grant NAS5-00203.

# Irregular Snow Crystals: Structural Features as Revealed by Low Temperature Scanning Electron Microscopy

WILLIAM P. WERGIN, ALBERT RANGO,\* JAMES FOSTER,† ERIC F. ERBE, CHRISTOPHER POOLEY‡

Soybean Genomics and Improvement Laboratory, Agricultural Research Service (ARS), U.S. Department of Agriculture (USDA), Beltsville, Maryland; \*Jornada Experimental Range, ARS, USDA, New Mexico State University, Las Cruces, New Mexico; †Laboratory for Hydrological Sciences, NASA Goddard Space Flight Center, Greenbelt; Maryland and ‡Hydrology and Remote Sensing Laboratory, ARS, USDA, Beltsville, Maryland, USA

**Summary:** For nearly 50 years, investigators using light microscopy have vaguely alluded to a unique type of snow crystal that has become known as an irregular snow crystal. However, the limited resolution and depth-of-field of the light microscope has prevented investigators from characterizing these crystals. In this study, a field-emission scanning electron microscope, equipped with a cold stage, was used to document the structural features, physical associations, and atmospheric metamorphosis of irregular snow crystals. The crystals appear as irregular hexagons, measuring 60 to 90 nm across, when viewed from the *a*-axis. Their length (*c*-axis) rarely exceeds the diameter. The irregular crystals are occasionally found as secondary particles on other larger forms of snow crystals; however, they most frequently occur in aggregates consisting of more than 100 irregular crystals. In the aggregates, the irregular crystals have their axes oriented parallel to one another and, collectively, tend to form columnar structures. Occasionally, these columnar structures exhibit rounded faces along one side, suggesting atmospheric metamorphoses during formation and descent. In extreme cases of metamorphoses, the aggregates would be difficult to distinguish from graupel. Frost, consisting of irregular crystals, has also been encountered, suggesting that atmospheric conditions that favor their growth can also occur terrestrially.

**Key words:** field-emission scanning electron microscopy, low-temperature scanning electron microscopy, snow crystals, irregular crystals, snowflakes, rime, graupel

**PACS:** 61.16 Bg, 61.66.-f, 81.10.Aj, 92.40.Rm

---

Address for reprints:

William P. Wergin  
Soybean Genomics and Improvement Laboratory  
Agricultural Research Service  
U.S. Department of Agriculture  
Beltsville, MD 20705, USA

## Introduction

Snow crystals have been studied with the light microscope for more than 100 years. However, because of their small size, delicate structure, and topography, this instrument has failed to elucidate many of the structural details of the crystals. In addition, snow is difficult to transport, store, image, and photograph without subjecting samples to structural changes resulting from sublimation, melting or recrystallization. Examination of snow crystals with a scanning electron microscope (SEM) would solve problems associated with resolution, topography, and their delicate nature. However, for obvious reasons, frozen samples cannot be imaged at ambient temperatures in a conventional SEM.

In 1970, Echlin *et al.* (1970) solved this problem for biologists by describing a cold stage that could be interfaced with an SEM and operated at temperatures below  $-130^{\circ}\text{C}$ . At these temperatures, the vapor pressure of water is not significant and sublimation does not occur at a detectable rate. Furthermore, recrystallization of pure water-ice does not occur (Beckett and Read 1986) and frozen, fully hydrated samples remain stable for several hours while being observed (Wergin and Erbe 1991).

Recently, this procedure, which has become known as low-temperature (LT) SEM, was used to compare frozen, fully hydrated, fractured membranes of yeast in the SEM with the platinum/carbon (Pt/C) replicas of the identical cells in the transmission electron microscope (TEM) (Wergin and Erbe 1990). Results indicated that macromolecular particles, as small as 10 nm in diameter, retained their structure, were stable, and could be imaged and photographed with LTSEM. The images, which were obtained in the LTSEM, were comparable with those of the same cells in the Pt/C replicas, which were photographed in a TEM. Encouraged by these results, identical snow crystals were imaged and photographed with a light microscope, imaged and photographed in the

---

Contribution of the Agricultural Research Service, U.S. Department of Agriculture; Not subject to copyright.

LTSEM, and then rephotographed with a light microscope. The results further demonstrated that observation in the LTSEM did not alter the structure of the snow crystals (Wergin *et al.* 1998). In addition, techniques were developed to collect, ship, and store fresh and metamorphosed snow crystals for subsequent imaging with an LTSEM. These techniques have been successfully used to record detailed images of thousands of snow crystals that were collected from numerous states including Alaska, Colorado, Montana, Utah, Wyoming, Wisconsin, Maryland, and West Virginia. In previous studies, we have described the detailed structure of snow and ice grains including columns, needles, plates, stellar dendrites, depth hoar, and glacial ice that were collected from several states (Rango *et al.* 1996a, b, 2000; Wergin and Erbe 1994a, b; Wergin *et al.* 1995, 1996a, b, 1998, 1999). The current study uses LTSEM to illustrate the features and distinctive characteristics of the elusive group of crystals recognized by The International Commission on Snow and Ice (Colbeck *et al.* 1990) and simply referred to as "irregular crystals."

## Materials and Methods

### Collection Procedure

Data illustrated in this study resulted from six different snow collections during 1993–1999 from sites near the following locations: Beltsville, Maryland; Bearden Mt., West Virginia and Greenwood, Wisconsin. The samples, which were obtained when the air temperatures ranged from  $-5^{\circ}\text{C}$  to  $0^{\circ}\text{C}$ , consisted of freshly fallen snowflakes. To collect samples, a thin layer of liquid Tissue-Tek, a commonly used cryoadhesive for biological samples, was spread on a flat copper plate ( $15 \times 27$  mm). The Tissue-Tek and the plates were precooled to ambient outdoor temperatures (below freezing) before use. Newly fallen snowflakes were either permitted to settle on the surface of the Tissue-Tek or were lightly dislodged from the snow surface and allowed to fall onto the surface of the cryoadhesive. Next, the plate was either rapidly plunged into a Styrofoam vessel containing liquid nitrogen ( $\text{LN}_2$ ) or placed on a brass block that had been precooled with  $\text{LN}_2$  to  $-196^{\circ}\text{C}$ . This process, which solidified the Tissue-Tek, resulted in firmly attaching the snow crystals to the plate. The frozen plates were inserted diagonally into prefabricated 20 cm segments of square, brass channel tubing, containing an end cap, and lowered into dry shipping dewars that had been previously cooled with  $\text{LN}_2$ . The dewars containing the samples were conveyed from the collection sites and then either transported by van (from West Virginia) or shipped by air (Wisconsin) to the laboratory in Beltsville, Maryland. Upon reaching the laboratory, the samples were transferred under  $\text{LN}_2$  to a  $\text{LN}_2$  storage dewar where they remained at  $-196^{\circ}\text{C}$  for as long as 9 months before being further prepared for observation with LTSEM.

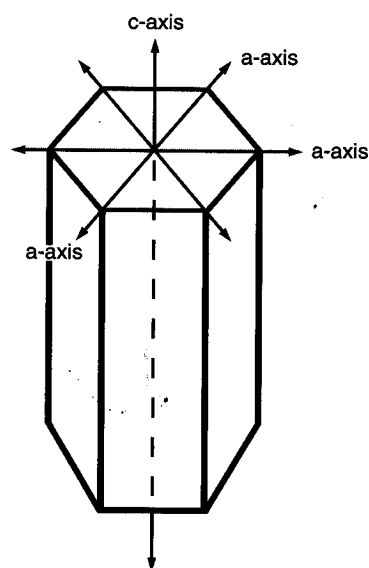


FIG. 1 Diagram illustrating the crystallographic axes of snow crystal growth. Environmental conditions that favor growth along the a-axes result in flat hexagonal plates and stellar dendrites, whereas conditions that favor c-axis growth produce elongated columns and needles. Neither type of growth predominates in the formation of irregular crystals.

## Conclusion

This study uses LTSEM to characterize small discrete crystals believed to correspond to the irregular crystals that previous investigators have attempted to describe with the light microscope. These crystals, which appear as irregular hexagons when viewed along their a-axes, generally measure 60 to 90  $\mu\text{m}$  across. Their lengths (c-axis) rarely exceed their diameters. Although the irregular crystals are occasionally found as individual, secondary particles on other larger forms of snow crystals, such as plates and dendrites, they are most frequently encountered in aggregates consisting of more than 100 crystals that tend to form a column. The aggregates are often associated with needles, suggesting that the atmospheric conditions that favor needle growth may be close to those that favor growth of irregular crystals. Furthermore, examples believed to represent atmospheric metamorphoses of irregular crystals are commonly encountered. Metamorphosis can result in aggregates that consist of partially sublimated crystals and droplets that collectively would be difficult to distinguish from graupel when using a light microscope.

## Low Temperature Scanning Electron Microscopy of Irregular Snow Crystals

William P. Wergin,\* Albert Rango,\*\* James Foster,\*\*\* Eric F. Erbe,\* and Christopher Pooley\*\*\*\*

\*Soybean Genomics and Improvement Laboratory, Agricultural Research Service (ARS), U.S. Department of Agriculture (USDA), Beltsville, MD 20705 USA

\*\*Jornada Experimental Range, ARS, USDA, New Mexico State University, 401 E. College Ave., Las Cruces, NM 88003 USA

\*\*\*Laboratory for Hydrological Sciences, NASA Goddard Space Flight Center, Greenbelt, MD 20771 USA

\*\*\*\*Hydrology and Remote Sensing Laboratory and Soybean Genetics and Improvement Laboratory, ARS, USDA, Beltsville, MD 20705 USA

Snow crystals occur in eight basic types: columns, needles, plates, dendrites, irregular crystals, graupel, hail and ice pellets.[1] Most of these types have been described and photographed.[2] However, our understanding of the "irregular crystals" remains vague because the limited resolution and depth-of-field associated with the light microscope have prevented investigators from fully characterizing and clearly illustrating the features of these crystals. Our study used a field-emission scanning electron microscope (FESEM), equipped with a cold stage, to document the structural features, physical associations and atmospheric metamorphosis of irregular snow crystals.

Snow samples, consisting of freshly fallen snowflakes, were collected from six different locations where air temperatures ranged from  $-5^{\circ}\text{C}$  to  $0^{\circ}\text{C}$ . The collection procedure consisted of spreading a cryo-adhesive on a pre-cooled flat copper plate and allowing newly fallen snowflakes to settle on the surface. Next, the plate was rapidly frozen in  $\text{LN}_2$ . The frozen plates were placed in a dry shipping dewar and conveyed to the laboratory where they were coated for observation in a Hitachi S-4100 FESEM equipped with an Oxford CT 1500 HF Cryotrans system as previously describe.[3]

Crystals, believed to correspond to irregular crystals, appeared as short, irregular hexagons, measuring 60 to 90  $\mu\text{m}$  across, when viewed from the a-axis (Fig. 1). Their length (c-axis) rarely exceeded the diameter. The irregular crystals were occasionally found as secondary particles on other larger forms of snow crystals (Fig. 2). However, they most frequently occurred as aggregates consisting of more than 100 irregular crystals (Fig. 3). In the aggregates, the irregular crystals had their c-axes oriented parallel to one another and collectively, tended to form columnar structures. Occasionally the aggregates exhibited rounded facets along one side, suggesting atmospheric metamorphoses and unidirectional fall. In extreme cases of metamorphoses, the aggregates would be difficult to distinguish from graupel. Frost, consisting of irregular crystals, was also encountered, suggesting that atmospheric conditions that favor this form of growth also occur terrestrially (Fig. 4).

Results obtained with low temperature FESEM suggested that crystals, which were previously designated as "irregular crystals", have distinctive features that can be used to characterize and distinguish them from other types of snow crystals.

[1] S. Colbeck et al., *The International Classification for Seasonal Snow on the Ground*, Univ. of Colorado, Boulder, 1990.

[2] U. Nakaya. *Snow Crystals: Natural and Artificial*, Harvard Univ. Press, Cambridge, MA, 1954.

[3] W.P. Wergin et al., *Scanning*. 17 (1995) 41.



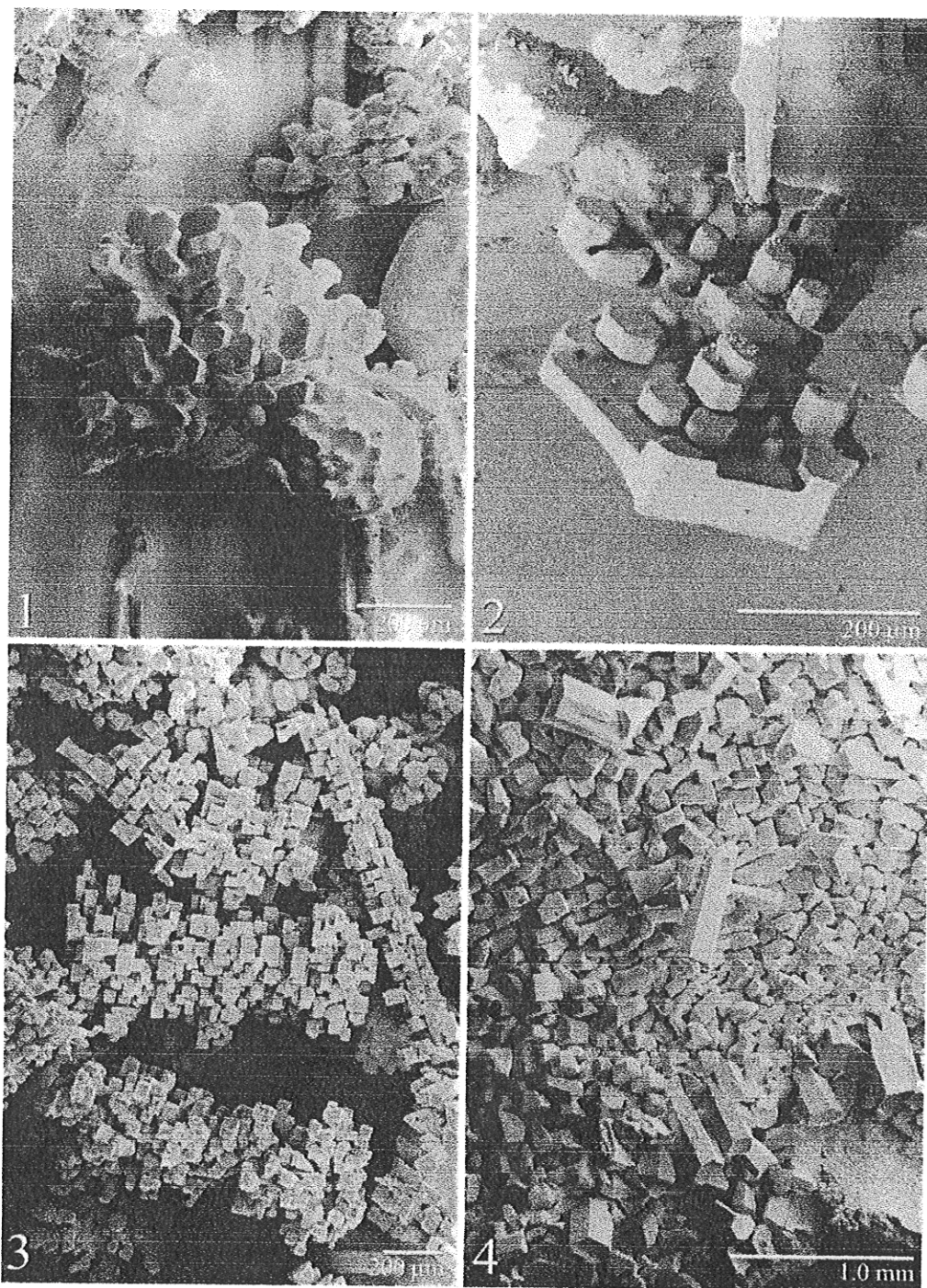


**Figure 1.** A-axis view of irregular crystals, which appear as asymmetric hexagons.  
**Figure 2.** Irregular crystals, which occur as secondary particles on the surface of a dendritic arm.  
**Figure 3.** Several "snowflakes", each consisting of aggregates of numerous irregular crystals.  
**Figure 4.** Irregular crystals that had formed on the surface of a leaf.

# Validation of Sea Ice Motion from QuikSCAT with those from SSM/I and Buoy

Yunhe Zhao, Antony K. Liu, and David G. Long, *Senior Member, IEEE*

**Abstract**—Arctic sea ice motion for the period from October 1999 to March 2000 derived from QuikSCAT and special sensor microwave/imager (SSM/I) data using the wavelet analysis method agrees well with ocean buoy observations. Results from QuikSCAT and SSM/I are compatible when compared with buoy observations and complement each other. Sea ice drift merged from daily results from QuikSCAT, SSM/I, and buoy data gives more complete coverage of sea ice motion. Based on observations of six months of sea ice motion maps, the sea ice motion maps in the Arctic derived from QuikSCAT data appear to have smoother (less noisy) patterns than those from NSCAT, especially in boundary areas, possibly due to constant radar scanning incidence angle. For late summer, QuikSCAT data can provide good sea ice motion information in the Arctic as early as the beginning of September. For early summer, QuikSCAT can provide at least partial sea ice motion information until mid-June. In the Antarctic, a case study shows that sea ice motion derived from QuikSCAT data is consistent with pressure field contours.

**Index Terms**—QuikSCAT, sea ice motion, special sensor microwave/imager (SSM/I), wavelet transform.

## I. INTRODUCTION

QUICKSCAT, a “quick recovery” mission to fill the gap created by the loss of data from the NASA Scatterometer (NSCAT), when the ADEOS-1 satellite lost power in June 1997, was launched on June 19, 1999. QuikSCAT is an active sensor, and the sensor footprint is an ellipse  $25 \text{ km} \times 37 \text{ km}$ . In both the Arctic and the Antarctic regions, repeated footprints of the satellite make it possible to construct QuikSCAT images with a 12.5 km grid and finer resolution (e.g., see [1]). In this paper, the daily (estimated over a four-day sliding window for the Arctic and over a one-day sliding window for the Antarctic) sea ice motion derived from QuikSCAT using an ice-tracking algorithm based on wavelet transform is demonstrated, and the applications of the daily sea ice motion are indicated. The uncertainty of QuikSCAT-derived sea ice motion is determined from validation with those from *in situ* buoy data and Defense Meteorological Satellite Program (DMSP) special sensor microwave/imager (SSM/I) observations during the same period of time. The instrument differences between QuikSCAT and NSCAT lead to significantly different spatial and temporal sampling characteristics, and it is for this reason that QuikSCAT ice motion validation is required. NSCAT is a fan-beam scatterometer with fixed azimuth but variable incidence, while QuikSCAT has fixed incidence and variable azimuth.

Satellite observations provide more complete and routine coverage of polar region than observations from any other means, and they have been used by several authors in deriving polar sea ice drift (e.g., see [2] and references cited there). The efficiency and utility of wavelet transform in analyzing

nonlinear dynamical ocean systems has also been documented in several papers ([2] and references cited there). In Section II, wavelet analysis for ice feature tracking and sea ice motion from QuikSCAT and SSM/I data are presented. Wavelet analysis results from QuikSCAT and SSM/I are compared with the ice motion derived from buoys for validation in Section III. Section IV deals with the potential application of QuikSCAT data in summer ice tracking. Section V is devoted to a sea-ice-tracking case study for the Antarctic using QuikSCAT data. The results and applications of satellite-derived sea ice motion are discussed and summarized with previous NSCAT and SSM/I data in the final section.

## II. WAVELET ANALYSIS OF SATELLITE IMAGES

A sea-ice-tracking procedure based on wavelet transform of satellite data and its error analysis have appeared in [2]–[4]. The effect of wavelet transform is a bandpass filter with a threshold for feature detection. For the details of the procedure, we refer readers to [2]–[4]. In this study, the same procedure is applied to QuikSCAT and SSM/I data with a few modifications. For the Arctic, QuikSCAT images with 12.5 km pixel size are first constructed from QuikSCAT Level 2A data, and SSM/I images are obtained from SSM/I compact discs. QuikSCAT Sigma-0 data has an incidence angle either around  $54.24^\circ$  (*v*-polarization) or around  $46.44^\circ$  (*h*-polarization) within  $\pm 0.5^\circ$ . Only *v*-polarization Sigma-0 data with an incidence angle around  $54.24^\circ$  are used in the construction of QuikSCAT images because of its better coverage. Areas indicated by sea ice flags in QuikSCAT data as land, open ocean, or no-data areas are masked in the images. For the Antarctic case study, the QuikSCAT data are processed with a scatterometer image reconstruction (SIR) resolution enhancement algorithm to a pixel resolution of 4.45 km from QuikSCAT Level 1B data [1], and sea ice extent is determined using the method of [5]. The QuikSCAT design specifications for location accuracy requirements are 25 km (rms) absolute and 10 km (rms) relative. However, the actual performance is currently estimated to be better than 6 km (rms) absolute and less than 1 km (rms) relative with bias dominating the total error [6]. Thus, QuikSCAT has very high precision measurement locations, far exceeding its design specifications and enabling the application of resolution enhancement algorithms. For both cases, wavelet transform is then applied to the satellite image at various scales to separate various ice textures or features. In the Arctic, two tracking regions are considered: coast/bay for fast ice motion (with a two-day sliding window), and central Arctic for slow ice motion (with a four-day sliding window). Template matching is performed with the results from the wavelet transform of the images between day 1 and day 5 for the central Arctic and between day 2 and day 4 for the coast/bay.

In the Antarctic, template matching is performed with the results from the wavelet transform of the images between day 1 and day 2. For both cases, velocities are estimated by dividing the displacement over the time interval. Finally, the sea ice drift map can be merged by block average with outlier filtering. The outlier filtering after block average is performed as follows: at any location, the mean velocity of nine neighboring ice velocities is computed. If the angle between the mean ice velocity and the ice velocity at the location is bigger than a certain degree, then the ice velocity at the location is discarded.

Fig. 1(a) and (b) show sea ice drift maps of the Arctic Ocean for November 5, 1999, derived from SSM/I and QuikSCAT data, respectively, where thin white arrows indicate velocities derived from satellite data, while thick white arrows indicate velocities derived from buoy data. Two circulation patterns—one in the Beaufort Sea and the other across the Chukchi, Beaufort, and Laptev Seas—are clearly observed in the maps. The ice motion converges in an area between the Chukchi Sea and the Beaufort Sea. Notice that velocities derived from both QuikSCAT and SSM/I data agree well with those from buoy data. Wavelet transform scales used in deriving these images from QuikSCAT and SSM/I data are based on parameter study and testing and are 1.0, 2.42, and 2.828. The resultant ice velocities have been block averaged to a  $100 \text{ km} \times 100 \text{ km}$  grid with outlier filtering. The empty areas with no velocity in the map indicate the regions where the tracking procedure cannot be used, since no matching templates between the time periods can be determined. Clearly, the ice motion maps derived from QuikSCAT and SSM/I data for November 5, 1999 are complementary to each other. The regions without ice velocity data from QuikSCAT and SSM/I are generally not colocated, since the QuikSCAT and SSM/I data correspond to different physical features: surface roughness and brightness–temperature anomalies, respectively. For the period from October 1999 to March 2000, based on the observations of sea ice motion maps, the patterns of motion from QuikSCAT appear smoother than those from SSM/I.

## VI. DISCUSSION

To further examine satellite-data-derived sea ice motion, Table I summarizes some six-month comparison results of sea ice motion derived from SSM/I, NSCAT, and QuikSCAT with those derived from buoy data for different periods. For all comparison periods, the rms of the speed differences between buoy-derived ice velocities and satellite-derived ones are all under 3 cm/s, and the rms of the direction differences between them are around  $30^\circ$ . Moreover, all satellite-derived sea ice motion data sets are consistent and comparable.

It is clear that sea ice motion products derived from SSM/I, NSCAT, and QuikSCAT data have very good quantitative agreements with the ice motion products derived from buoy data. But, the sea ice motion products derived from NSCAT and QuikSCAT data are slightly more accurate than that derived from SSM/I data because both NSCAT and QuikSCAT are active sensors and do not suffer from cloud and atmospheric effects. Also, the results from NSCAT and QuikSCAT are very consistent. The rms of the direction difference between NSCAT-derived and buoy-derived ice drift for the period from October, 1996 to March, 1997 is slightly better than that

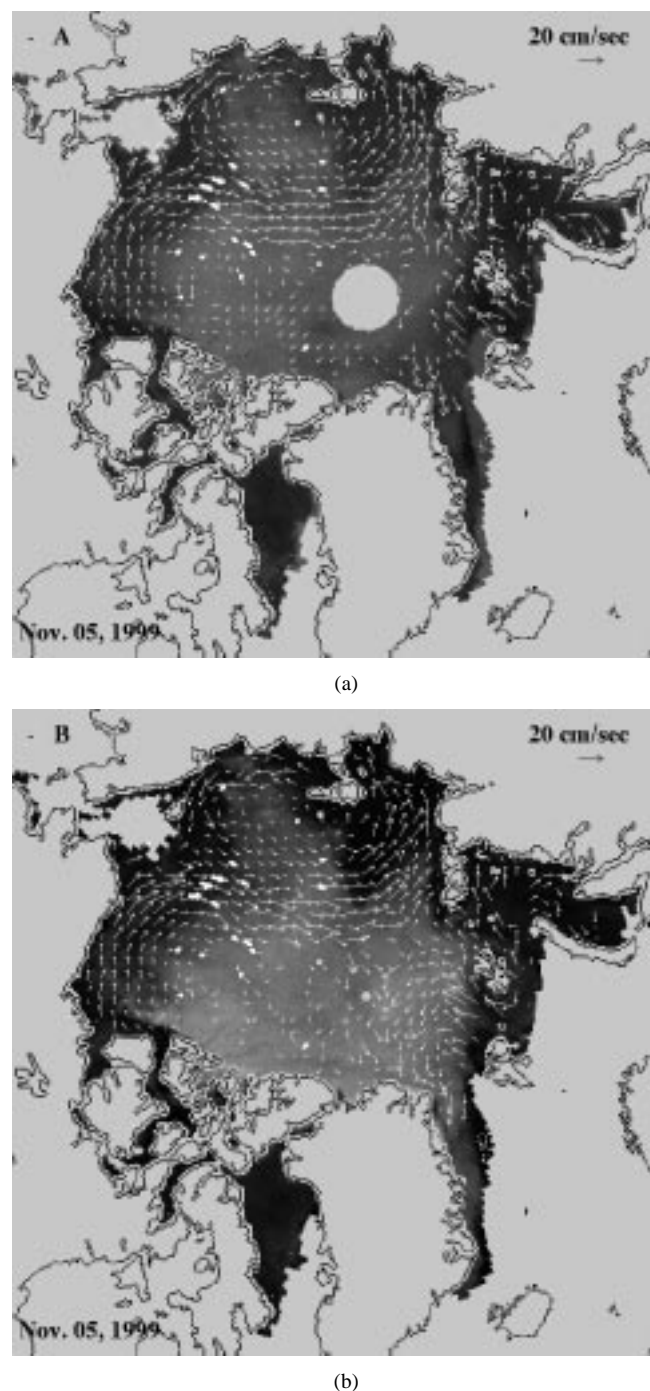


Fig. 1. Arctic sea ice drift maps of the Arctic basin in a grid of  $100 \times 100 \text{ km}$  derived from (a) SSM/I 85 GHz radiance data and (b) from QuikSCAT data on November 5, 1999. Thin white arrows indicate velocities derived from feature tracking using wavelet analysis, while thick white arrows indicate velocities from buoys.

between QuikSCAT-derived ice velocities and buoy-derived ones for the same winter period in 1999 and 2000. But keep in mind that the rms are for two different periods and that the ice motion in the central Arctic during winter 1999 has a very slow motion, and so the ice-tracking results are less accurate. In fact, based on the observations, the ice motion maps from QuikSCAT data appear to have smoother patterns than those from NSCAT, especially in boundary areas, e.g., in the Kara and Barents Seas where there is no buoy for comparison.